UNIVERSIDADE FEDERAL DE SANTA CATARINA
CENTRO TECNOLÓGICO
PROGRAMA DE PÓS-GRADUAÇÃO EM ENGENHARIA E CIÊNCIAS TÉRMICAS

Guilherme Grando Carqueja

Novel Conception of Compact Diffusion Bonded Heat Exchanger

Florianópolis
2021

Guilherme Grando Carqueja

Novel Conception of Compact Diffusion Bonded Heat Exchanger

Dissertação submetida ao Programa de Engenharia Mecânica da Universidade Federal de Santa Catarina para a obtenção do título de mestre em Engenharia e Ciências Térmicas.

Orientadora: Profa. Marcia Barbosa Henriques Mantelli, PhD.

Florianópolis
2021

Ficha de identificação da obra elaborada pelo autor,
através do Programa de Geração Automática da Biblioteca Universitária da UFSC.

Carqueja, Guilherme
Novel Conception of Compact Diffusion Bonded Heat Exchanger / Guilherme Carqueja ; orientadora, Marcia Barbosa Henriques Mantelli, 2021.
162 p.

Dissertação (mestrado) - Universidade Federal de Santa Catarina, Centro Tecnológico, Programa de Pós-Graduação em Engenharia Mecânica, Florianópolis, 2021.

Inclui referências.

1. Engenharia Mecânica. 2. Trocadores de Calor. 3. Convecção Forçada. 4. União por Difusão. 5. Correlação Convectiva. I. Barbosa Henriques Mantelli, Marcia. II. Universidade Federal de Santa Catarina. Programa de Pós Graduação em Engenharia Mecânica. III. Título.

Guilherme Grando Carqueja

Novel Conception of Compact Diffusion Bonded Heat Exchanger

O presente trabalho em nível de mestrado foi avaliado e aprovado por banca examinadora composta pelos seguintes membros:

Prof. Alexandre Kupka da Silva, PhD.
UFSC

Prof. Jose Alberto dos Reis Parise, PhD.
PUC-RJ

Certificamos que esta é a **versão original e final** do trabalho de conclusão que foi julgado adequado para obtenção do título de mestre em Engenharia e Ciências Térmicas.

Documento assinado digitalmente
Paulo de Tarso Rocha de Mendonca
Data: 09/10/2021 12:24:14-0300
CPF: 149.822.691-49
Verifique as assinaturas em https://v.ufsc.br

Coordenação do Programa de
Pós-Graduação

Documento assinado digitalmente
Marcia Barbosa Henriques Mantelli
Data: 09/10/2021 00:05:15-0300
CPF: 025.041.158-06
Verifique as assinaturas em https://v.ufsc.br

Profa. Marcia Barbosa Henriques Mantelli,
PhD.
Orientadora

Florianópolis, 2021

To my parents, who have always supported me.
To my grandparents.

ACKNOWLEDGEMENTS

Primarily, I would like to thank my parents for their amazing support. They have always made me a better human being and helped me achieve my goals. Sharing their values and knowledge with me is just part of everything they did to me. Throughout my entire life, I have been presented with many opportunities of experiencing amazing moments thanks to them.

I would also like to thank my grandparents Ury and Mercedes for taking care of me so many times during my childhood and teenage years. They have always been a huge part of my life and I feel honored to be their grandson. I must also include here the rest of my family, especially my aunts, for adopting me as a son more than a nephew.

At this point, it is only fair that I thank my girlfriend Fabiane for all the support and love. As time passes, it becomes increasingly clearer to me that living with her makes life more beautiful. In her, I find support, care, warmth, friendship and, most importantly, love. She played a very important role helping me get this work done and she deserves a great amount of credit for it.

I would also like to thank Professor Marcia Mantelli for guiding me through this masters program. Along the way, she always believed in me and gave me autonomy to conduct the activities as I thought to be the best way. I must also thank the entire team of Labtucal for the amazing support.

My good friends João V. Colin Batista, André Provensi and Gabriel Serafim C. Vieira deserve to be reminded as well for their friendship and support. Throughout this time, they were always available for a nice conversation. I must also thank Pedro H. P. Favero for all the help while working at the laboratory.

My big thanks to the Department of Mechanical Engineering and to the Federal University of Santa Catarina for making me the engineer I am today. I would like to thank the Professors and other co-workers who made part of my journey. My special thanks to Professor Lauro C. Nicolazzi for helping me multiple times.

Es ist nicht genug zu wissen - man muss auch anwenden.
Es ist nicht genug zu wollen - man muss auch tun.

(Knowing is not enough; we must apply.
Willing is not enough; we must do.)

(Johann Wolfgang von Goethe)

RESUMO

O presente trabalho introduz nova concepção de trocador de calor compacto unido por difusão, através da usinagem de placas em padrões de corte que permitem a criação de diversas geometrias de superfície de transferência de calor. Essa dissertação foca em uma superfície do tipo placa aletada, porém, essa nova concepção permite também a obtenção de geometrias inéditas de superfícies de transferência de calor, como canais tridimensionais e/ou intercomunicantes. Tais trocadores buscam ser mais compactos, mais eficientes (maior transferência de calor sem significativos aumentos de perda de carga) e melhor adaptados à operação em condições de entupimento. Os detalhes de desenvolvimento de um projeto de trocador de calor desse tipo, considerando superfícies com aletas do tipo pino, são apresentados. O presente trabalho engloba o desenvolvimento de um protótipo para testes desse tipo de superfície de transferência de calor (aletas do tipo pino). Tal protótipo foi desenvolvido objetivando obter correlações termo-hidráulicas para essa superfície, bem como permitir futuros testes em condições de deposição/incrustação. O desenvolvimento de uma bancada de testes também é apresentado. Resultados experimentais, aliados à implementação de um modelo de trocador de calor que considera condução interna e convecção em um dos ramais, permite a obtenção de dados referentes ao coeficiente convectivo no ramal de nova geometria. Dados de queda de pressão no núcleo tamém são obtidos. Os resultados são apresentados de maneira adimensionalizada, na forma do fator Colburn e do fator de atrito de Fanning. Parâmetros de desempenho são introduzidos e utilizados na comparação da nova geometria com duas superfícies comuns de transferência de calor.

Palavras-chave: trocador de calor compacto, união por difusão, superfície aletada, desempenho de superfície convectiva.

RESUMO EXPANDIDO

Introdução

Trocadores de calor compactos têm sido utilizados de forma cada vez mais frequente em diversas aplicações de engenharia, tendo destaque na indústria de processos. Tal classe de trocadores de calor vem à mente sempre que a necessidade de alta efetividade e restrições de espaço se fazem presentes. Dentro dessa classe, destacam-se os trocadores de calor unidos por difusão, fabricados através da união de placas metálicas previamente usinadas com uma geometria específica para formar canais. O processo de união por difusão permite que as placas se unam a nível microscópico, possibilitando que as microestruturas de placas vizinhas cresçam conjuntamente, eliminando a superfície de separação. Assim sendo, forma-se um único núcleo contínuo com propriedades semelhantes às do material de base. Até hoje, os canais de trocadores de calor unidos por difusão têm sido majoritariamente feitos através do ataque fotoquímico das placas, o que cria canais de seção semicircular. A esse tipo específico de trocador de calor (fabricado utilizando ataque fotoquímico) dá-se o nome de trocador de calor de circuito impresso ou PCHE (do inglês, *Printed Circuit Heat Exchanger*).

Objetivos

O presente trabalho tem por objetivo principal desenvolver nova técnica de fabricação de núcleo trocador de calor compacto unido por difusão, criando assim uma nova classe desse tipo de equipamento, a qual poderá ser utilizada pela indústria e representar uma solução competitiva ao mercado. Dentre os objetivos específicos, destaca-se projetar uma nova concepção de núcleo de trocador de calor, construir um protótipo para testes, montar uma bancada experimental para testar o protótipo, encontrar correlações termo-hidráulicas para a nova superfície de transferência de calor e comparar a nova superfície a soluções comuns de mercado. A nova bancada deverá, primeiramente, permitir a condução de testes com o intuito de se obter correlações termo-hidráulicas. Conforme delineado no trabalho, ao longo do desenvolvimento da nova concepção, surgiu o interesse de testá-la em condições de incrustação. Portanto, tal bancada deverá ser apta para esse tipo de teste.

Materiais e Métodos

Para o desenvolvimento do protótipo, placas metálicas foram usinadas por corte a jato d'água e posteriormente submetidas a um processo de união por difusão. Posteriormente, fresamento por comando numérico foi utilizado para a obtenção da geometria final da superfície de transferência de calor a ser estudada[1]. A bancada foi construída com equipamentos disponíveis no laboratório. Testes foram feitos com o trocador de calor operando em regime permanente sob diversas condições de operação. Durante os testes, as temperaturas nas entradas e saídas do trocador de calor foram monitoradas, assim como as quedas

[1] O processo de fresamento foi utilizado apenas no protótipo por conta de requisitos específicos do projeto e não faz parte do método de fabricação desenvolvido. Trocadores de calor fabricados conforme delineado no texto não deverão necessitar de operações de usinagem posteriores ao processo de união por difusão, salvo, eventualmente, nas regiões dos difusores e bocais.

de pressão no núcleo. As vazões volumétricas foram aferidas por medidores eletromagnéticos. Todos os testes foram feitos com água em ambos os ramais. Os dados experimentais foram usados para a determinação da taxa de transferência de calor e da condutância térmica. Como um dos ramais do trocador de calor possía canais retos, sua resistência convectiva foi modelada. A resistência condtiva no núcleo também foi calculada. Assim sendo, a resistência térmica no ramal de nova geometria e, por conseguinte, o coeficiente convectivo médio, puderam ser obtidos. Os resultados foram então adimensionalizados na forma do fator de Colburn. Similarmente, as variações de pressão na entrada e na saída do núcleo foram calculadas, para a queda de pressão apenas no interior do núcleo poder ser obtida. Os dados foram adimensionalizados na forma do fator de atrito de Fanning.

Resultados e Discussão

Os valores obtidos do fator de Colburn e do fator de atrito foram apresentados como funções do número de Reynolds, e funções foram ajustadas a partir dos resultados. Assim sendo, uma correlação convectiva foi obtida para uma superfície até então inédita nos trabalhos científicos. Os dados de condutância térmica foram analisados para se avaliar a importância relativa de cada resistência térmica elementar do trocador de calor. Posteriormente, parâmetros de desempenho foram utilizados para comparar a nova geometria com duas geometrias comuns de superfície de transferência de calor: canais retos e em zigue-zague, ambos com seção transversal quadrada. Os resultados mostraram que, uma vez determinados os parâmetros de operação (vazão mássica, queda de pressão e número de unidades de transferência do ramal), a nova geometria opera a um menor número de Reynolds em comparação às duas outras superfícies. Verificou-se, também, que a nova geometria demanda uma maior área de seção transversal de escoamento, o que está de acordo com o resultado anterior (para uma mesma vazão mássica, o número de Reynolds cai se a área de seção transversal de escoamento aumenta). Assim sendo, espera-se que trocadores de calor com essa nova geometria possuam seções transversais maiores do que trocadores de calor com as duas outras geometrias. Os resultados mostraram ainda que, em termos de volume total de trocador de calor, a presente geometria apresenta resultado intermediário entre ambas as geometrias de referência, sendo os canais em zigue-zague os que apresentam melhor resultado (menor volume). Visto que a seção transversal de escoamento da nova geometria aqui proposta é maior do que a da geometria de canais retos, o fato de o volume de fluido ser menor significa que o trocador de calor aqui proposto seria muito mais curto do que o trocador de calor de canais retos. De forma geral, percebe-se que para a condição de queda de pressão prescrita ser respeitada, o trocador de calor precisa de um número de Reynolds mais baixo, o que deve ser alcançado através de uma maior área de seção transversal. No entanto, a melhora na convecção faz o trocador de calor ser mais curto ao ponto de o volume final ser menor do que o do trocador de calor de canais retos.

Considerações Finais

O presente trabalho introduziu uma nova concepção de trocador de calor compacto unido por difusão que pode ser utilizada em aplicações práticas da indústria. Obteve-se, no trabalho, uma correlação convectiva que poderá auxiliar engenheiros a desenvolver futuros projetos, porém, mais do que isso, uma nova forma de se construir trocadores de calor foi apresentada. Assim sendo, o projetista tem a liberdade de usinar placas metálicas

como for conveniente, de forma a criar canais com maior liberdade dimensional. Portanto, tem-se aqui uma ferramenta de grande valia no desenvolvimento de trocadores de calor compactos.

ABSTRACT

This monograph introduces a novel conception of compact, diffusion bonded heat exchanger. Careful machining of plates followed by ordered stacking and diffusion bonding allows the designer to produce a multitude of heat transfer surfaces with multiple features. This work focuses on a pin-fin surface, however, this new conception allows the creation of novel surface geometries, including, for instance, intercommunicating and/or three-dimensional channels. The engineer can work with the new design possibilities to search for heat transfer surfaces which are more compact, more efficient (with higher heat transfer capabilities without significant increase in pressure drop) and less prone to fouling effects. The development of a feasible, applicable heat exchanger with pin-fin geometry is presented, showing that this new conception can, in fact, be applied in practical situations. This work also presents the design and manufacturing of a prototype, with similar heat transfer surface geometry (pin fins) for the development of thermal and hydraulic correlations, as well as future testing under fouling conditions. A new workbench for such kind of testing was developed, and the details regarding it are presented as well. Experimental results are used as inputs to a thermal model, allowing the convective coefficients of the new heat transfer surface to be obtained. Core pressure drop data are also obtained. The results are non-dimensionalized and presented in the form of Colburn factor and friction factor. Finally, performance parameters are used to compare the new geometry to two common heat transfer surfaces.

Keywords: compact heat exchanger, diffusion bonding, pin-fin surface, heat exchanger performance.

LIST OF FIGURES

LIST OF TABLES

LIST OF ABBREVIATIONS AND ACRONYMS

HPD	High Pressure Drop
Labtucal	Laboratório de Tubos de Calor (*Heat Pipes Laboratory*)
LPD	Low Pressure Drop
Ntu	Number of transfer units
OSF	Offset Strip Fin
PCHE	Printed Circuit Heat Exchanger
UFSC	Universidade Federal de Santa Catarina (*Federal University of Santa Catarina*)
UHF	Uniform Heat Flux
UWT	Uniform Wall Temeprature

LIST OF SYMBOLS

Latin symbols

A	Area [m^2]
A_b	Base Surface Heat Transfer Area [m^2]
A_c	Flow Cross-sectional Area [m^2]
A_{cf}	Fin Cross-section Area [m^2]
A_f	Heat Transfer Area of a Single Fin [m^2]
A_o	Control Volume's Cross-sectional Area [m^2]
A_s	Heat Transfer Area [m^2]
A_t	Total Heat Transfer Area of Extended Surface [m^2]
C	Thermal Capacity Flow Rate [W/K]
C_{min}	Minimal Heat Capacity Flow Rate [W/K]
C_{max}	Maximal Heat Capacity Flow Rate [W/K]
C_r	C_{min}/C_{max} Ratio
C_s	Heat Exchanger Cross-sectional Area [m^2]
D	Fin Diameter or Side Length [m]
D_e	Duct Hydraulic Diameter [m]
D_h	Subchannel Hydraulic Diameter [m]
d_h	Hudraulic Diameter [m]
F	Flow Arrangement Correction Factor
f_D	Darcy Friction Factor
G	Mass Velocity [kg/(m^2s)]
Gr	Grashof Number
Gz	Graetz Number (adimensional)
h	Specific Enthalpy [J/kg]
$\hbar$	Convection Heat Transfer Coefficient [W/(m^2K)]

$\hbar_b$	Bottom Convection Heat Transfer Coefficient [W/(m^{2}K)]
h_f	Fin Height [m]
h_l	Major Head Loss [J/kg]
h_{lm}	Minor Head Loss [J/kg]
h_{lT}	Total Head Loss [J/kg]
$\hbar_t$	Top Convection Heat Transfer Coefficient [W/(m^{2}K)]
j	Colburn Factor
K	Gnielinski's Correction Factor for Liquids
K'	Gnielinski's Correction Factor for Gases
k	Thermal Conductivity [W/(Km)]
K_c	Contraction Coefficient
K_e	Expansion Coefficient
K_l	Loss Coefficient
K_{td}	Flow Length Correction Factor
K_S	Additional Dimensionless Pressure Drop
L	Length [m]
l	Fin Length [m]
$\dot{m}$	Mass Flow Rate [kg/s]
m_c	Sarmiento's Adjustment Exponent
N	Stream Related Number of Transfer Units
N_f	Number of fins
Nu	Nusselt Number
Nu^*	Heat Transfer Enhancement Factor
P	Fin Perimeter [m]
P'	Total Heat Transfer Area to Flow Length Ratio [m]
p	Pressure [Pa]

P_A	Throughflow Area Parameter
P_f	Face Area Parameter
P_o	Operating Parameter [m^{-1}]
Pr	Prandtl Number
P_{fv}	Fluid Volume Parameter [m]
P_v	Volume Parameter [m]
Po	Poiseuille Number
$\dot{Q}$	Net Heat Flow Rate to the System [W]
q	Heat Transfer Rate [W]
q_f	Heat Transfer Rate of a single fin [W]
q''	Heat Flux [W/m^2]
R	Thermal Resistance [K/W]
Re	Reynolds Number
s	Fin Spacing [m]
S_x	Fin Spacing in Flow Length [m]
T	Temperature [°C] or [K]
t	Fin Thickness [m]
TC	Modified Gnielinski's Correction Factor
U	Global Heat Transfer Coefficient [$W/(m^2K)$]
u	Specific Internal Energy [J/kg]
V	Velocity [m/s]
$\overline{V}$	Mean Velocity [m/s]
$\mathcal{V}$	Volume [m^3]
$\mathcal{V}_s$	Fluid Volume [m^3]
$\dot{W}$	Net Work Rate Delivered by the System [W]
$\dot{W}_p$	Pumping Power [W]

x	Flow Length Coordinate [m]
x^+	Dimensionless Flow Length

Greek symbols

α	Thermal Diffusivity [m^2/s]
α_f	Fin Spacing to Height Ratio
α_V	Kinetic Energy Coefficient
β	Surface Area Density [m^{-1}]
β_f	OSF-Surface total flow length to fin length ratio
γ_f	Fin thickness to spacing ratio
δ	Thickness [m]
δ_f	Fin thickness to length ratio
ϵ	Aspect Ratio
ε	Heat Exchanger Effectiveness
η_f	Fin Efficiency
η_o	Overall Surface Efficiency
θ	Temperature difference between fin base and free stream [K]
μ	Dynamic Viscosity [Ns/m^2]
ν	Momentum Diffusivity
ρ	Density [kg/m^3]
σ	Porosity
σ_i	Core Inlet Area Ratio
σ_o	Core Outlet Area Ratio
τ	Shear Stress [Pa]
Ω	P'/A_c Ratio [m^{-1}]

Sub-indexes

c	Cold Side

h	Hot Side
i, in	Inlet
L	Laminar
lm	Logarithmic Mean
low	Lower Limit
max	Maximum
min	Minimum
o, out	Outlet
s	Smooth Duct
up	Upper Limit
w	Wall

CONTENTS

1 INTRODUCTION

Over the years, heat exchangers have become widely used in many fields such as automotive, refrigeration, power and so on. Shah, in the foreword of the monograph developed by Hesselgreaves (2000), stated that the importance of compact heat exchangers has been recognized in multiple industry segments due to several factors, among them packaging constraints, high performance requirements, low cost and the use of air or gas as one of the fluids in the exchanger.

Multiple conceptions of compact heat exchangers have been developed by the industry. Among them, the so-called printed circuit heat exchangers (PCHEs) reached the market mainly through the works of the British company Heatric Ltd. This company produces heat exchanger cores by chemically etching metal plates to form grooves. The etched plates are stacked on top of each other and subsequently diffusion bonded, so that channels are formed between the etched surface of one plate and the non-etched surface of a neighboring plate.

Due to their high heat transfer capabilities under extreme pressure and temperature conditions, as well as high compactness, printed circuit heat exchangers have been widely used in many fields, such as oil and gas processing, high temperature reactor intercooling and also as heat exchangers for supercritical carbon dioxide for Brayton cycles among other applications.

The Laboratory of Heat Pipes (Labtucal), at the department of Mechanical Engineering of the Federal University of Santa Catarina (UFSC) developed a new technique to manufacture diffusion bonded heat exchangers. The main feature consists of implementing a different machining process to substitute chemical etching. To this date, waterjet cutting has been used to form channels. In this new manufacturing method, separation plates have been used to separate the streams, since waterjet machining cuts plates throughout their entire thickness.

Based on the wide range of application possibilities of compact heat exchangers, this work focuses on the further development of diffusion bonded heat exchanger cores. The design flexibility of this new manufacturing technique is explored to create different heat transfer surfaces. The main goal here is to further explore machining patterns that allow the creation of more compact and efficient heat exchanger cores.

As a result of this work, new design possibilities utilizing the same manufacturing method were created and registered in patent form. A pin-fin heat transfer surface was designed, manufactured and submitted to testing.

Compared to the conventional designs, the here introduced heat exchanger conception has the main advantage of providing a better trade-off between flow turbulence, which increases the convective coefficient, and pressure drop. Moreover, better performance under high fouling conditions is expected.

1.1 GOALS

The present work aims to create a new type of heat exchanger core and to test its performance. Therefore, this monograph presents the design, manufacturing, testing and analysis phases of this new conception of heat exchanger core.

1.1.1 Main goal

The main goal of this work is to develop a new technique to manufacture compact heat exchanger cores, thus creating a new type of heat exchanger that could be used in industry and provide a competitive solution to the market.

1.1.2 Elementary goals

As elementary goals we have: design a new type of heat exchanger core, build a prototype, construct an experimental apparatus to test the prototype, find thermo-hydraulic correlations for the new heat transfer surface and compare the surface's performance to benchmark surfaces.

The new workbench must, at first, allow the conduction of basic experiments to test the prototype in order to obtain thermal and hydraulic correlations. Furthermore, the experimental apparatus must allow the conduction of future experiments under high-fouling conditions, since the new geometry is expected to perform well in such scenario.

1.2 STRUCTURE

This monograph is divided in eight chapters and also has three appendices. The first chapter simply brings the introduction, containing the motivation behind the study, main and elementary goals and the structure of the present work.

Chapter 2 brings a literature review on heat exchangers and heat transfer surfaces. It focuses on previously developed diffusion bonded heat exchangers and presents common fin geometries used in heat transfer applications.

Chapter 3 shows the development of the new conception of heat exchanger core, which has been registered in patent form. This chapter also brings a design suggestion of a heat exchanger based on the patented manufacturing technique. It is important to mention that this design does not correspond to the tested prototype, since it would not allow appropriate testing under fouling conditions.

Chapter 4 shows the development and manufacturing of the prototype that was actually tested, and also describes the workbench that was built to allow the prototype to be tested.

Chapter 5 brings the basics of heat exchanger analysis and modelling, which encompasses thermal and hydraulic aspects of heat exchangers.

Chapter 6 shows ways to evaluate heat exchanger performance, so that different heat transfer surfaces can be compared for a specific set of operating constraints.

Chapter 7 shows experimental results, brings correlations for the Colburn factor and friction factor based on the experimental data and compares the new heat transfer surface to two othe common benchmark surfaces.

Chapter 8 reviews the achievement of all goals and suggests further studies.

Appendix A brings raw measured data of all tests, whereas appendix B shows the metrological procedure used to calculate measured physical quantities. Appendix C brings additional figures that were not introduced in chapter 7.

2 LITERATURE REVIEW

In this chapter, the most important literature information needed for the development of the present work is given. Since diffusion bonding is a particularly useful manufacturing technique to fabricate compact heat exchangers, the first section of this chapter will be dedicated to exchangers manufactured using this technique. Afterwards, other common geometries of compact heat exchangers, so far not achievable by diffusion bonding, will be presented. Correlations for the calculation of the heat transfer coefficient and the friction factor for various geometries will then be presented.

Before explicitly presenting the different conceptions of compact heat exchangers, it is important to mention that Shah and Sekulic (2003) state that heat exchangers are classified as compact according to reference values of the heat transfer area density, defined by the authors as the ratio of the total heat transfer area to the total fluid volume of the corresponding stream:

$$\beta := \frac{A_s}{V_s} \tag{2.1}$$

In the case of vapor or gas, compactness is achieved for values greater or equal to $700\text{m}^2/\text{m}^3$, whereas in the case of a liquid or in the presence of phase change, the threshold value is $400\text{m}^2/\text{m}^3$.

2.1 DIFFUSION BONDED HEAT EXCHANGERS

Diffusion bonded heat exchangers are manufactured by orderly stacking previously machined plates and submitting the plates to a diffusion bonding process. This process allows the microstructure of each plate to grow into the microstructure of the neighboring ones on a microscopic level. This makes the interfaces between plates to vanish and forms a monolithic core. The machining process prior to diffusion bonding creates grooves and/or channels that allow fluid flow.

Two main types of diffusion bonded heat exchangers exist: Printed Circuit Heat Exchangers (PCHE) and Machined Plate Heat Exchangers. The former variation was the first one to be developed and is also the most commonly employed solution. The latter variation arises from recent studies developed at the Federal University of Santa Catarina (UFSC), more specifically at the Heat Pipes Laboratory (Labtucal).

2.1.1 Printed Circuit Heat Exchangers

The most common type of diffusion bonded heat exchanger is manufactured by creating fine grooves on plates through chemical etching. The plates are stacked and then diffusion bonded (SHAH; SEKULIC, 2003). Such devices are called Printed Circuit Heat Exchangers (PCHE) and were first introduced to the market by British company Heatric Ltd.

Figure 1 – (a) S-shaped and (b) zigzag fins.

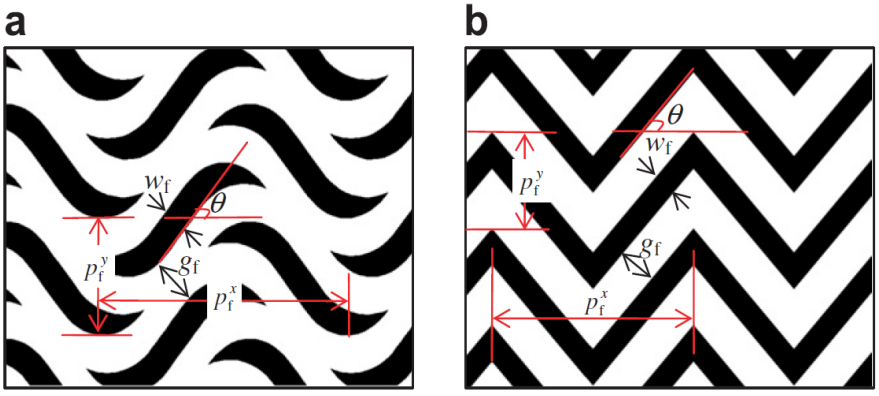

Ngo et al. (2007)

Such construction technique allows the designer to obtain various flow paths by chemically etching the grooves with the desired geometry. The most basic solution would be to create straight channels. The etching process creates grooves with semi-circular cross-section. Since internal convection in straight ducts has been studied by many researchers outside the context of printed circuit heat exchangers, this topic will be covered in a separate section.

Ngo et al. (2007) tested printed circuit heat exchangers with zigzag and S-shaped fins. Two prototypes were built by chemically etching flow channels and diffusion bonding plate stacks. Both fin geometries are presented in figure 1. The authors tested surfaces with a fin angle of 52°. In both cases, the fin gap, denoted by g_f, was $1,31$mm, whereas the fin depth was $0,94$mm. It is important to bear in mind that, when implementing the dimensionless results, the same fin angle and gap-to-depth ratio must be kept. The authors recommend, for both fin geometries, correlations in the form

$$Nu = CRe^m Pr^n \tag{2.2}$$

where C, m and n are constants given in table 1. For the friction factor, the authors provide

$$f = ARe^b \tag{2.3}$$

where constants A and b are given in table 2.

The correlations for S-shaped fins are valid for $3,5 \times 10^3 < Re < 2,3 \times 10^4$, whereas the ones for zigzag fins are valid for $3,5 \times 10^3 < Re < 2,2 \times 10^4$. For both fin geometries, the thermal correlations are valid for $0,75 < Pr < 2,2$.

Tsuzuki, Kato, and Ishiduka (2007) performed numerical simulations to analyze thermal and hydraulic performance of S-shaped fins, such as shown in figure 2a. A top view of the heat transfer surface is presented in figure 2b. As evaluation criteria, the authors used heat transfer rate per unit volume and pressure drop per unit length. For the final comparison, a total of five different fin geometries were used, including plain zigzag

Table 1 – Constants for equation 2.2.

	S-shaped fins	Zigzag fins
C	$0,1740 \pm 0,0118$	$0,1696 \pm 0,0144$
m	$0,593 \pm 0,007$	$0,629 \pm 0,009$
n	$0,430 \pm 0,014$	$0,317 \pm 0,014$

Ngo et al. (2007)

Table 2 – Constants for equation 2.3.

	S-shaped fins	Zigzag fins
A	$0,4545 \pm 0,0405$	$0,1924 \pm 0,0299$
b	$-0,340 \pm 0,009$	$-0,091 \pm 0,016$

Ngo et al. (2007)

Figure 2 – (a) S-shaped fin geometry and (b) Fin Arrangement.

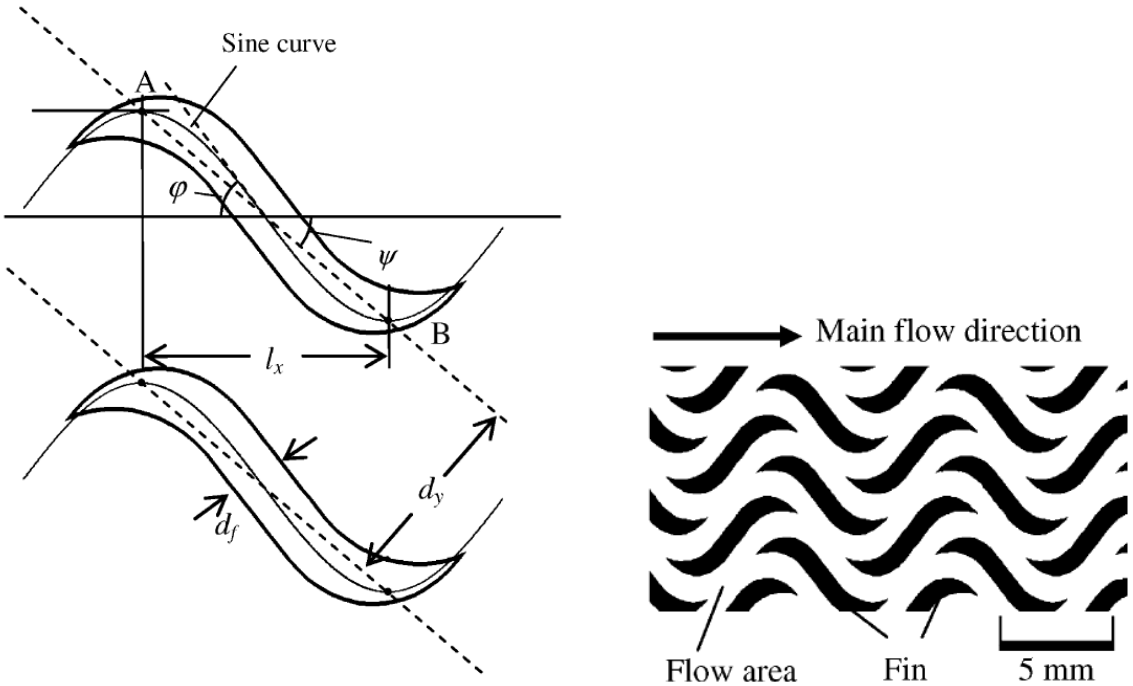

(a) (b)

Tsuzuki, Kato, and Ishiduka (2007)

channels. Figure 3 shows heat transfer rate per unit volume plotted against pressure drop per unit flow length for all five surface geometries. Points represented by the same symbol represent the same basic fin structure, but different fin angles. The authors concluded that *at the same fine angle of 52°, the new flow channel configuration reduces the pressure drop to one-fifth that of the conventional zigzag flow channel configuration while maintaining equal heat transfer performance.*

Figure 3 – Heat transfer rate per unit volume vs. pressure drop per unit length.

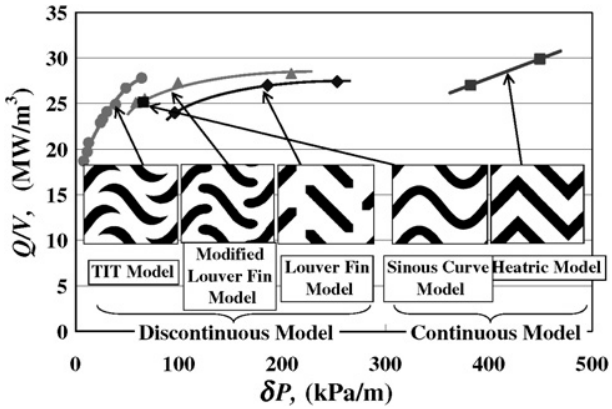

Tsuzuki, Kato, and Ishiduka (2007)

Figure 4 – Trapezoidal periodic unit.

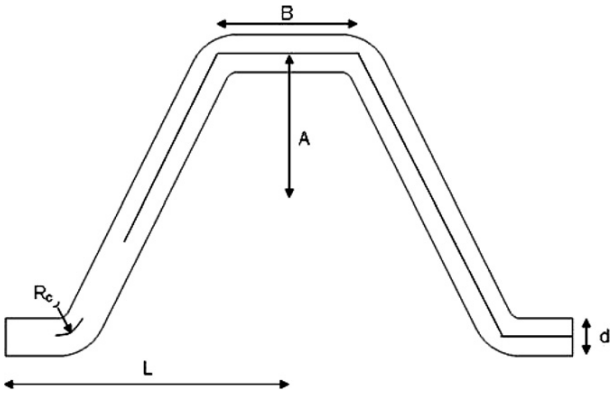

Gupta et al. (2008)

Gupta et al. (2008) performed numerical simulations to study the thermohydraulic performance of channels with a periodic trapezoidal flow path, such as shown in figure 4. The authors considered values of B/L varying from 0 to 1. Taking $B/L = 0$ corresponds to the limit case of a zigzag flow path, whereas $B/L = 1$ generates 90° corners. Multiple cross-sections (triangular, circular, semi-circular and square) were studied. Only fully developed laminar flow was considered, with Reynolds number up to 200. To draw conclusions from the results, the authors considered heat transfer and pressure drop enhancements when comparing trapezoidal channels to straight channels with the same cross-section, obtained by making $A = 0$. Regardless of the cross-section, trapezoidal channels present increased heat transfer and pressure drops than their straight channel counterparts. Results show that the triangular cross-section is the best performer, when considering augmented heat transfer compared to increased pressure drop.

Kim et al. (2008) proposed the use of airfoil shaped fins inside a PCHE. The authors performed numerical simulations, whose results show that, compared to zigzag channels, the heat transfer rate per unit volume was almost the same, whereas the pressure drop was

Figure 5 – Airfoil geometry and fin positioning.

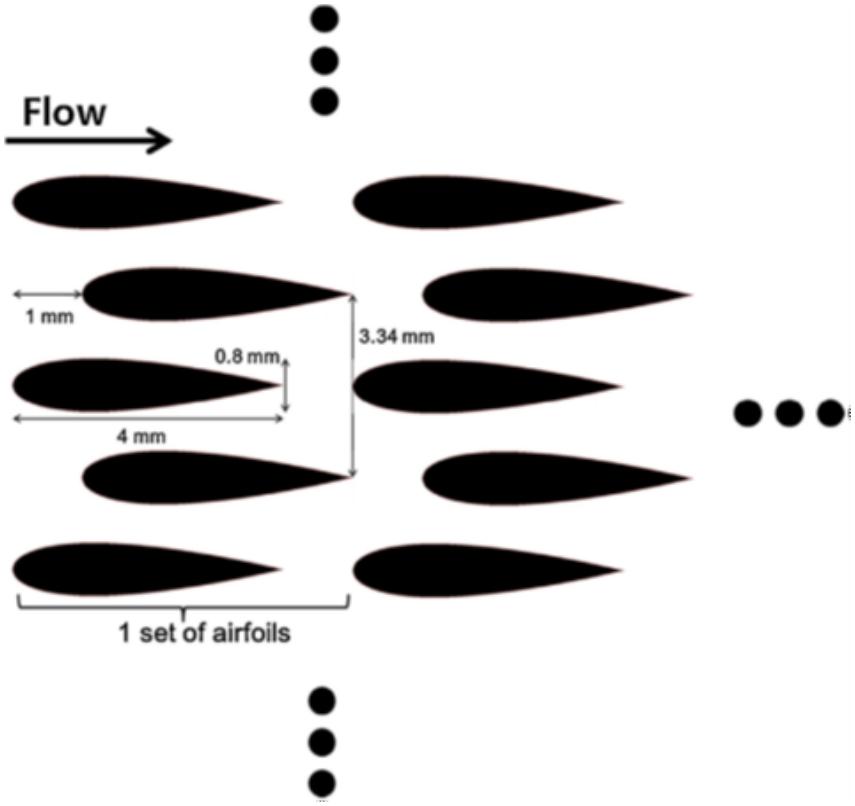

Yoon, NO, and Kang (2014)

reduced to one-twentieth of the benchmark value. The authors, however, did not develop correlations for the new geometry.

Lee and Kim (2013) performed numerical simulations to compare various channel cross-sectional shapes and configurations of zigzag printed circuit heat exchangers. The authors considered semicircular, rectangular, trapezoidal and circular cross-sections. Four channel configurations were also considered. The authors found that the rectangular channels have the highest thermal, but lowest hydraulic performance. The circular channel shows the lowest thermal performance.

Yoon, NO, and Kang (2014) developed thermo-hydraulic correlations for an airfoil PCHE by implementing Computational Fluid Dynamics (CFD). The correlations are applicable for Reynolds numbers from 0 to 150000. The authors used the minimal cross-section to obtain the hydraulic diameter and calculate flow velocity for the Reynolds number. The considered geometry is shown in figure 5. The fins are $0,5$mm high.

The authors recommend the following correlation for the Poiseuille number:

$$fRe = 9,31 + 0,028Re^{0,86} \tag{2.4}$$

This correlation is valid for the entire range of Reynolds number provided above. The Nusselt number is given by

$$Nu = 3,7 + 0,0013Re^{1,12}Pr^{0,38} \tag{2.5}$$

for Re up to 2500 and

$$Nu = 0,027 Re^{0,78} Pr^{0,4} \tag{2.6}$$

for $3000 < Re < 1,5 \times 10^5$. The two last correlations are valid for $0,6 < Pr < 0,8$.

Huang et al. (2019) published a review on flow and heat transfer characteristics of printed circuit heat exchangers (PCHEs). The authors state that PCHEs have high heat transfer ability, with a heat transfer area density of up to $2500 m^2/m^3$, are able to withstand high pressures, up to 60MPa and can work in temperatures as low as $-200°C$. According to the authors, the concept of printed circuit heat exchangers was first proposed by 1985 and has been commercialized by Heatric Ltd.

Hulse (2020) studied a chemically etched diffusion bonded heat exchanger in the dependencies of the Laboratory of Heat Pipes (Labtucal), at the department of Mechanical Engineering of the Federal University of Santa Catarina (UFSC).

2.1.2 Machined Plate Heat Exchangers

Recent developments made in Labtucal, UFSC provide a new method to manufacture diffusion bonded heat exchangers. Instead of chemical etching, waterjet cutting was applied to form channels. This new method was registered in the patent WO 2016/074048 Al (CARVALHO DOS SANTOS et al., 2016) and is presented in detail in the following paragraphs.

The channels of the heat exchanger, through which a fluid will flow, are formed as a result of the stacking and subsequent diffusion bonding of plates previously cut with a specific geometry, containing internal holes and channels. In the most basic conception, straight channels are machined onto plates, which are subsequently sandwiched between non-machined ones, which work as separation walls to avoid fluid mixture. This is presented in figure 6. Notice that some plates must have S-shaped channels to allow further header placement. Just as mentioned, in this conception, machined and non-machined plates are alternately stacked to form the channels, as shown in figure 7a (the non-machined plates are not shown in figure 6). The final stack can be seen in figure 7b.

The stack is subsequently diffusion bonded to form the core. Afterwards, the core is cut by electric discharge machining in the header regions to open the flow passages (figure 8a). This allows the installation of headers, such as shown in figure 8b.

Studies performed in such type of heat exchanger include the doctoral thesis of Mortean (2017). The author manufactured two crossflow heat exchangers. One of them was made of copper and is shown in figure 9, whereas the other one was made of stainless steel and in shown in figure 10.

Afterwards, a counterflow heat exchanger with square cross-sectional channels was manufactured in the laboratory[1]. The exchanger was modelled and tested by Carqueja

[1] This is the heat exchanger shown in figure 8b.

Figure 6 – (a) Plate geometry for straight channels and (b) plate geometry for S-shaped channels.

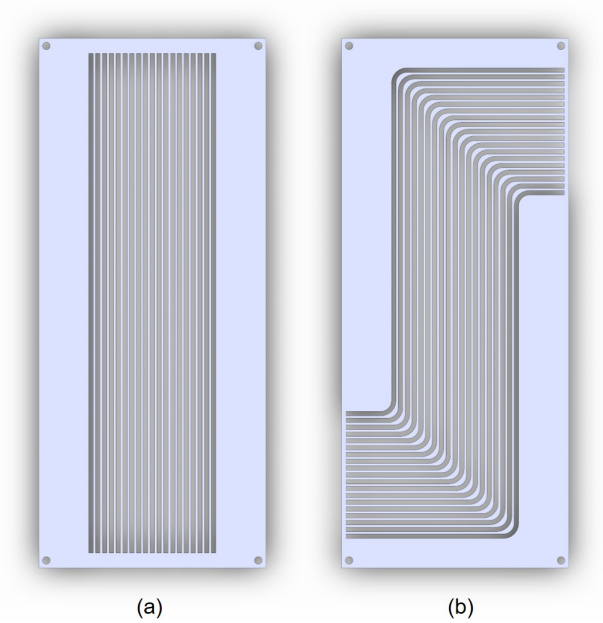

Figure 7 – (a) Plate stacking pattern and (b) complete plate stack ready for bonding.

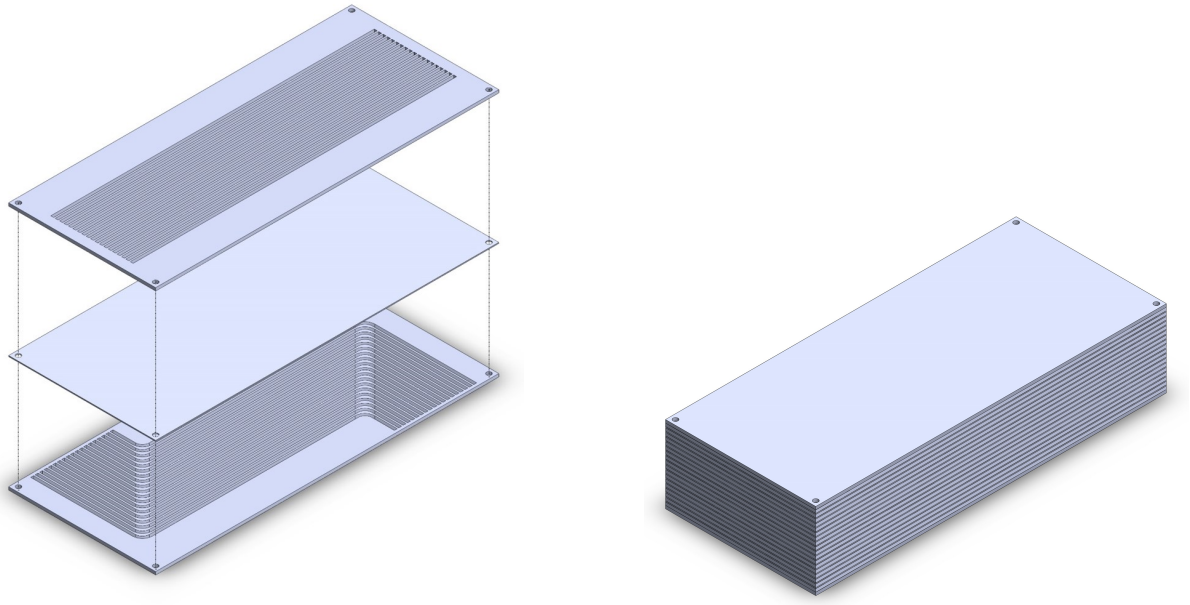

(a) (b)

Figure 8 – (a) Heat exchanger core after machining and (b) heat exchanger ready to be used.

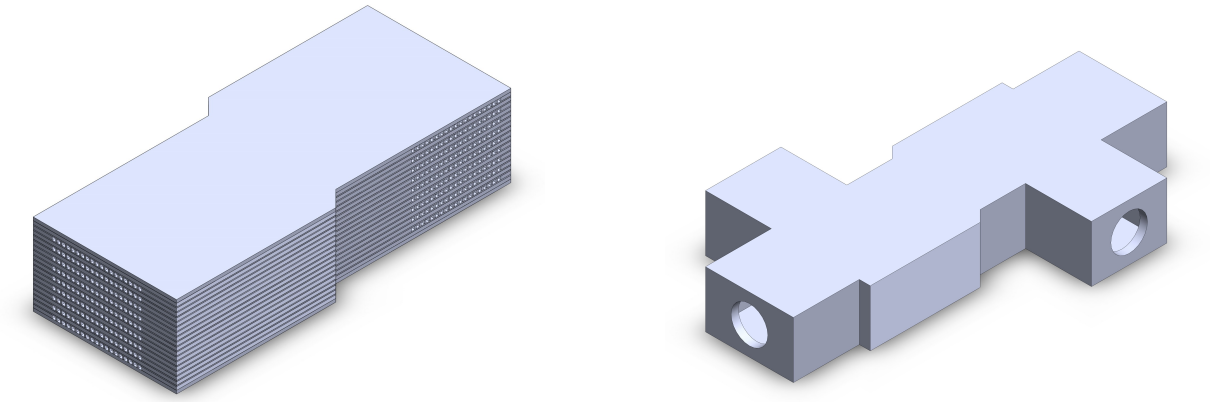

(a) (b)

Figure 9 – Copper heat exchanger.

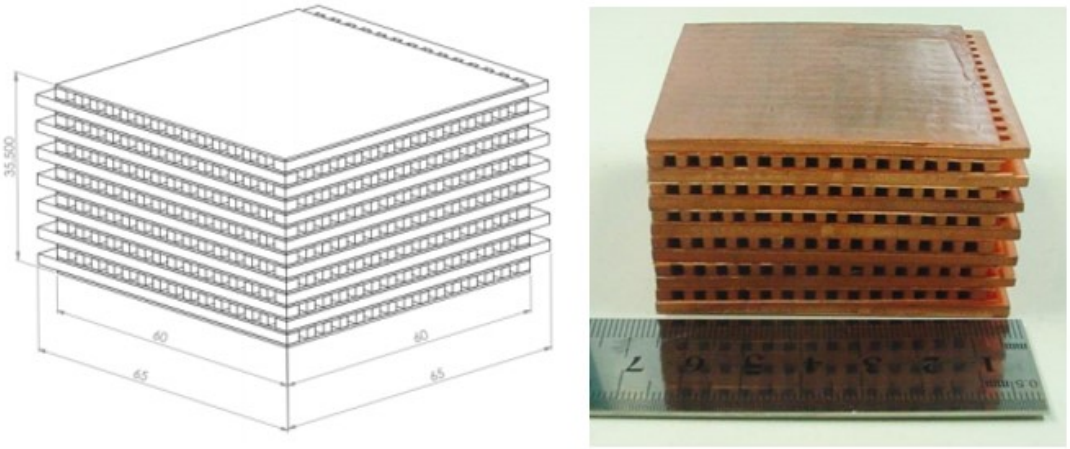

Mortean (2017)

(2017). Afterwards, Sarmiento, Soares, Carqueja, et al. (2020) used the experimental data obtained by Carqueja (2017) to model the same heat exchanger with a new convective correlation developed by Sarmiento, Soares, Milanez, et al. (2020). In the second study, header distribution was also analyzed.

Another counterflow heat exchanger was developed and built in the laboratory. This time, however, square cross-sectional zig-zag channels were designed. The heat exchanger was modelled and tested by Batista (2017).

Figure 10 – Stainless steel heat exchanger.

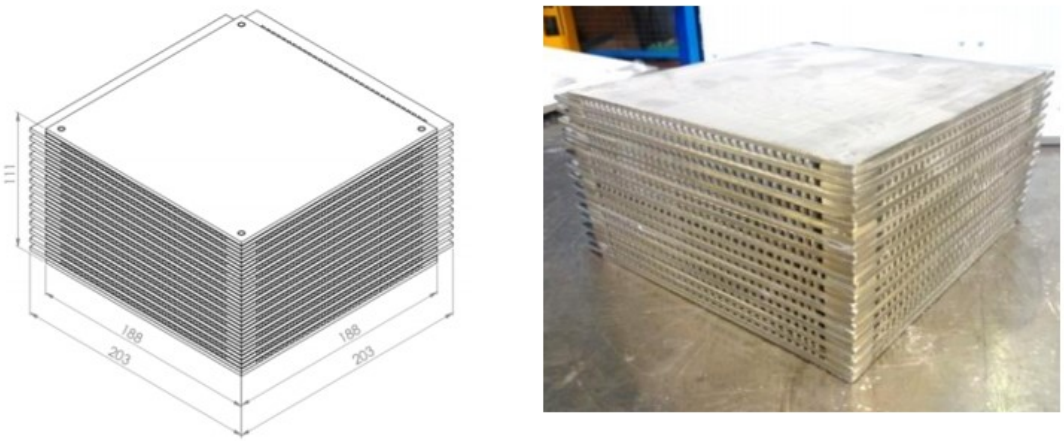

Mortean (2017)

2.2 PLATE-FIN HEAT EXCHANGERS

According to Hesselgreaves (2000), plate fin surfaces are by far the commonest of all compact types, being used for applications from aerospace air conditioning duties to oil refining. One of the basic fin surface types presents plain rectangular fins, which form straight flow channels. Such kind of surface is schematically shown in figure 11a.

Another common type of plate fin surface is the Offset Strip Fin (OSF) surface, shown in figure 11b. According to the author, among all fin surfaces presented in his work, this kind of surface is the highest performer, and hence has been the subject of most experimental research.

Figure 11 – (a) Plain rectangular fins and (b) offset strip fins.

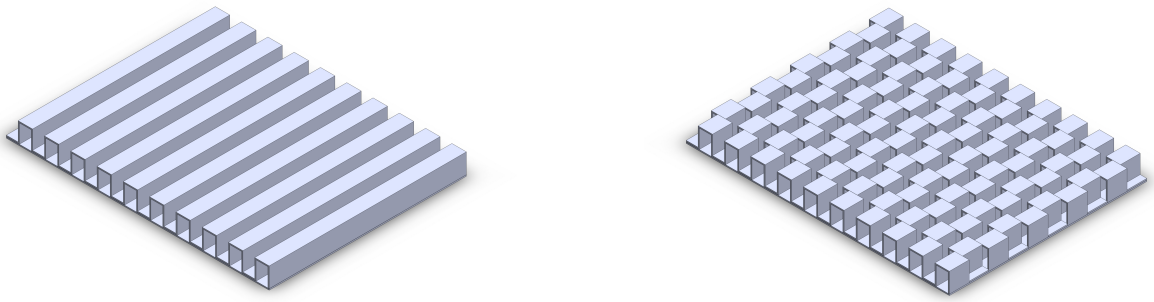

(a) (b)

2.2.1 Duct Flow

Regarding duct flow, Incropera et al. (2014) first introduces the correlations developed by Dittus and Boelter, Sieder and Tate and Hausen, which are well-known in the literature. Such correlations are, however, not anymore frequently used, given that other, more accurate ones, have been developed. Therefore, they will not be introduced here.

Gnielinski (1975) collected data provided by several already available studies and researched previously developed correlations for smooth ducts. The author showed the lack of accuracy in Hausen's correlation and then developed a new one based on the previous data provided by all gathered studies. The correlation was based on a former one developed by Petukhov, Kurganov, and Gladuntsov (1973), and is valid for $Re > 2300$ and $0,6 < Pr < 10^5$:

$$Nu = \frac{(f_D/8)(Re - 1000)Pr}{1 + 12,7\sqrt{f_D/8}(Pr^{2/3} - 1)} \left[1 + \left(\frac{d}{L}\right)^{2/3}\right] K \tag{2.7}$$

Here, K is a correction factor that considers temperature variations in liquids and is given by

$$K = \left(\frac{Pr}{Pr_w}\right)^{0,11} \tag{2.8}$$

where the subscript w indicates the property must be calculated at wall temperature. In the absence of a subscript, the property must be evaluated at the mean flow temperature. This correction factor is valid for $0,05 < Pr/Pr_w < 20$. For gases, K is substituted by the correction factor K', which is valid when $0,5 < T_m/T_w < 1,5$ and given by

$$K' = \left(\frac{T_m}{T_w}\right)^{0,45} \tag{2.9}$$

where T_m is the mean fluid temperature.

Gnielinski (1975) recommends the following correlation for the Darcy friction factor, which is attributed to Filonenko (1954):

$$f_D = (0,79 \ln Re - 1,64)^{-2} \tag{2.10}$$

The author states that this correlation effectively predicts the Darcy friction factor also within the validity range of the Blasius correlation

$$f_D = \frac{0,3164}{Re^{1/4}} \tag{2.11}$$

Although Gnielinski's correlation was developed for smooth ducts, Incropera et al. (2014) claim its applicability for rough ducts, if the appropriate value of f_D is used. Considering turbulent flow, the Darcy friction factor can be obtained by the Colebrook equation, as recommended by Fox, Mcdonald, and Pritchard (2014):

$$\frac{1}{\sqrt{f_D}} = -2,0 \log\left(\frac{e/d}{3,7} + \frac{2,51}{Re\sqrt{f_D}}\right) \tag{2.12}$$

Table 3 – Lower and upper limits of transition Reynolds number according to inlet geometry.

Inlet Geometry	Lower Limit	Upper Limit
Re-entrant	$Re_{low} = 2157 - 0,65\left(192 - \frac{x}{D}\right)$	$Re_{up} = 8475 - 9,28\left(192 - \frac{x}{D}\right)$
Square-edged	$Re_{low} = 2524 - 0,82\left(192 - \frac{x}{D}\right)$	$Re_{up} = 8791 - 7,69\left(192 - \frac{x}{D}\right)$
Bell-mouth	$Re_{low} = 3787 - 1,80\left(192 - \frac{x}{D}\right)$	$Re_{up} = 10481 - 5,47\left(192 - \frac{x}{D}\right)$

Tam and Ghajar (2006)

When calculating duct flow head loss, other expressions are available. Since the Colebrook equation is implicit, Fox, Mcdonald, and Pritchard (2014) suggest the following explicit equation, developed by Haaland (1983):

$$\frac{1}{\sqrt{f_D}} = -1,8\log\left[\left(\frac{e/d}{3,7}\right)^{1,11} + \frac{6,9}{Re}\right] \tag{2.13}$$

Results obtained from this expression differ from those obtained from the Colebrook equation up to about 2% for $Re > 3000$.

According to Hesselgreaves (2000), ducts with polygonal geometries usually have considerably sharp transition between laminar and turbulent flows, depending on the free stream conditions at entry. The author states that transition starts at Reynolds numbers between 1000 and 2000 and is effectively complete at about $Re = 4000$. Tam and Ghajar (2006) claim that the usual transitional flow Reynolds number, between 2300 and 10000 apply strictly to a very steady state and uniform entry flow with a rounded entrance. The authors also state that if the flow has a sharp entry with sudden contraction (typical of heat exchangers) and possibly even a re-entrant entrance, the transitional Reynolds number range will be considerably different. Equations for calculating the lower and upper limits of the transitional flow Reynolds number range are given in table 3 as a function of the tube's length to diameter ratio, for the three inlet geometries studied by the authors. The equations are valid for $3 < x/D < 192$.

Ghajar and Tam (1994) developed correlations for the Nusselt number considering both entrance and fully developed, forced and mixed convection heat transfer in the laminar, transition and turbulent flow regimes. They also compared their fully developed forced convection heat transfer data in the transition and turbulent regimes with the results predicted by the correlations developed by Gnielinski (1975) and Churchill (1977). Results showed excellent agreement for the bell-mouth inlet, however, the accuracy of these correlations deteriorated as the influence of inlet configuration on the heat transfer coefficient became more pronounced. According to them, the Nusselt number in transitional

Table 4 – Values of constants a, b and c of equation 2.14 for each inlet geometry.

	Re-entrant	Square-edged	Bell-mouth
a	1766	2617	6628
b	276	207	237
c	-0,955	-0,950	-0,980

Ghajar and Tam (1994)

Table 5 – Validity ranges of equation 2.14 for each inlet geometry.

	Re-entrant	Square-edged	Bell-mouth
Reynolds	$1700 \leq Re \leq 9100$	$1600 \leq Re \leq 10700$	$3300 \leq Re \leq 11100$
Prandtl	$5 \leq Pr \leq 51$	$5 \leq Pr \leq 55$	$13 \leq Pr \leq 77$
Grashof	$4000 \leq Gr \leq 2,5 \times 10^5$	$4000 \leq Gr \leq 2,5 \times 10^5$	$6000 \leq Gr \leq 1,1 \times 10^5$
μ/μ_w	$1,2 \leq \mu/\mu_w \leq 3,1$	$1,2 \leq \mu/\mu_w \leq 3,1$	$1,2 \leq \mu/\mu_w \leq 3,1$

Ghajar and Tam (1994)

flow can be expressed by

$$Nu_{tr} = \left[Nu_L + \exp\left(\frac{a - Re}{b}\right) + Nu_T^c \right]^c \tag{2.14}$$

where Nu_L is the Nusselt number for laminar flow and Nu_T for turbulent flow. In their work, the authors recommend the use of the following modified version of the Sieder and Tate correlation to calculate Nu_T:

$$Nu_T = 0,023 Re^{0,8} Pr^{0,385} \left(\frac{x}{D}\right)^{-0,0054} \left(\frac{\mu}{\mu_w}\right)^{0,14} \tag{2.15}$$

To develop a heat transfer correlation in entrance and fully developed regions of laminar flow, the authors used available mixed and forced convection data to fit a curve. The resulting correlation is

$$Nu_L = 1,24 \left[RePr\frac{D}{x} + 0,025(GrPr)^{0,75} \right]^{1/3} \left(\frac{\mu}{\mu_w}\right)^{0,14} \tag{2.16}$$

which is applicable when $3 \leq x/D \leq 192$, $280 \leq Re \leq 3800$, $40 \leq Pr \leq 160$, $1000 \leq Gr \leq 2,8 \times 10^4$ and $1,2 \leq \mu/\mu_w \leq 3,8$.

The values of constants a, b and c of equation 2.14 are summarized in table 4, whereas its validity ranges are presented in table 5 for each inlet geometry. It is worth mentioning that, according to the authors, the correlation is applicable, for all cases, when $3 \leq x/D \leq 192$.

Equation 2.14 is applicable to transition, forced and mixed convection, in the entrance and fully developed regions. The equation must be used with the appropriate set of constants for each inlet configuration. Thermal properties, when not evaluated at wall temperature, are evaluated at the bulk fluid temperature.

Table 6 – Distribution of data points.

Inlet Geometry	Mixed Convection	Forced Convection
Re-entrant	194	247
Square-edged	286	130
Bell-mouth	365	68

Tam and Ghajar (2006)

Table 7 – Average relative deviations of well-known convective correlations to experimental data points in transitional flow with forced convection.

Inlet Geometry	Gnielinski (f. developed)	Gnielinski (developing)	Churchill (f. developed)	Churchill (developing)	Ghajar and Tam
Re-entrant	10,65%	8,67%	28,35%	13,12%	9,02%
Square-edged	6,52%	15,72%	20,76%	21,17%	9,02%
Bell-mouth	2,48%	10,17%	10,72%	10,74%	4,99%

Tam and Ghajar (2006)

Table 8 – Average relative deviations of well-known convective correlations to experimental data points in transitional flow with mixed convection.

Inlet Geometry	Gnielinski (f. developed)	Gnielinski (developing)	Churchill (f. developed)	Churchill (developing)	Ghajar and Tam
Re-entrant	23,64%	8,67%	78,67%	37,61%	6,61%
Square-edged	45,64%	64,79%	70,58%	64,04%	6,42%
Bell-mouth	128,46%	185,44%	103,66%	200,72%	8,66%

Tam and Ghajar (2006)

Tam and Ghajar (2006) compared the accuracy of Gnielinski's, Churchill's and Ghajar and Tam's correlations in transitional flow for the same three inlet configurations of their previous study[2]. The correlations developed by the first two authors were tested both for the fully developed and for the developing case. It is worth mentioning that Churchill's correlation is not valid for the hydrodynamically developing case, only for the thermally developing and completely developed ones. The data were separated into two groups, one considering mixed convection and the other considering forced convection. The distribution of data into both groups is presented in table 6 for each inlet geometry considered.

In their study, the authors displayed the results both graphically and quantitatively, in form of tables containing statistically relevant quantities. For the sake of simplicity, only the average relative deviation[3] for each case will be given here. Results are presented in tables 7 and 8.

[2] This refers to Ghajar and Tam (1994).

[3] The relative deviation corresponds to the absolute value of the difference between the theoretical and the experimental value divided by the experimental value.

The authors state that *Gnielinski's and Churchill's correlations fail to give accurate predictions in the mixed convection region. This is directly due to the effect of free convection superimposed on the main flow, something Gnielinski and Churchill did not address in their works.*

Tam and Ghajar (2006) also studied the effects of secondary flow inside the tube due to the presence of a natural convection component. In the study, as an evaluation criterion, the ratio of top to bottom local heat transfer coefficients, $\hbar_t/\hbar_b$, was used. Values of this ratio close to the unity mean forced convection, otherwise mixed convection is present. More specifically, the authors considered a threshold value of 0,8, meaning that mixed convection is assumed when $\hbar_t/\hbar_b < 0,8$. The research showed that for re-entrant, square-edged and bell-mouth inlets, when the Reynolds number was greater than 2500, 3000 and 8000, respectively, the flows were dominated by forced convection heat transfer. Furthermore, in short tubes, equations for lower and upper limits of table 3 are not influenced by the presence of mixed convection. *However, as the flow travels the tube length required for the establishment of secondary flow, the lower transition region for all three inlets will be influenced by the presence of mixed convection* (TAM; GHAJAR, 2006). For bell-mouth inlets, both limits will be influenced by the presence of mixed convection.

Shah (1978) stated that compact heat exchangers often use interrupted heat exchange surfaces. Hence, new boundary layers form every time the free flow meets a new surface. Due to the small hydraulic diameters, characteristic of this class of heat exchangers, it is normal to find laminar flow conditions in such devices. Therefore, the developing laminar internal flow correlations are useful in the design of heat exchangers. The author used the following dimensionless coordinate

$$x^+ = \frac{x}{d_h Re} \tag{2.17}$$

and the following dimensionless pressure drop from 0 to x

$$\Delta p^* := \frac{\Delta p}{\frac{1}{2}\rho \overline{V}^2} = 4 f_{app} Re x^+ = 4 f_{app} \frac{x}{d_h} \tag{2.18}$$

in the study. In the equation, the apparent friction factor is used, which considers the total pressure drop from 0 to x. The author also presents an alternative way to express the dimensionless pressure drop:

$$\Delta p^* = 4 f Re x^+ + K_S(x) \tag{2.19}$$

Here, $K_S(x)$ represents an additional dimensionless pressure drop due to momentum change and accumulated increment in wall shear stress, valid for the range between developing and a fully developed flow.

Based on experimental data from a previous work, the author suggests the correlation

$$f_{app} = \frac{3,44}{Re\sqrt{x^+}} \tag{2.20}$$

valid for $51200 < Re < 113400$. The author states that *even at this high Reynolds number, for which the fully developed flow is turbulent, a laminar boundary layer is formed at the entry of a tube.*

In a further work, Tam, Tam, and Ghajar (2013) studied the friction factor in the entrance and fully-developed regions considering laminar and transitional flows for two inlet geometries. The authors tested available friction factor correlations and developed a new correlation for non-isothermal entrance and fully-developed flows, considering re-entrant and square-edged inlets.

2.2.2 Offset Strip Fins

Both fin types are described by the same geometric parameters. These include the fin thickness t, the passage height h_f, the fin spacing s, the fin length l and the total flow length L. These geometric parameters can be seen in Figure 12. The following dimensionless ratios are now defined:

$$\alpha_f \coloneqq \frac{s}{h_f} \tag{2.21}$$

$$\beta_f \coloneqq \frac{L}{l} \tag{2.22}$$

$$\delta_f \coloneqq \frac{t}{l} \tag{2.23}$$

$$\gamma_f \coloneqq \frac{t}{s} \tag{2.24}$$

Hesselgreaves (2000) recommends the use of Gnielinski's correlation for circular ducts when modelling plain fin surfaces in transitional and turbulent flows.

Figure 12 – Geometric parameters describing a plain fin or an offset strip fin surface.

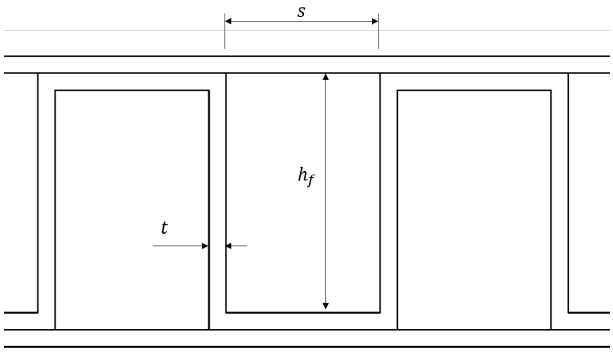

Figure 13 – Possible flow arrangements for an OSF surface.

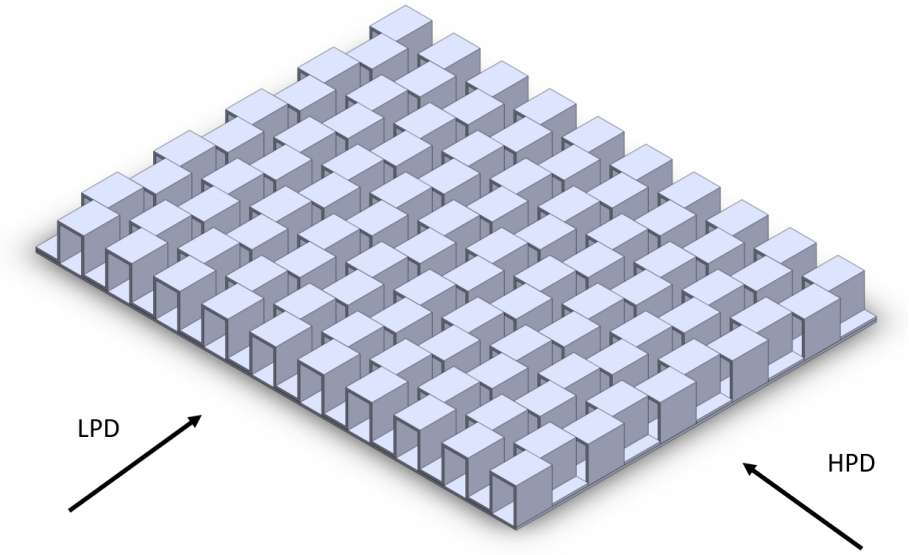

Dong et al. (2007) performed experimental studies on 16 types of offset strip fins and flat tube heat exchangers. The study involved air flow at Reynolds numbers varying from 500 to 7500. Based on the experimental data, the authors developed the following two equations for j (Colburn factor) and f:

$$j = 0,101 Re^{-0,189} \alpha_f^{-0,488} \delta_f^{0,479} \gamma_f^{-0,297} \beta_f^{-0,315} \tag{2.25}$$

$$f = 2,092 Re^{-0,281} \alpha_f^{-0,739} \delta_f^{0,972} \gamma_f^{-0,78} \beta_f^{-0,497} \tag{2.26}$$

Any flow orientation around an OSF surface is possible. When flow orientation is parallel to the fin plates, the so-called *Low Pressure Drop* (LPD) configuration is present. When the orientation is perpendicular to the fin plates, one has a *High Pressure Drop* (HPD) configuration. Both orientations are illustrated in Figure 3.

In a doctoral thesis, Muzychka (1999) used the asymptotic adjustment method to developed new correlations for f and j covering the entire spectrum from laminar to turbulent flow around offset strip fins. The author provides

$$f = \left\{ \left[\frac{Po \dfrac{d_h}{D_h}}{Re_{d_h}} + 1,328 \left(Re_{d_h} \frac{L_f}{d_h} \right)^{-\frac{1}{2}} \right]^n + \left[0,074 \left(Re_{d_h} \frac{L_f}{d_h} \right)^{-\frac{1}{5}} + \frac{Ht + \dfrac{st}{2}}{2L_f (H+s)} C_D \right]^n \right\}^{1/n} \tag{2.27}$$

The author states that values of n were found to vary between 1,3 and 5, whereas a value of $n \approx 3$ provides excellent correlation for the considered data. In the last equation, D_h is the hydraulic diameter of the subchannel and d_h is the hydraulic diameter of the OSF array. In the equation, $Po = f Re_{D_h}$ is the Poiseuille number in fully developed laminar

condition for the subchannel. Analytical results are available for Po. In the equation, C_D is the form drag factor, taken to be $C_D = 0,88$. For the Colburn factor, the author provides the expression

$$j = \left\{ \left[\left(\frac{Nu_{D_h}}{Re_{d_h} Pr^{\frac{1}{3}}} \frac{d_h}{D_h} \right)^5 + \left(\frac{0,641 f Re_{D_h}^{\frac{1}{3}}}{Re_{d_h}^{\frac{2}{3}}} \left(\frac{d_h^2}{D_h L_f} \right)^{\frac{1}{3}} \right)^5 \right]^{\frac{m}{5}} + \left[0,037 \left(Re_{d_h} \frac{L_f}{d_h} \right)^{-\frac{1}{5}} \right]^m \right\}^{1/m} \tag{2.28}$$

where m was found to vary between 2 and 5. According to the author, a value of approximately 7/2 provides excellent correlation for the data.

For offset strip fin surfaces, Hesselgreaves (2000) recommends correlations developed by Manglik and Bergles (1995), who studied previous correlations and gathered experimental data of airflow heat transfer in 18 different heat exchanger cores. The authors developed continuous expressions for f and j covering laminar, transitional and turbulent regimes:

$$f = 9,6243 Re^{-0,7422} \alpha_f^{-0,1856} \delta_f^{0,3053} \gamma_f^{-0,2659} \left(1 + 7,669 \times 10^{-8} Re^{4,426} \alpha_f^{0,920} \delta_f^{3,767} \gamma_f^{0,236} \right)^{0,1} \tag{2.29}$$

$$j = 0,6522 Re^{-0,5403} \alpha_f^{-0,1541} \delta_f^{0,1499} \gamma_f^{-0,0678} \left(1 + 5,269 \times 10^{-5} Re^{1,340} \alpha_f^{0,504} \delta_f^{0,456} \gamma_f^{-1,055} \right)^{0,1} \tag{2.30}$$

In their study, the authors defined the hydraulic diameter as

$$d_h = \frac{4 s h_f l}{2 \left(s l + h_f l + t h_f \right) + t s} \tag{2.31}$$

These correlations are valid for α_f varying from 0,134 to 1,0354, β_f ranging from 0,012 to 0,060 and γ_f ranging from 0,038 to 0,195. The authors considered Reynolds number varying from 120 to 10^4.

Zheng and Qi (2018) published a review of studies concerning offset strip fins and their applications. When considering single-phase flow, different ranges of α_f, δ_f, γ_f and Re were investigated in each study. The review published by Zheng and Qi (2018) is a valuable asset when searching for literature based studies of offset strip fins.

VanFossen (1982) studied convection in staggered arrays of short pin fins. The author was interested in convective cooling of turbine blades, which demands a low number of short pin fin rows. According to the study, pin fins are designated as short when the height to diameter ratio is up to 4. Because of the study's goals, the author considered height-to-diameter-ratios of 2 and 0,5, configuring therefore short pin fins. The study also claims that the local convective coefficient stabilizes after about eight rows of fins, which

is more than what is usually found in the trailing edges of gas turbines. Because of the application purposes of the study, in all tests, only four rows of pin fins were present. The author defined the Reynolds number as

$$Re_{d_h} = \frac{(\dot{m}/A_c)\, d_h}{\mu} \tag{2.32}$$

where the characteristic length d_h is the hydraulic diameter, defined as $d_h = 4V_s/A_s$. Here, V_s is the enclosed fluid volume and A_s is the total heat transfer area. In the definition of the Reynolds number, $A_c = V_s/L$ is the average flow area. The author defines the Nusselt number as

$$Nu = \frac{\bar{h} d_h}{k} \tag{2.33}$$

where $\bar{h}$ is the average heat transfer coefficient of the entire arrangement. The transverse pitch between the axes of two fins in a same row corresponds to two or four times the fin diameter. The axes of all fins in each row belong to the same plane. The distance between consecutive planes is called longitudinal pitch, whereas the relative longitudinal pitch refers to the ratio of longitudinal pitch to fin diameter. The fin rows were arranged in such a way that each pin axis is equidistantly located from the axes of all neighboring fins, whenever the fins were positioned perpendicularly to the endwalls (the author also tested inclined fins). The author developed the correlation

$$Nu = 0,153 Re^{0,685} \tag{2.34}$$

Şara (2003) studied convection in rectangular ducts with staggered square cross-sectional pin fins on one surface. The basic experimental set-up used by the author can be seen in Figure 4. The transverse distance ratio was kept constant at $S_z/D = 2,25$, whereas multiple longitudinal distance ratios (S_x/D) and clearance ratios (C/H) were tested. The channel had a total height of 80mm, so to obtain different clearance ratios, fins of different heights were used. The fins were positioned on top of a 2mm thick aluminum plate, which was placed on top of an electric heater.

The author used two definitions of Reynolds number. One of them involves the mean inlet velocity $\overline{V}$ and the duct's hydraulic diameter d_h, yielding

$$Re_{d_h} = \frac{\rho \overline{V} d_h}{\mu} \tag{2.35}$$

The other definition involves the maximum velocity V_{max} and the fin's side length D:

$$Re_D = \frac{\rho V_{max} D}{\mu} \tag{2.36}$$

In the last equation, the maximum velocity is given by

$$V_{max} = \overline{V} \frac{A}{A_{min}} \tag{2.37}$$

Figure 14 – Experimental set-up.

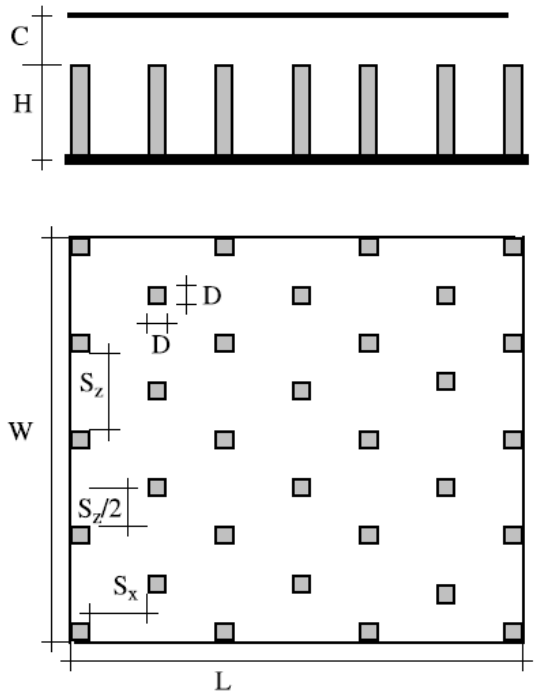

Şara (2003)

where A_{min} is the minimum flow area in the finned region. The author calls the first definition (equation 2.35) the *duct Reynolds number*, whereas the second one (equation 2.36) is called *pin Reynolds number*.

Similarly, the *duct Nusselt number* is defined as

$$\overline{Nu}_{d_h} = \frac{\bar{h} d_h}{k} \tag{2.38}$$

whereas the pin Nusselt number is defined as

$$\overline{Nu}_D = \frac{\bar{h} D}{k} \tag{2.39}$$

For the duct Nusselt number, the convective coefficient is calculated based on the duct's base area, whereas the pin Nusselt number is obtained by calculating the convective coefficient based on the total heat transfer area.

Considering the experimental data, the author found the following correlation for the duct Nusselt number as a function of the duct Reynolds number, Prandtl number, longitudinal spacing ratio and clearance ratio:

$$\overline{Nu}_{d_h} = 2,8358 Re_{d_h}^{0,58} \left(1 + \frac{C}{H}\right)^{-0,848} \left(\frac{S_x}{D}\right)^{-0,251} Pr^{1/3} \tag{2.40}$$

This correlation is valid for $10000 \leq Re \leq 34000$, $1,58 \leq S_x/D \leq 9,33$ and $0 \leq C/H \leq 1$.

The author correlates the pin Nusselt number to the pin Reynolds number in the form of the following correlation:

$$\overline{Nu}_D = mRe_D^n \tag{2.41}$$

In the last equation, m and n are functions of S_x/D and C/H. The results are given in Table 10.

Table 9 – Values of m and n for equation 2.41

C/H	S_x/D	m	n
1	1,58	0,201	0,547
	4,17	0,364	0,473
	9,33	0,168	0,569
0,6	1,58	0,723	0,415
	4,17	0,642	0,410
	9,33	0,182	0,575
0	1,58	0,524	0,404
	4,17	0,782	0,372
	9,33	0,4137	0,449

Şara (2003)

The pressure drop in the test section is given in terms of the Darcy friction factor. Şara (2003) presents the correlation below:

$$f_D = 11,944Re_{d_h}^{-0,101}\left(1+\frac{C}{H}\right)^{-2,05}\left(\frac{S_x}{D}\right)^{-0,582} \tag{2.42}$$

This expression is valid for the same variable ranges as the last one (equation 2.40).

To evaluate the heat transfer performance, the author compared the heat transfer coefficient of the plate-fin arrangements to that of a smooth duct under the constraint of same pumping power. To do this, the duct Nusselt number was used, so the same reference area would be employed. This allows one to define the *heat transfer enhancement factor*

$$Nu^* := \frac{\overline{Nu}_{d_h}}{\overline{Nu}_s} \tag{2.43}$$

where $\overline{Nu}_s$ is the smooth duct Nusselt number for the same pumping power as in the plate-fin configuration. The pumping power is proportional to $f_D Re_{d_h}^3$. Therefore, for the same pumping power, both in a smooth duct and in a plate-fin arrangement, one has

$$f_D Re_{d_h}^3 = f_{D,s} Re_s^3 \tag{2.44}$$

where the sub-index s refers to the smooth duct. The author states that the Darcy friction factor can be written as a function of the Reynolds number in the following functional form:

$$f_D = aRe^b \tag{2.45}$$

Applying equation 2.45 to both cases and substituting the results in equation 2.44, it is found that the Reynolds number of a smooth duct, for the same pumping power, as for a pin-fin arrangement with Reynolds number Re, is

$$Re_s = \left(\frac{a}{a_s}\right)^{1/(b_s+3)} Re_{d_h}^{\frac{b+3}{b_s+3}} \tag{2.46}$$

Based on equation 2.42, $a = 11,944\,(1 + C/H)^{-2,05}\,(S_x/D)^{-0,582}$ and $b = -0,101$. For smooth ducts, the author uses the following correlation:

$$f_{D,s} = 0,316 Re_s^{-0,25} \tag{2.47}$$

This allows one to obtain $a_s = 0,316$ and $b_s = -0,25$. Substituting the results for a, b, a_s and b_s into equation 2.46 yields

$$Re_s = 3,751 \left(1 + \frac{C}{H}\right)^{-0,746} \left(\frac{S_x}{D}\right)^{-0,212} Re_{d_h}^{1,054} \tag{2.48}$$

Hence, for a Reynolds number Re in the pin-fin arrangement, a smooth duct must have a Reynolds number Re_s given by the last equation so the pumping power would be the same for both ducts. In other words, for two ducts with the same cross section, one with fins and the other without, for the pumping power to be the same in both cases, the Reynolds numbers must be linked by equation 2.48. Once Re_s is obtained, the corresponding smooth duct Nusselt number can be calculated by the expression

$$\overline{Nu}_s = 0,0919 Re_s^{0,706} Pr^{1/3} \tag{2.49}$$

provided by the author. Then the pin-fin Nusselt number can be compared to $\overline{Nu}_s$. The author found that for all tests, the pin-fin arrangement presented a better performance than the smooth duct under the same pumping power constraint. In other words, in all cases $Nu^* > 1$. The author also verified that Nu^* increased when the Reynolds number decreased. Finally, it became evident that lower values of lontigudinal spacing to side length ratio lead to higher values of Nu^*. The same observation holds for lower values of clearance to fin height ratio. In other words, within the study ranges, longer and more numerous fins increase heat transfer when compared to shorter, more distanced ones. Overall, any pin fin configuration among the tested ones performs better than a smooth duct under the same pumping power constraint.

Jeng and Tzeng (2007) performed an experimental study on square pin-fin arrays to analyze heat transfer and pressure drop characteristics. The authors studied in-line and staggered arrangements, using the transient single-blow technique. This study considers three different values of relative longitudinal pitch and three different values of relative transverse pitch. The results allow one to understand the effects of varying both the relative longitudinal and transverse pitches. The authors also evaluated the performance of pin-fin arrays and compared different configurations.

3 NEW DESIGN

In this chapter, the heat exchanger, which is the subject of a patent developed in the frame of the present dissertation, is presented in detail. A full compact heat exchanger design is shown for illustration.

The previous manufacturing technique, presented in section 2.1.2, allows the designer to easily build counterflow, parallel flow and crossflow heat exchangers with different channel geometries, such as zigzag or sine channels. In such heat exchangers, the flow channels are always dimensionally limited to one plate, so the channel height always corresponds to the plate thickness. Therefore, the engineer, apart from the selection of plate thickness, could only control the two-dimensional design of the channels. This also means that intercommunications between channels could not be manufactured without subsequent machining procedures, such as drilling after the diffusion bonding process, which is impractical in such kind of geometry. This means that all implemented constructive variations were limited to layers with different channel patterns inside the core.

3.1 NOVEL CONCEPTION

In the present work, to avoid the two-dimensional limitations imposed by the fabrication process described in the last section, new plate machining and stacking patterns are proposed, enabling the creation of channels that allow internal flow in more than one dimension and/or channels with internal communications, so the flow stream can change its path from one channel to another. This means that the confinement between two separation plates is avoided, and new machining patterns are utilized. The developed conceptions are registered in patent form with deposit code BR 10 2020 017139 9.

Once separation plates are avoided, any internal channel geometry that can be divided into layers of feasible manufacturing and stacking could be used to form a core. This creates a higher design flexibility compared to the previous manufacturing method. After an iterative development, the first conception was obtained, and will be described in the next paragraphs.

For the design proposal presented in this monograph, the plates are conceived with basically only one geometric pattern for the core. This pattern is schematically represented, on a conception level, in figure 15. To form the core, each plate must be stacked rotated 180° relative to its neighboring ones. The stacking pattern can be seen in figure 16. The resulting core is shown in figure 17.

The machined plates are formed by longitudinal and transverse beams, such as shown in figure 18. As this new heat exchanger core has no separation plates, the walls are formed by the stacking and bonding of the longitudinal plate beams. Hence, intercommunicating channels for the fluid flow are created throughout the whole stack height. The plates' transverse beams create fins, which enhance heat transfer. The designer can work

Figure 15 – Geometric pattern of new conception.

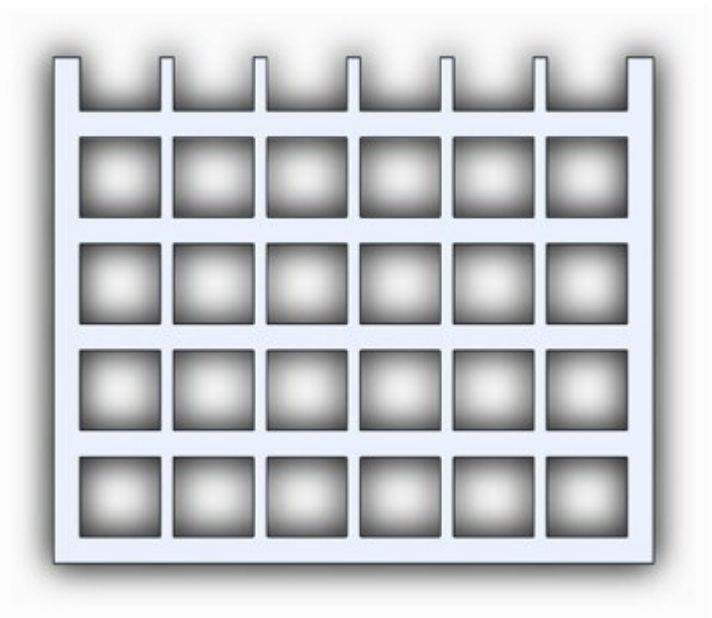

Figure 16 – Stacking pattern.

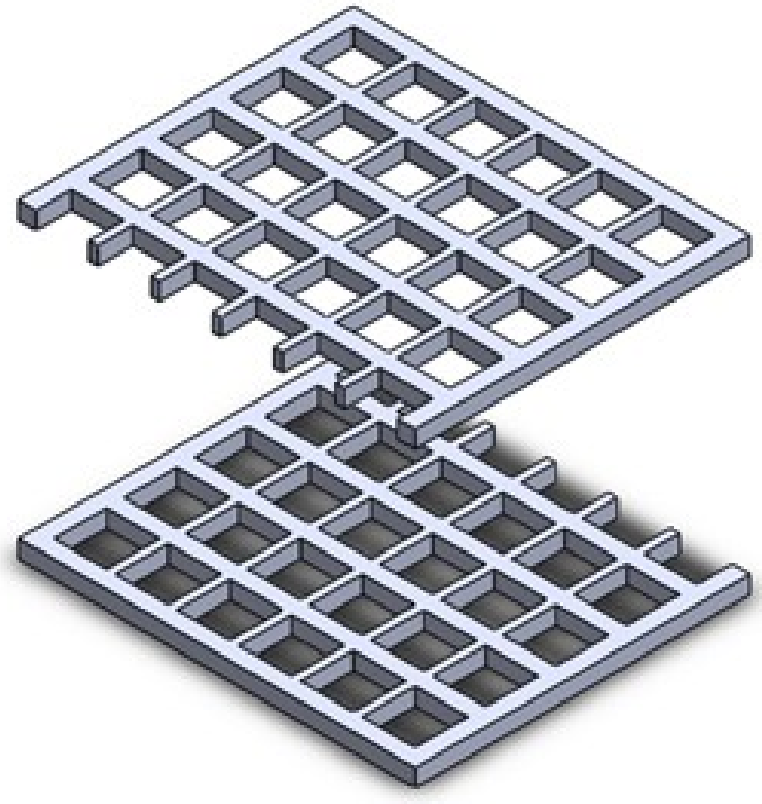

Figure 17 – Plate stack.

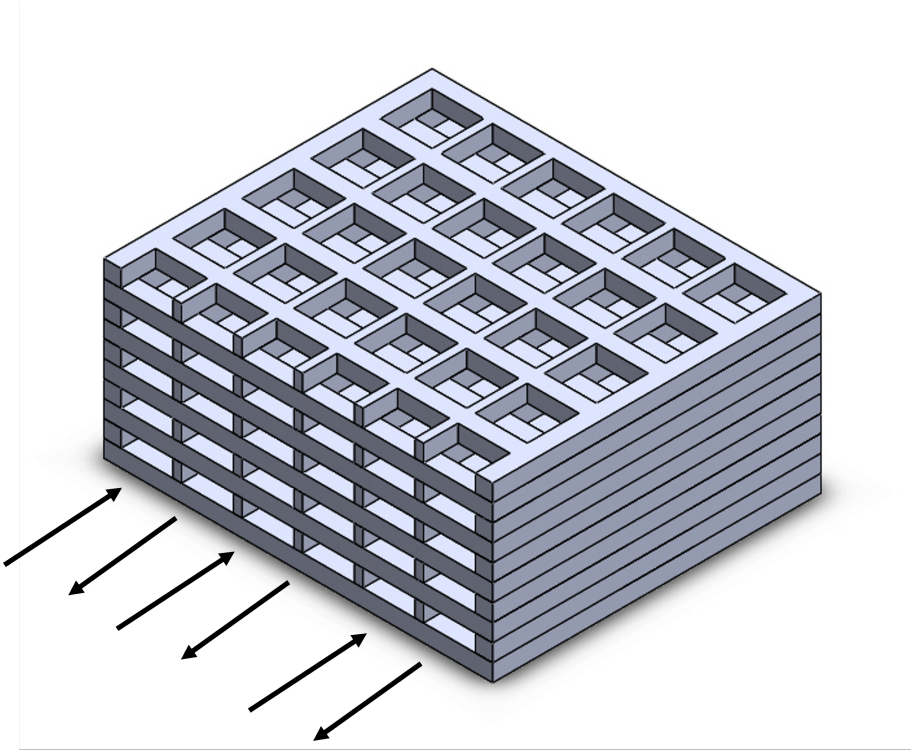

Figure 18 – Plate structure.

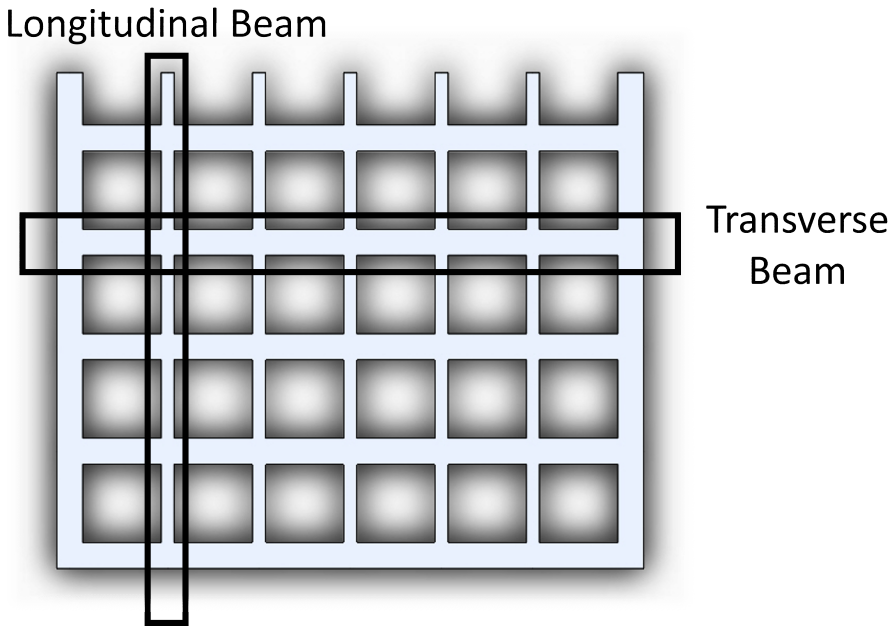

with the beams' dimensions to create different flow patterns inside the core. Figure 17 also shows arrows representing the flow directions of both streams when the core is used in counterflow arrangement. It can be recognized that the longitudinal beams form the separation walls.

A further illustration of the internal structure is shown in figure 19, which is the core from figure 17 cut along a longitudinal plane. The blue regions of the figure are the

Figure 19 – Internal view of plate stack.

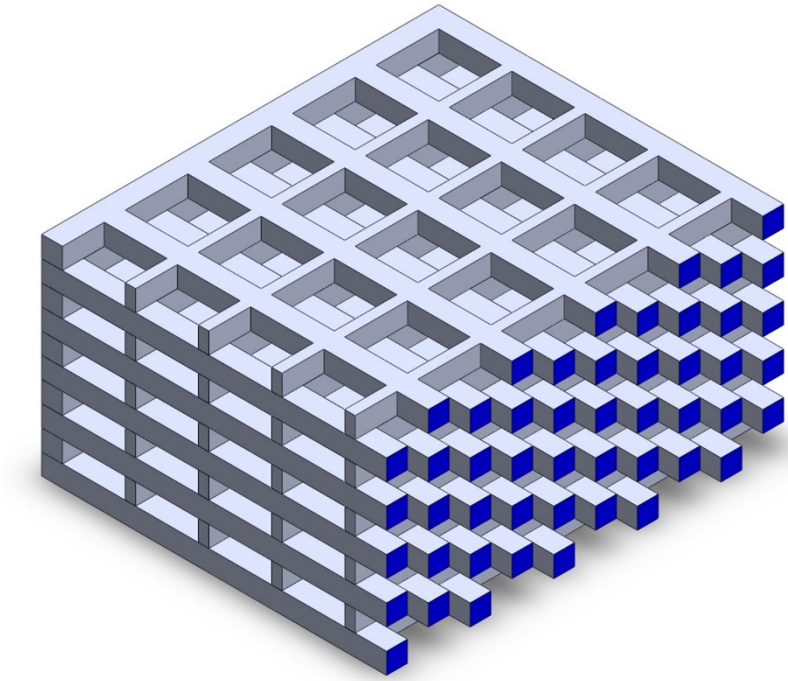

Figure 20 – Flow Pattern of new design conception. Cut view highlighted in figure 19.

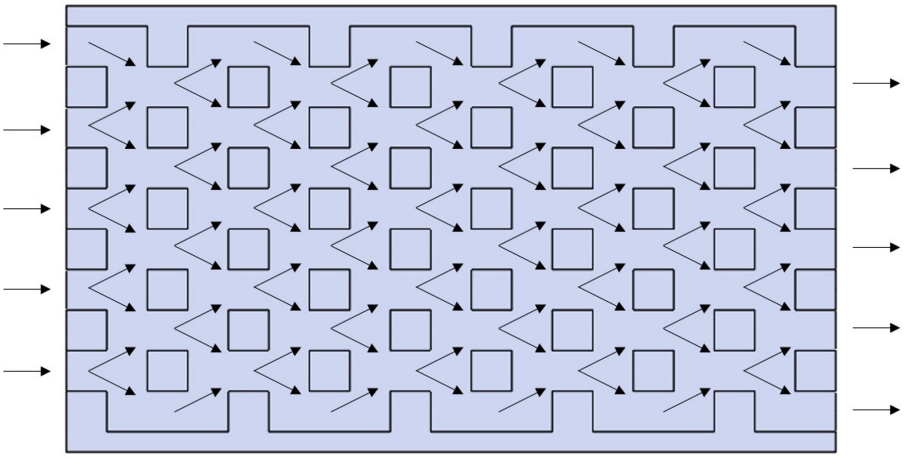

cross-sections of the transverse beams, which act as fins. The cut plane is parallel to the separations walls that are formed by the longitudinal beams. Therefore, the plane cuts only one of the streams. The flow pattern inside the heat exchanger is shown in figure 20, which represents a cut view similar to the one shown figure 19. Unlike figure 19, however, top and bottom plates are schematically shown in figure 20, creating a more realistic representation of an enclosed heat exchanger core. The top and bottom plates are not shown in the former figures to allow better observation of the core structure.

Figure 20 allows one to easily observe the multiple flow separations that occur each time the fluid meets a new fin. At such point, each separated stream meets another

separated stream from a neighboring flow passage. The upstream faces of the fins provide high values of heat transfer coefficient, whereas the sharp corners increase turbulence.

An interesting characteristic of such core geometry is that instead of having long channels, only short flow passages are present, and each row of flow passages is separated to the neighboring rows by plena[1]. In other words, the flow passages are intercommunicated. Thus, the fluid can freely move around the fins, so that if one passage is blocked, the fluid naturally finds its way around the other ones. In the case of regular channels, if a channel is blocked anywhere in its length, the entire channel is affected. In the present geometry, however, blocking one passage only compromises a small portion of the heat transfer surface.

In normal conditions, fouling is expected to occur evenly spread across the stream's width, so having a small number individually blocked passages inside a heat exchanger is not a probable scenario. One should bear in mind that fouling is frequently related to the deposition of calcium carbonate, which occurs as the water temperature rises along the stream[2]. Deposition, in this case, occurs slowly and progressively, forming a layer of solute along the surface. Nevertheless, interest regarding this surface's behavior under fouled conditions rose during its conception, given the flow behavior described in the last paragraph.

The internal structure of the core allows its use either in parallel or counterflow arrangements. Naturally, the necessary installation of headers might demand specific, individual geometric features that could imply in different plate geometries (thicker borders, for instance), so that not all plates will be identical. Nevertheless, when considering only the core, a single geometry pattern is necessary.

3.2 FIRST DESIGN

This section shows a design possibility of a heat exchanger that could be compared to previous ones manufactured in the Laboratory of Heat Pipes. Because of the study motivations behind this monograph, such prototype was not tested, however, its importance is recognized once it proves the applicability of the manufacturing technique.

Based on the common use of 3mm thick stainless steel plates to manufacture heat exchangers in the Laboratory of Heat Pipes, it was decided to keep this standard for the present design. Furthermore, 3mm wide channels had also been used multiple times in past experiences, yielding therefore another design parameter to be followed. To keep dimensional standards, gaps between consecutive rows of fins (plena) were also designed with a 3mm spacing.

[1] In this context, a plenum is the gap between two consecutive rows of fins. This way, whenever a fluid particle leaves a flow passage between to fins, it enters a plenum before flowing through the gap between two fins of the same row again.

[2] Fouling can also occur through many other mechanisms as well. Calcium carbonate deposition is only a common scenario.

Figure 21 – Heat exchanger core with longitudinal cut.

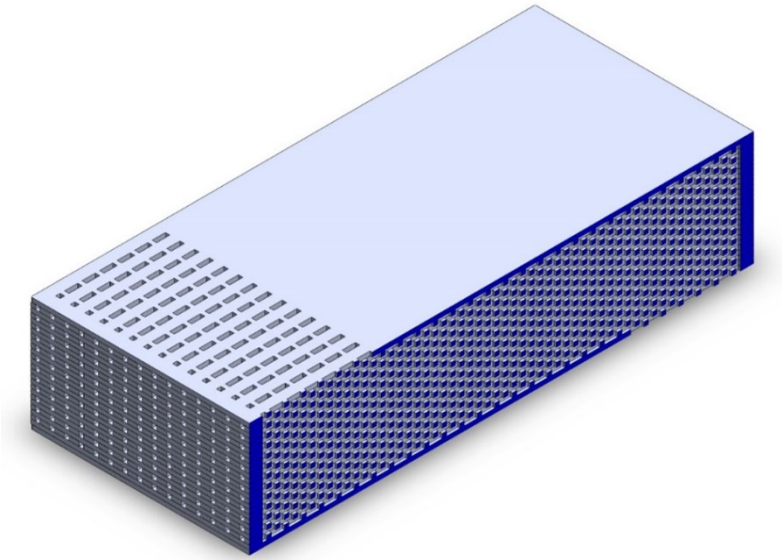

Figure 22 – Internal geometry.

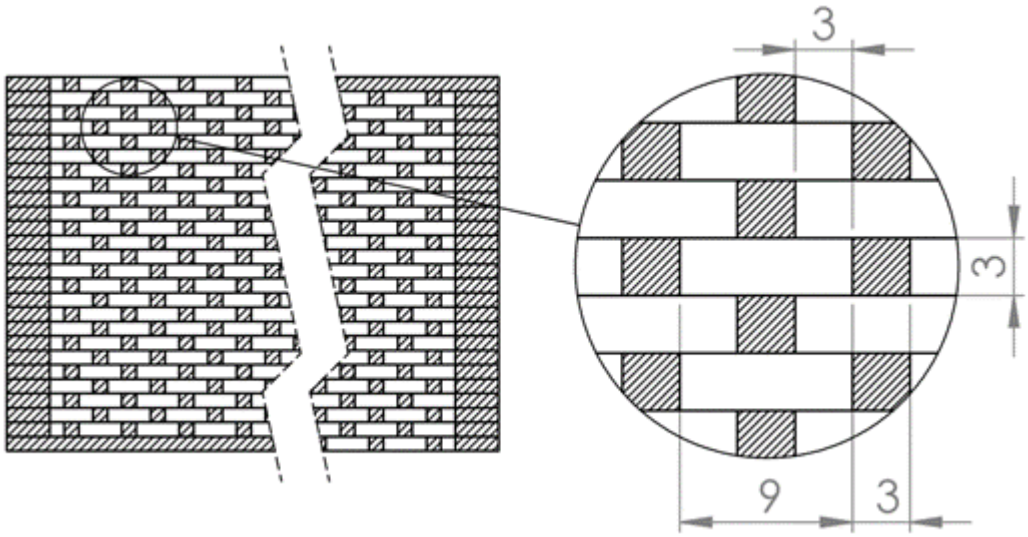

The heat exchanger's external dimensions were also based on previously manufactured models for the sake of comparison. This originated the heat exchanger core presented in figure 21, which shows the designed core longitudinally cut on the first stream layer. The internal geometry is shown in detail in figure 22, which follows an equivalent cut plane as the one in the previous figure.

The plate geometry needed to build the heat exchanger core is presented in figure 23. For the actual assembly, however, some extra features are necessary, as will be explained later. Therefore, this figure only shows what will be left of each plate inside the heat exchanger core, not how each plate should be machined in the first place.

For stacking purposes, the plates need guiding holes through which alignment pins can be inserted. Alignment is crucial for the formation of separation walls between both

Figure 23 – Heat exchanger plate.

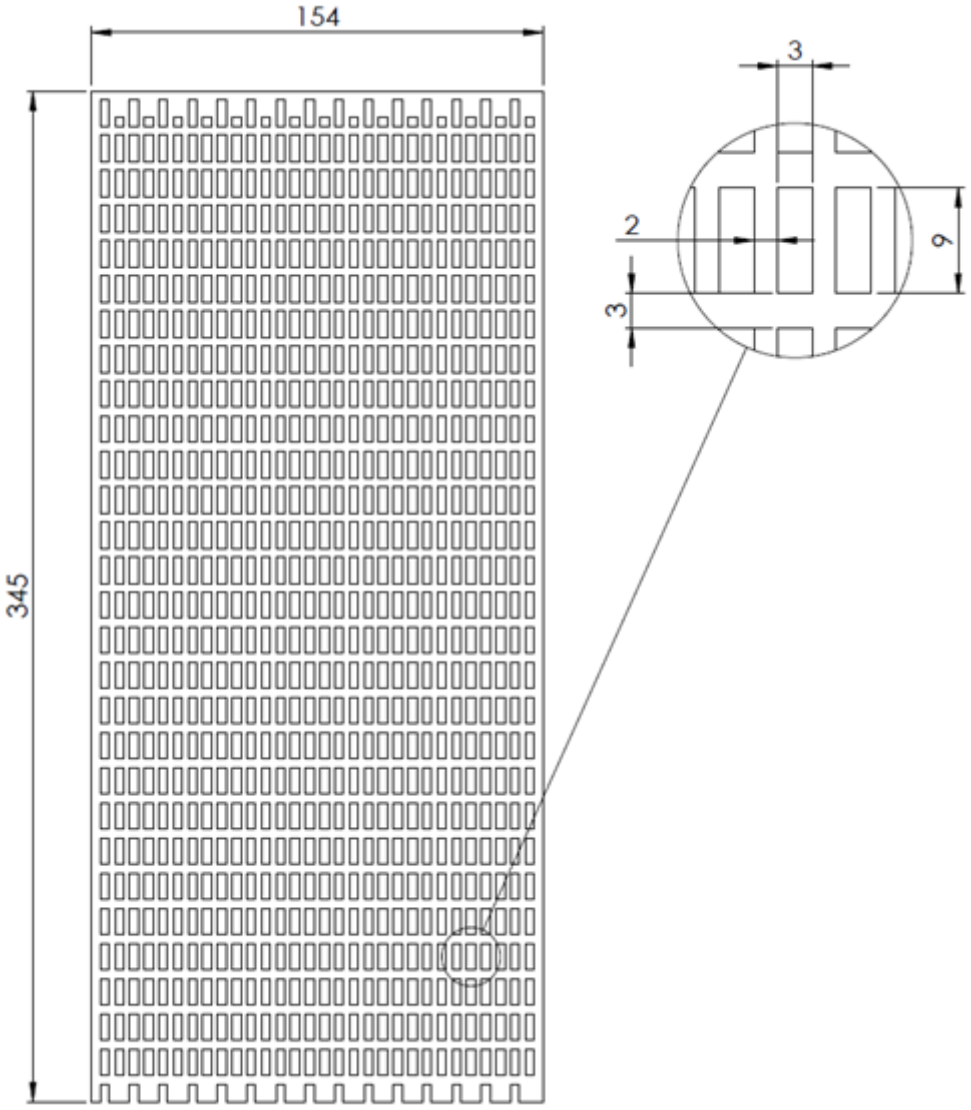

streams. Figure 24 shows added material to the upper and lower sides of the plate, where these guiding holes are located. A reference geometric feature was also added to the design to ensure correct stacking orientation of each plate.

Because of header placement, the first and last plates of the stack need a different design, which is shown in figure 25. This allows two headers to be placed for each stream. One stream longitudinally crosses the entire heat exchanger. The other would have its inlet and outlet positioned on the first and last plates of the stack. Because of the added material needed for the guiding holes and reference features, the top and bottom plates have indentations indicating where the stack must be cut after diffusion bonding. Cutting is essential to open the flow passages.

The resulting plate stack can be seen in figure 26. The added material is usually cut by electric discharge machining. A comparison between the stages before and after the cutting process is shown in figure 27. Figure 28 shows the resulting core.

Figure 24 – Plates for manufacturing.

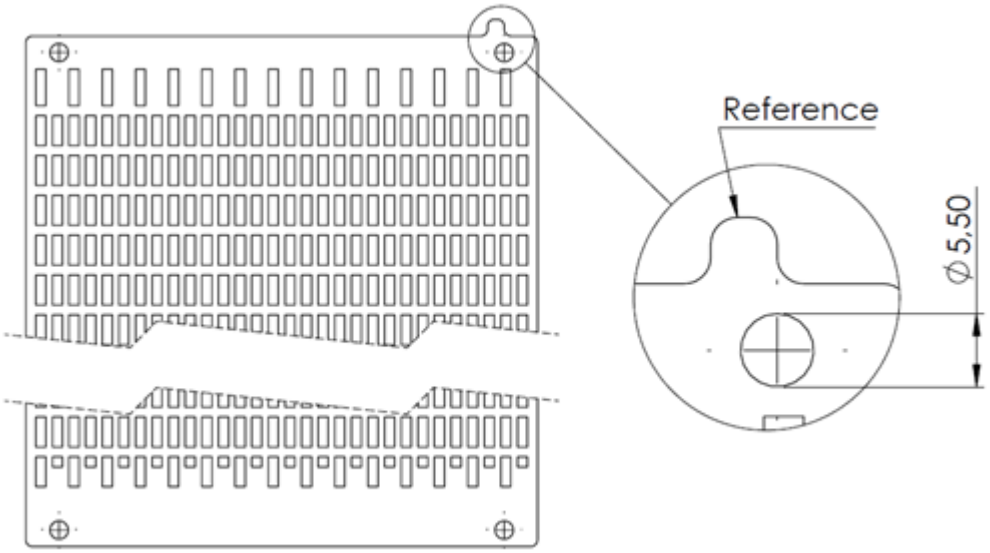

Figure 25 – First or last plate of the stack.

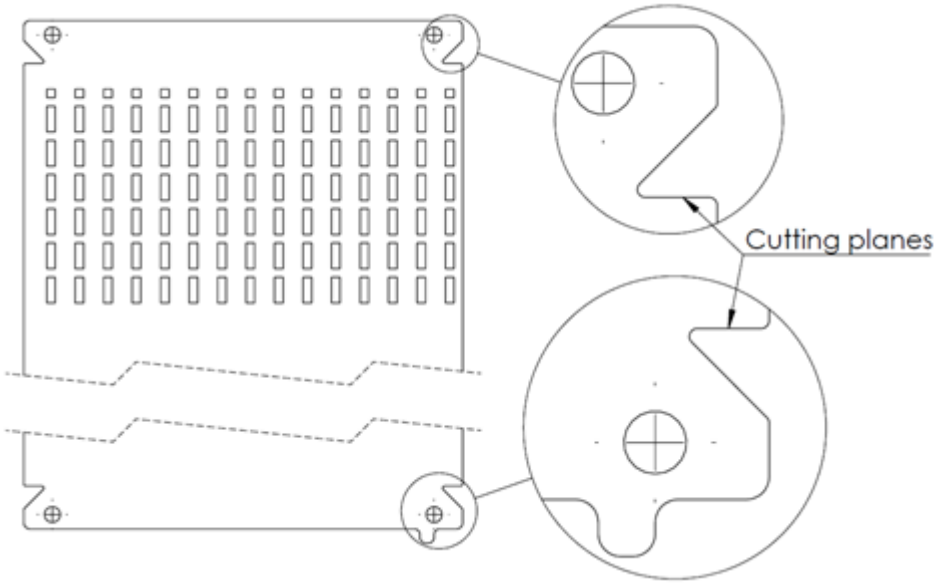

Figure 26 – Plate stack.

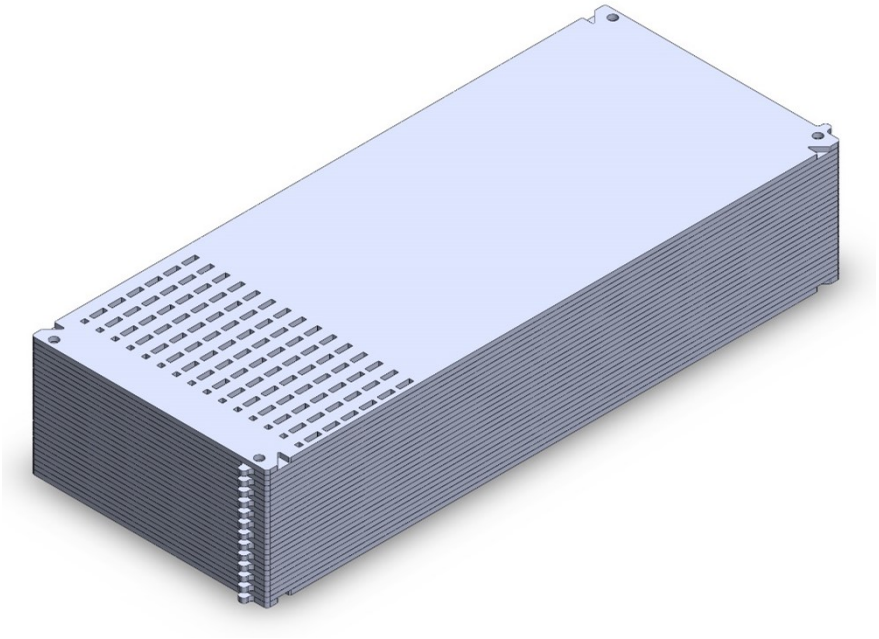

Figure 27 – Heat exchanger core (a) before electric discharge machining and (b) after electric discharge machining.

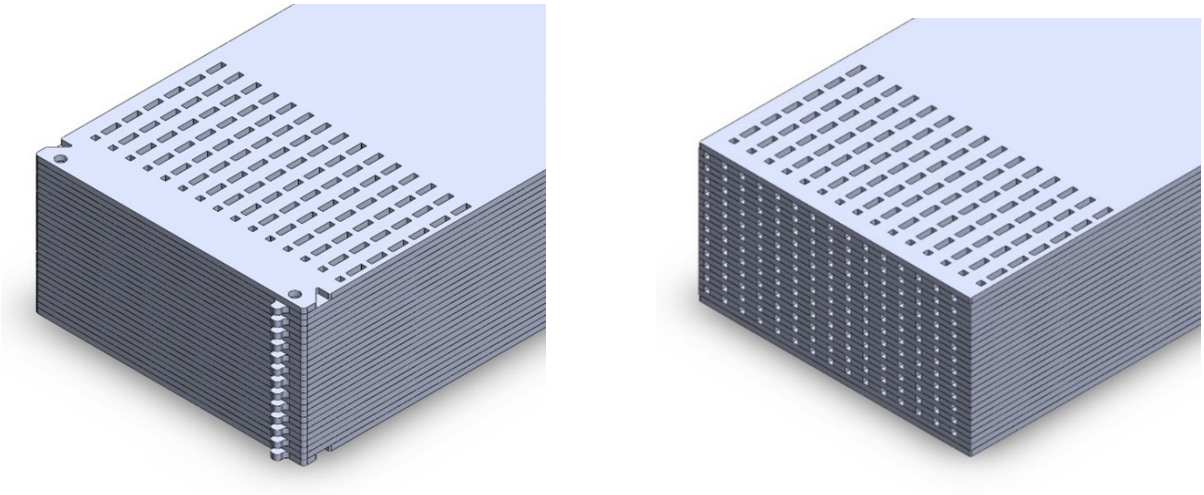

(a) (b)

Figure 28 – Heat exchanger core.

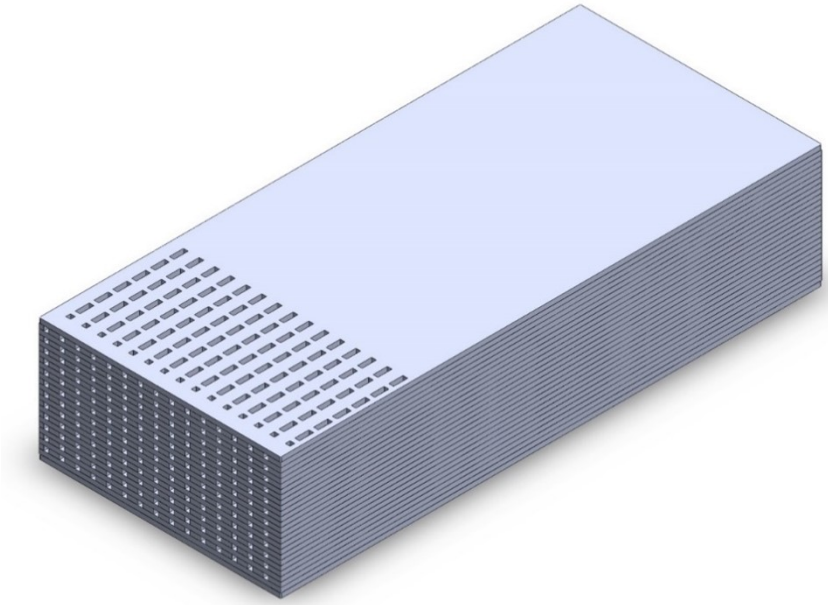

The next step consists of designing the headers. Inlet headers can be designed with flow distributors, which are not needed in outlet headers.

3.3 COMMENTS

The present design would be effective for testing the thermal and hydraulic performance of the new conception. Therefore, the heat exchanger idealized in this chapter is a valuable design for practical implementation and it illustrates the capabilities of the presented manufacturing method. However, as soon as observation of fouling is of interest, such design is no longer practical. For immediate research purposes, a different prototype, which allowed appropriate testing under both fouled and non-fouled conditions, was needed, and its design is presented in the next chapter.

4 EXPERIMENTAL SET-UP

4.1 MOTIVATION

Since interest regarding operation under fouled conditions appeared, a special prototype needed to be manufactured, which could not only provide heat exchange and pressure drop data to develop appropriate correlations, but also allow future observation of fouling. The design presented in the last chapter would not allow proper observation of the streams, so a new design was needed to enable the new geometry to be tested. The present monograph, however, focuses only on the thermal and hydraulic aspects of the new heat transfer surface.

To prepare the testing apparatus for gathering heat transfer and pressure drop data, and also for future experimental fouling studies, a new workbench was assembled. Two closed streams needed to be built, in order to test the heat exchanger in the presence of a solute. Each stream could only have a limited amount of fluid to allow practical control of solute concentration. Furthermore, peripheral equipment such as cooling towers and cryostats should not be installed directly in the circuit to avoid fouling in them. Therefore, temperature control would have to be performed by using heat exchangers connected to such devices.

4.2 PROTOTYPE

4.2.1 Design

Because of observation purposes, each stream was designed with only one layer of channels or flow passages covered with glass for visualization. One of the layers presents straight channels of square cross section. Such kind of geometry had already been studied, both by multiple authors, as well as by the laboratory team, with successful implementation of literature-based correlations. Based on these previous studies, the channels were designed with a 3mm $\times$ 3mm square cross-section.

The second stream was designed with intercommunicating channels forming a pin-fin heat transfer surface. The goal here was to create the same geometry previously presented in chapter 3. Therefore, the same standard periodic machining pattern was chosen, so that all fins were similar and spacing was constant (figure 22).

The previously idealized manufacturing process was not be applicable in this case, due to the aspect ratio of the resulting heat exchanger's core. Because of the presence of only two stream layers, the plate stack's height would be considerably greater than its width. It should be remembered that, in the proposed fabrication method, the separation walls are transversal to the stacked plates. If the proposed process were to be applied to build a thin heat exchanger such as the one here idealized, an excessively slender plate stack would be formed, which would create stability issues when loaded for diffusion

Figure 29 – (a) Plate stacking and (b) diffusion bonded core.

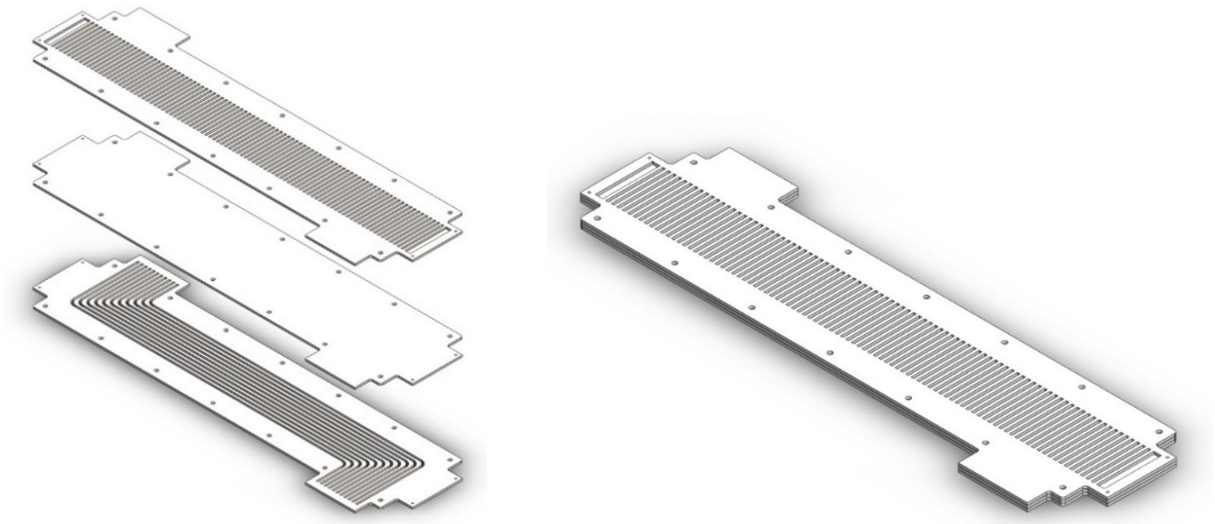

(a) (b)

bonding[1]. Instead of the previous procedure, for the present prototype, three metal plates with flat geometry were designed, fabricated and diffusion bonded.

The first plate had 3mm wide channels, with 3mm thick separation fins. In order to allow future header installation, channels were designed with an "S-shape". The second plate played the role of the separation wall (full plain pate) and was designed with the same external geometry of the first one.

To build the prototype, it would not be possible to individually place every fin at the correct position and later diffusion bond them to the core. Therefore, the third plate was designed in a way that would subsequently allow one to obtain the desired pin fin geometry through a milling process. With that in mind, the plate was manufactured with numerous transverse beams, that would, once bonded, be machined to have the flow passages opened. All three plates should then be stacked such as shown in figure 29a. The stack would then be diffusion bonded to form the core, such as represented in figure 29b. Figure 30 shows the expected heat exchanger core after the milling process, with open flow passages.

Subsequently, frames should be added to both sides of the core to enable the placement of glass sheets. The frames should be made of machined steel plates and stacked such as shown in figure 31.

The core would then be machined in the header regions to open the inlet and outlet channels. Frames were designed with special geometric features (indentations) to show where machining is needed. The result can be seen in figure 32.

The headers consist of an assembly of parts. A slot-shaped channel with a flange

[1] In order to understand this properly, imagine the conceptual core of figure 17 with only two layers of flow passages.

Figure 30 – Milled core.

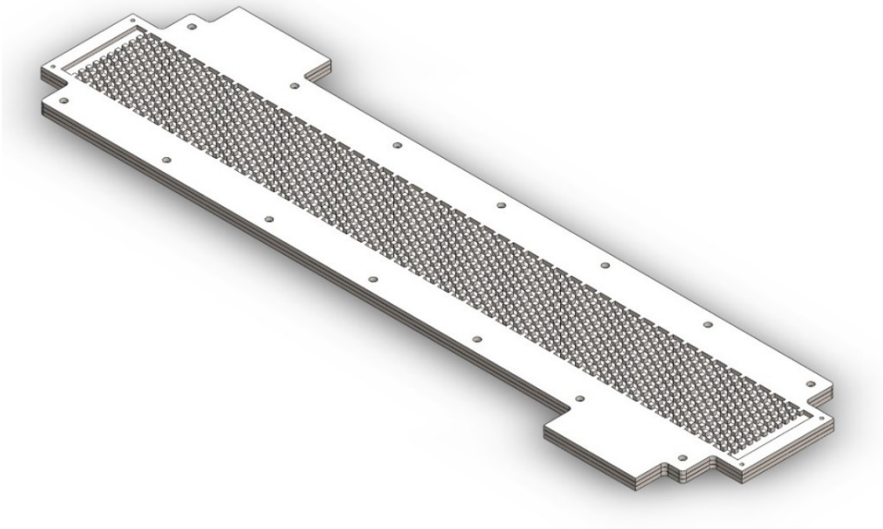

Figure 31 – (a) Plate stacking for frame placement and (b) core with frames.

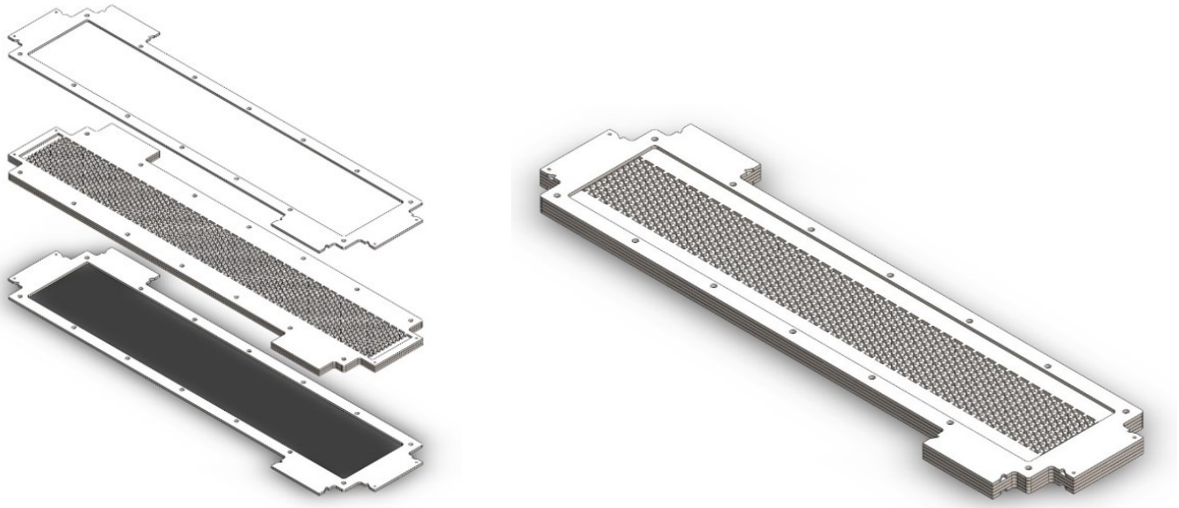

(a) (b)

Figure 32 – Prototype core.

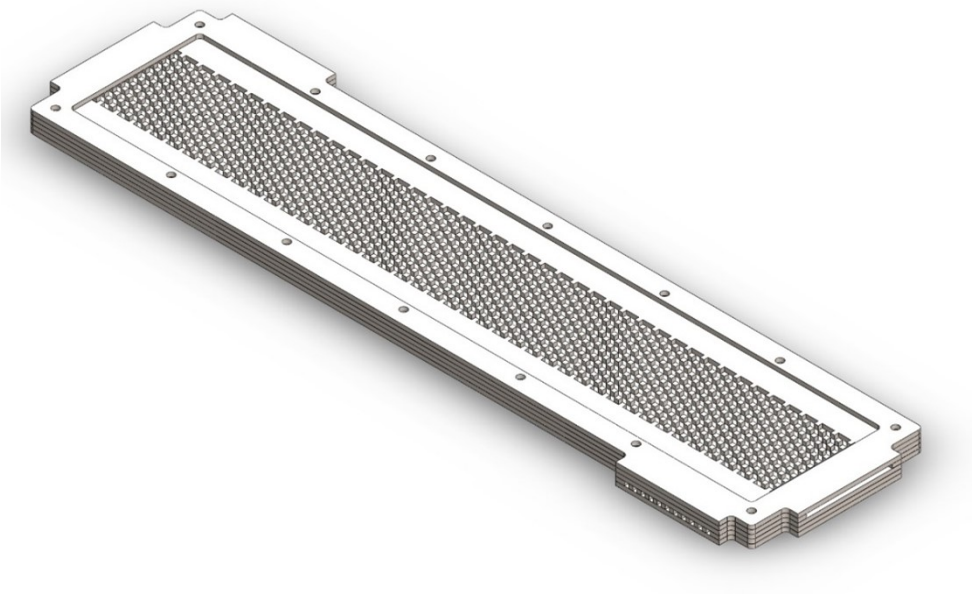

should first be welded to the core at each inlet and outlet. These channels were designed with two holes, where plugs would be inserted for pressure measurement. The plugs would then be connected to hoses, which, in turn, would be connected to differential pressure gauges.

Inlet headers were designed with internal distributors, so that mass flow could be evenly spread to all channels and flow passages. An assembled inlet header is shown in figure 33, whereas an exploded view of the entire assembly is presented in figure 34. The distributors consist of two steel plates separated by a spacer. Each plate contains two lines of 2mm-diameter holes. When assembled, the holes belonging to one plate are not aligned with the ones on the other, such as presented in figure 35. The spacer should be made of rubber for water sealing. The plate pair that forms the spacer must be connected to two flanges, one upstream and another downstream. In both cases, rubber spacers similar to the one previously presented should be implemented to obtain water tightness. The upstream flange must then be directly welded to a tapered diffusor, which, in turn, must be welded to a steel tube. The downstream flange is the one welded to the slot-shaped channel.

The outlet headers are similar to the inlet ones, although they do not have flow distributors. Therefore, the outermost flange of each outlet header can be directly mounted onto the upstream one, which, in turn, must be welded to the slot-shaped channel. A rubber layer should also be applied for water sealing. The outlet header can be seen in figure 36.

The outlet headers were designed with long outlet tubes for thermoresistance placement. This was done not only because of the thermoresistance's length, but also to develop the outlet flows for temperature measurement. The result can be seen in detail in

Figure 33 – (a) Inlet header and (b) inlet header with partial cuts.

(a) (b)

Figure 34 – Inlet header assembly.

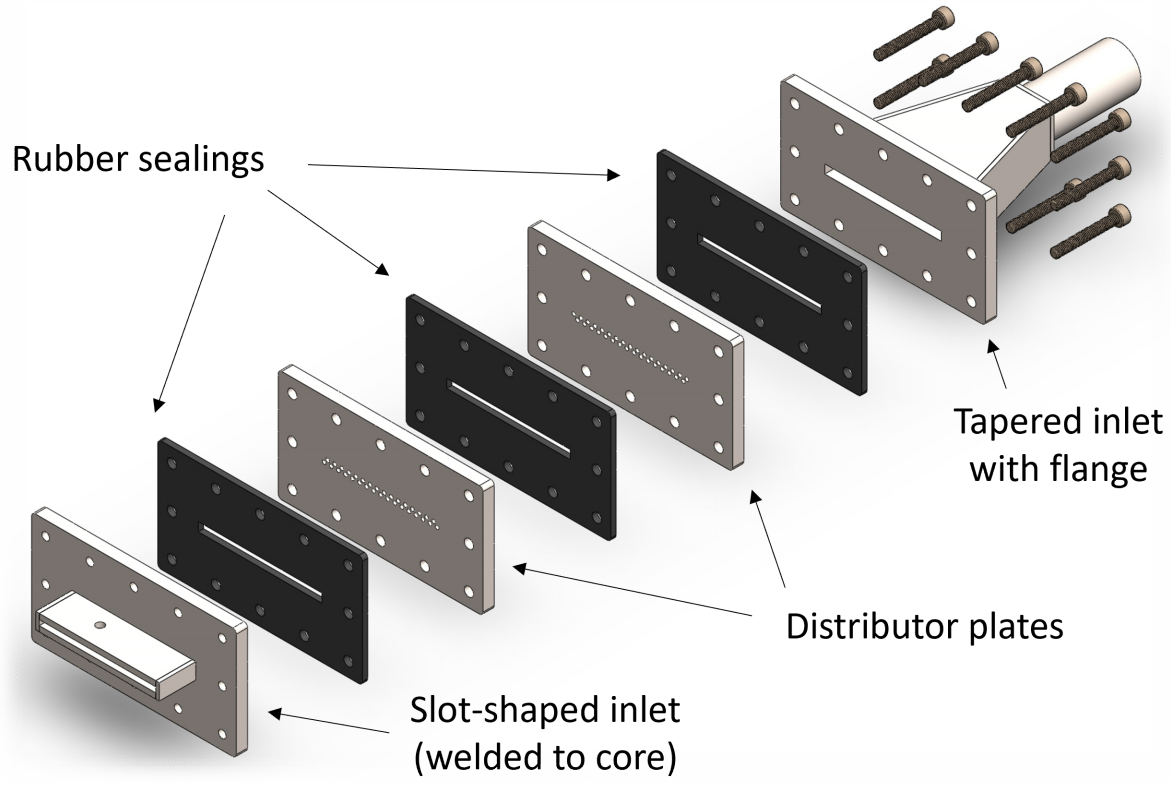

Figure 35 – Distributor flow passages.

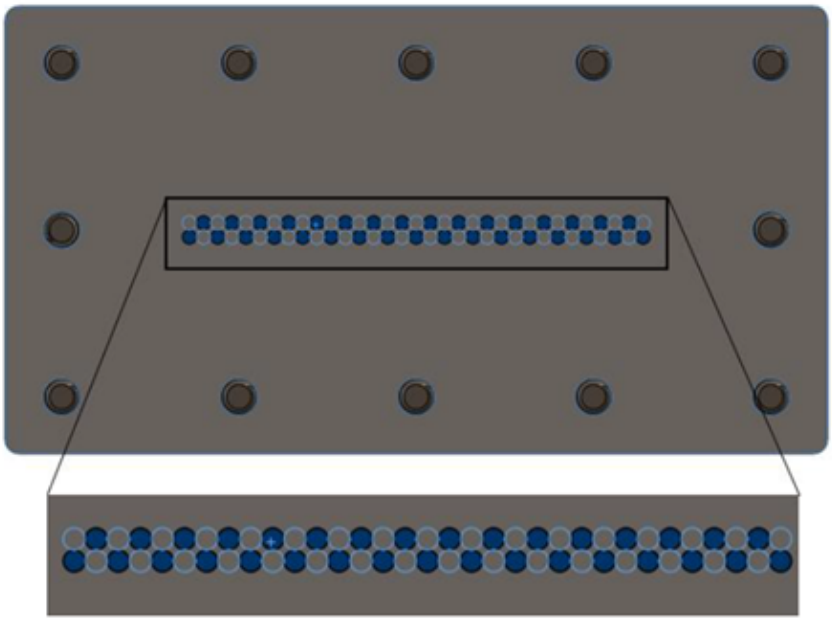

Figure 36 – (a) Outlet header and (b) outlet header with partial cuts.

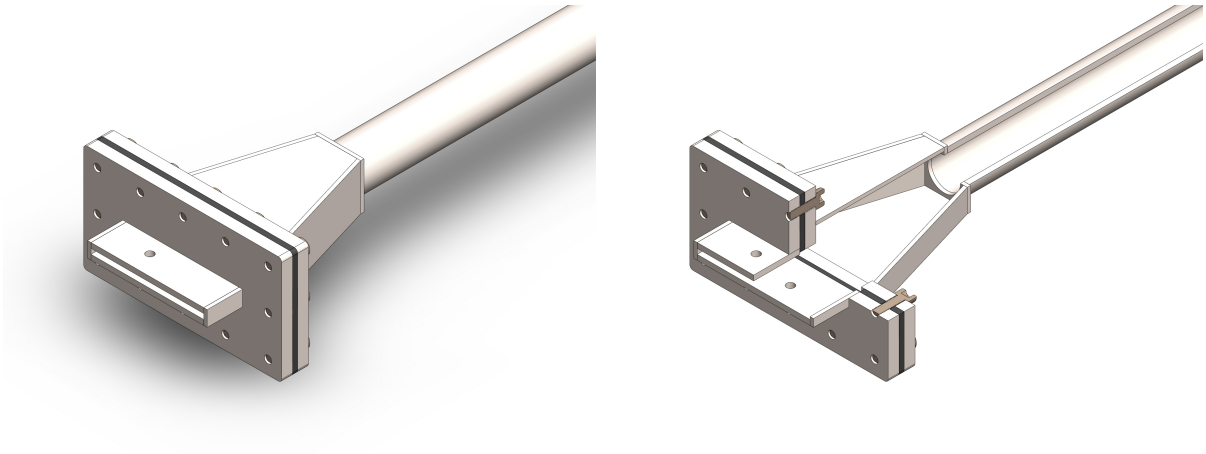

(a) (b)

figure 37, whereas the general assembly with all header is shown in figure 38.

The next step would be placing glass sheets inside the frames. Each sheet should be held in place by a rubber layer under an external steel frame. The assembly would be tightened by bolts. Both the rubber layers and the external frames were designed to cover the gap between the glass sheets and the internal frames. The final result can be seen in figure 40. The assembly procedure is illustrated in figure 39.

Figure 37 – Header placement in detail.

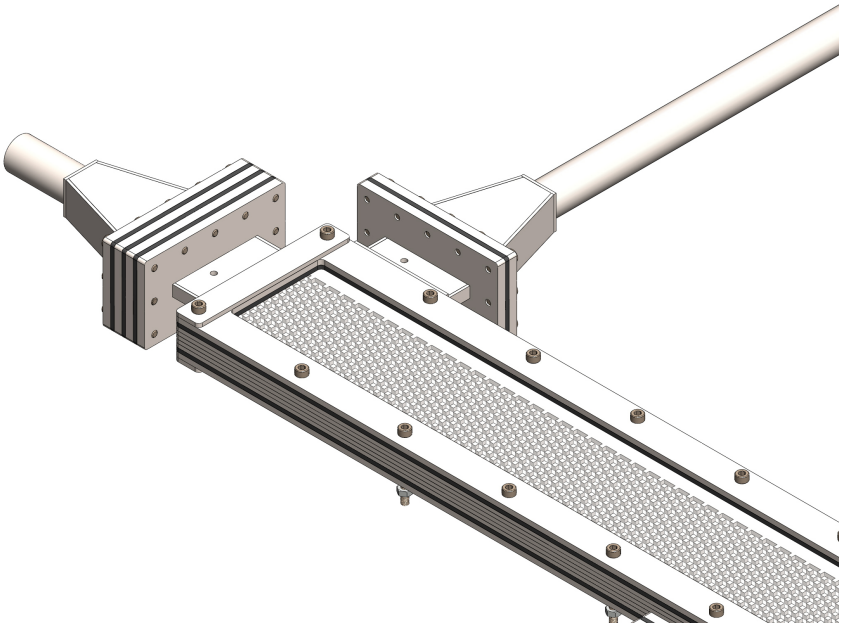

Figure 38 – Core with headers.

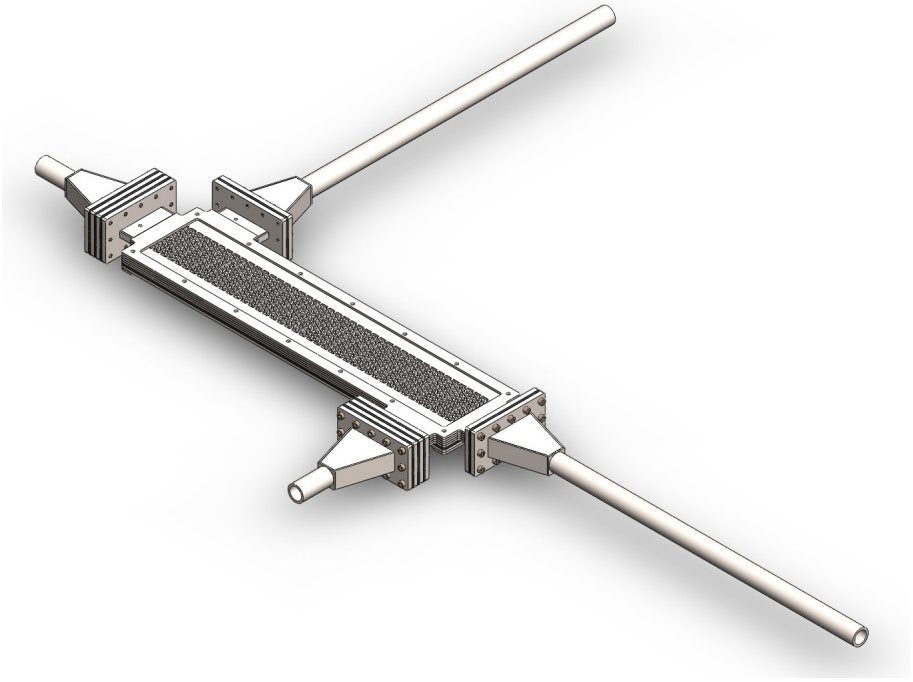

Figure 39 – Assembly procedure.

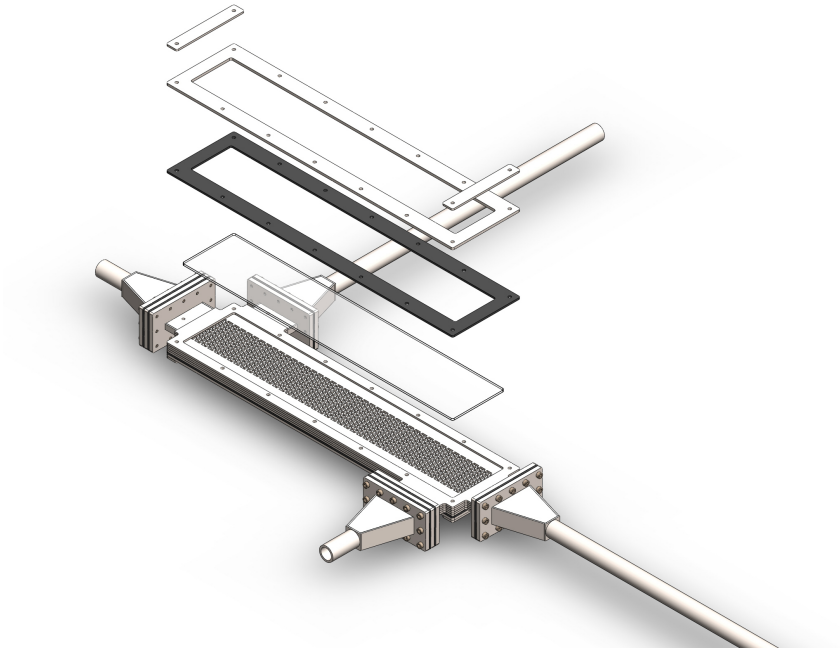

Figure 40 – Assembled heat exchanger.

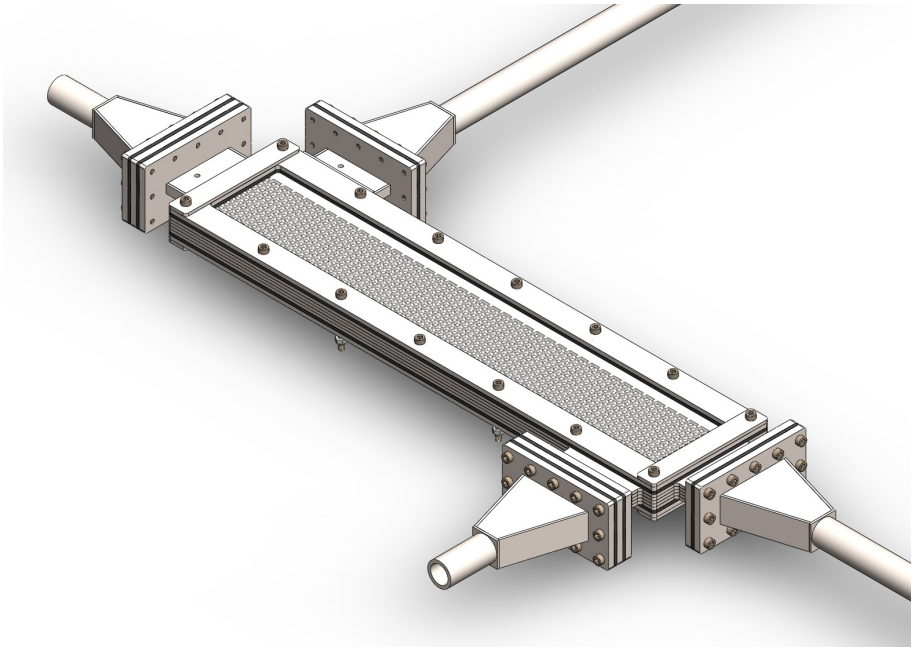

4.2.2 Manufacturing

The AISI 316L stainless steel plates were machined by a waterjet cutter. The plates were afterwards sanded, primarily washed with plain detergent and then subsequently washed in two ultrasonic baths. The plates were then stacked. To guarantee appropriate assembly, alignment pins were used.

To avoid any damage caused by the alignment pins to the oven's press surfaces, two extra plates were added on each side of the stack. The extra layers would enable the alignment pins to eventually move during accommodation without touching the press' surfaces. These plates were also properly washed, such as the core ones. Figure 41 shows the plate stack ready for diffusion bonding inside the oven. The result of the diffusion bonding process can be seen in figures 42 and 43.

The core was then milled in a CNC machine to form the flow passages (and separate the pin fins from one another). Figure 44 shows the milling pattern that was followed throughout the entire core. The result can be seen in figure 45.

The frames were glued to the core using silicone. During the procedure, attention was given not to put any silicone near the header regions. The frames were cut with geometric features indicating where channel openings were needed. As soon as the silicone dried out, the core was cut by electrical discharge machining to open stream inlets and outlets. During these last two steps, the frames were also kept in place by bolts.

The slot-shaped channels were then welded to the core, enabling all headers to be mounted. Apart from the tubes, the headers were also manufactured by machining steel plates and subsequently welding the parts. Just as the core, all parts were manufactured

Figure 41 – Plate stack inside the oven.

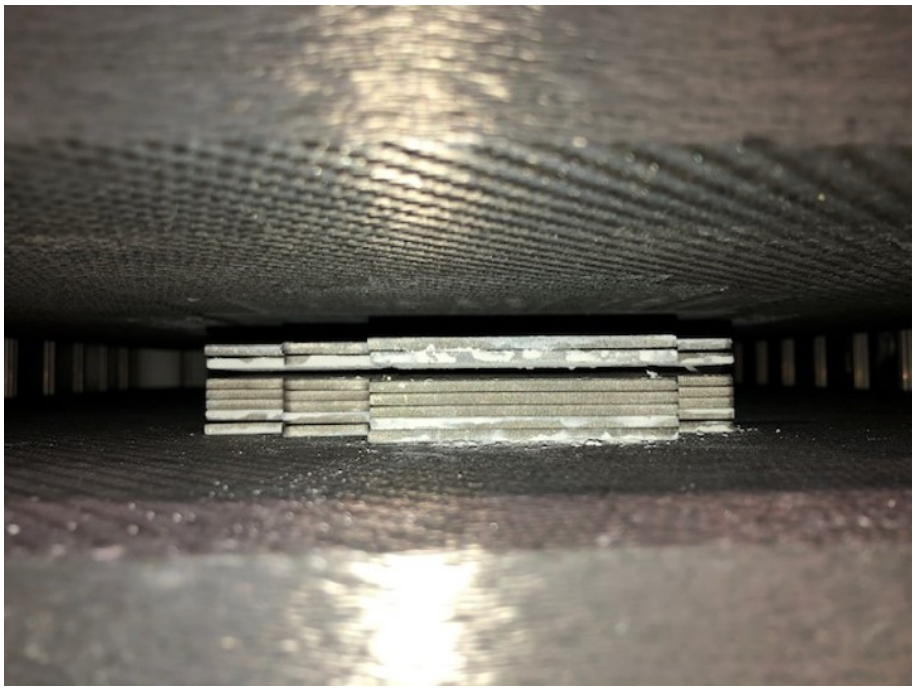

Figure 42 – Bonded core - pin-fin side.

Figure 43 – Heat exchanger core showing side with channels of square cross-section.

using a waterjet cutter. Figure 46 shows some header parts.

The manufactured geometries of both streams differ from their design idealizations because of three causes. One of them is related to the waterjet cutter's precision. Because of geometric deviations during cutting, channels were machined with a larger width than designed, meaning that the straight channels are wider, whereas their fins are thinner. Likewise, all the plena between consecutive layers of channels/fins in the pin-fin stream are also wider.

Another issue concerning manufacturing precision is the original thickness of the steel plates. Moreover, plastic deformation is imposed onto the plates during the diffusion bonding process. Because of these reasons, the resulting diffusion bonded core has a smaller height compared to the design value.

To determine the influence of the manufacturing processes on the core's dimensions, pictures of the cold stream were taken. Based on any known length between two points in the picture, the scale could be found and any other dimension could be determined. In total, 10 pictures were used. The scale was determined based on the assumption that the CNC milling machine produced spacing pitches accurately enough for the measurement purposes. Hence, consecutive fins of a row are considered to be uniformly spaced according

Figure 44 – (a) Heat exchanger core in milling machine and (b) initial milling of flow passages.

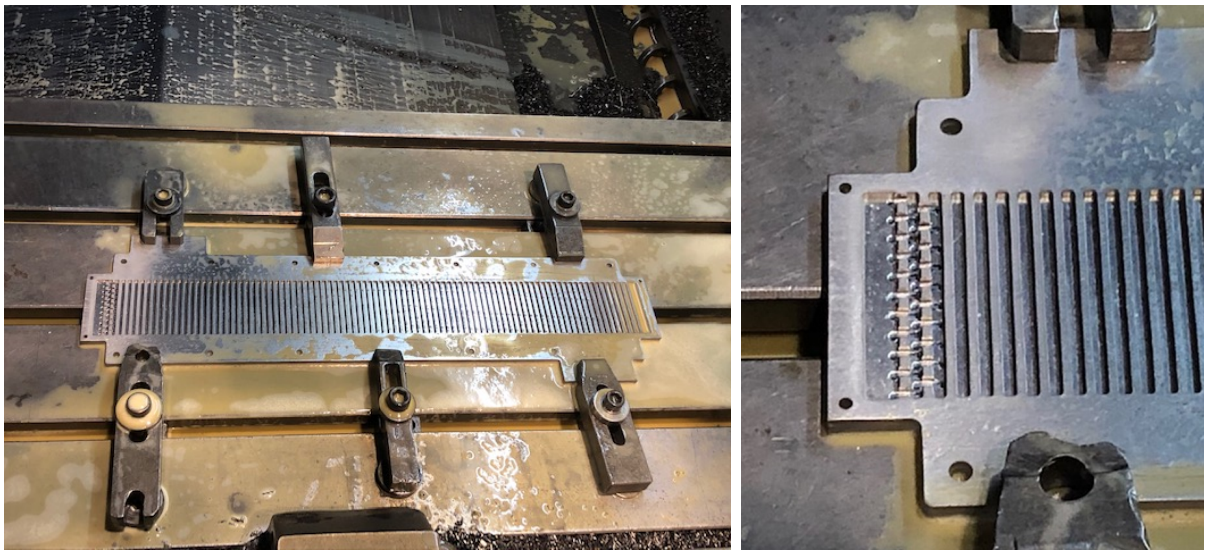

(a) (b)

Figure 45 – Milled core.

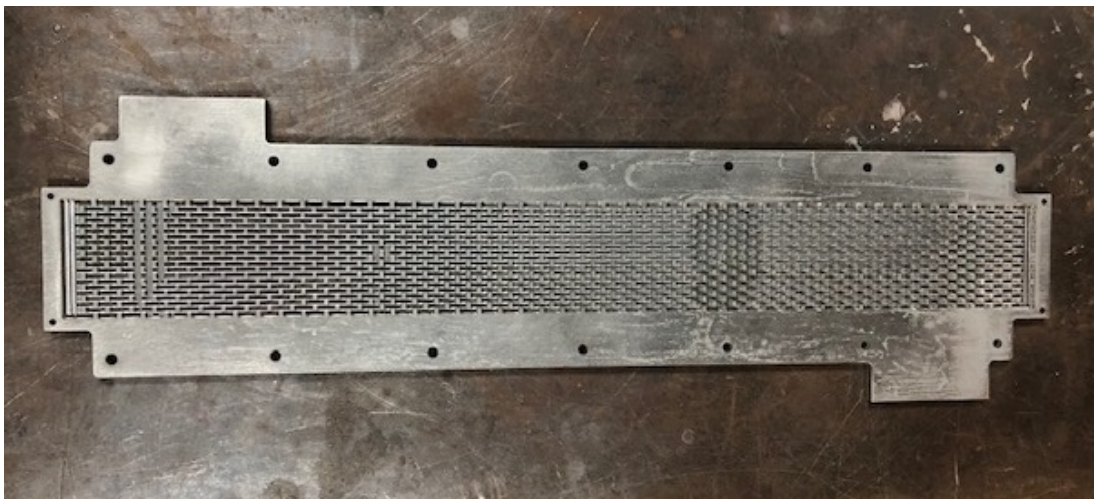

to design dimensions. Instead of considering only two consecutive fins, multiple fins were used when determining the reference length for scale setting. Caution was taken when selecting the points for scale setting. Faces with the same relative positions to their respective fins were selected. This means that if, for instance, when looking at a picture, the right-hand side of a fin was selected, the right-hand side of another fin in the same row was also selected. Therefore, the distance would only be a function of spacing pitch, and not the tool's diameter[2].

The software was calibrated for every picture used in the study. Each picture provided 5 measurements. The statistical distribution of measurements provided the random

[2] The milling process consisted of passing a 3mm tool multiple times across each flow passage until the entire depth was cut. Therefore, the passage width corresponds to the tool's diameter.

Figure 46 – Header parts.

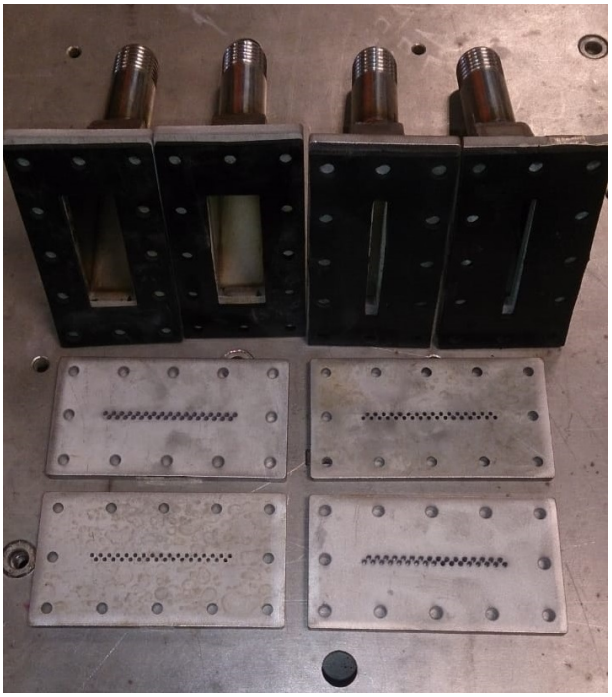

Table 10 – Spacing between consecutive rows of fins.

Mean Value [mm]	4,0096
Sample Standard Deviation [mm]	0,0786
Number of Data Points	50
Approximate Resolution [mm]	0,02
Standard Uncertainty [mm]	0,0788
Expanded Uncertainty [mm]	0,16
Result of Measurement	$(4,01 \pm 0,16)$mm

uncertainty. As a second source of uncertainty, the picture resolution was considered.

A set of measurements taken from one of the pictures is shown in figure 47. The first goal of this analysis was to determine the spacing between consecutive rows of fins (plenum width) as a measurand subjected to both systematic and random effects. The second goal was to determine the systematic influence of the waterjet cutter. This analysis was done only for the cold stream because, by the time the pictures were taken, the heat exchanger was assembled for testing in a way that made the other stream inaccessible to be photographed. Since both plates were consecutively machined in a single cycle, the same systematic effects are expected to be present in both plates. Therefore, the results from this analysis will be used for both streams. Relevant statistical data related to measurement results are presented in table 10. It is important to notice that the spacing is a variable measurand.

Figure 47 – Sample picture used for measurements.

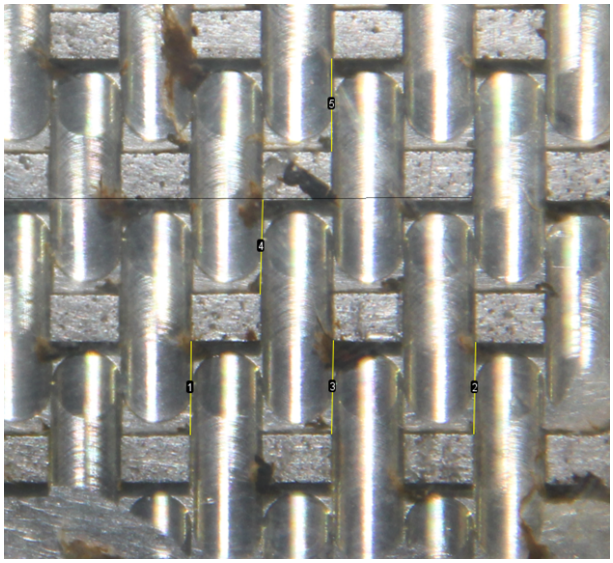

Table 11 – Mean value of spacing between consecutive rows of fins.

Mean Value [mm]	4,0096
Sample Standard Deviation [mm]	0,0786
Number of Data Points	50
Standard Deviation of Mean Value [mm]	0,011
Approximate Resolution [mm]	0,02
Standard Uncertainty [mm]	0,0125
Expanded Uncertainty [mm]	0,025
Result of Measurement	$(4,010 \pm 0,025)$mm

The systematic influence of the waterjet cutter is represented by the mean deviation between the obtained measurements and the theoretical value. Therefore, its determination involves knowing the mean value of plenum width, which can be obtained with higher accuracy than simply the plenum width itself, given that the latter is a variable measurand. Results are shown in table 11. Since the design value of plenum width is 3mm, the waterjet cutter systematically produced channels $(1,010 \pm 0,025)$mm wider than designed.

A caliper was used to measure the core thickness five times. Results from the measurements of the thickness of the three plate core are presented in table 12.

Details about the metrological procedure are given in appendix B.

Table 12 – Core thickness.

Mean Value [mm]	8,46
Sample Standard Deviation [mm]	0,1949
Number of Data Points	5
Resolution [mm]	0,05
Standard Uncertainty [mm]	0,088
Expanded Uncertainty [mm]	0,25
Result of Measurement	$(8,46 \pm 0,25)$mm

4.3 WORKBENCH

A general overview of the new workbench is presented in figure 48. Both main circuits are described in detail and presented in separate pictures in the next pages. The cooling tower shown in figure 48 is located outside the building.

A general overview of the cold stream is presented in figure 49 with numbered components described in table 13. The cold stream has a water tank (1) open to the atmosphere. This allows water to expand/contract due to temperature variations. The water tank allows a solute to be added to the water to observe fouling inside the heat exchanger. An outlet pipe is located near the tank's bottom to allow water to flow from the tank to a centrifugal pump (2), which is connected to a control panel. After water leaves the pump, it flows through a polymeric hose to an electromagnetic flow meter (3), which measures the mean fluid velocity inside a pipe of known diameter, enabling the calculation of the resulting volumetric flow rate. Near the flow meter's inlet, a thermocouple is placed to measure the water temperature as it flows through the measuring device. This is needed to calculate water density and the resulting mass flow.

After leaving the electromagnetic flow meter, water flows through a cross-flow heat exchanger (4) connected to a cryostat. This allows the cold stream temperature to drop according to the cryostat's adjustment. The water then flows through the test section (5), where its temperature rises. Once the water leaves the test section, it flows through a counterflow heat exchanger (6) connected to an externally located cooling tower, before re-entering the tank.

Two reasons justify the existence of two separate cooling stages. The first one is related to the available equipment in the laboratory. There was no cryostat that could absorb the entire thermal load delivered to the cold stream by the heat exchanger prototype, for the desired operating conditions. An alternative would be to cool it down using only the cooling tower. Cooling towers work with evaporative heat transfer to the atmosphere outside the building, meaning its performance depends on weather conditions. Therefore, water from the cooling tower would not have a constant temperature, as weather conditions

Figure 48 – General overview of the workbench.

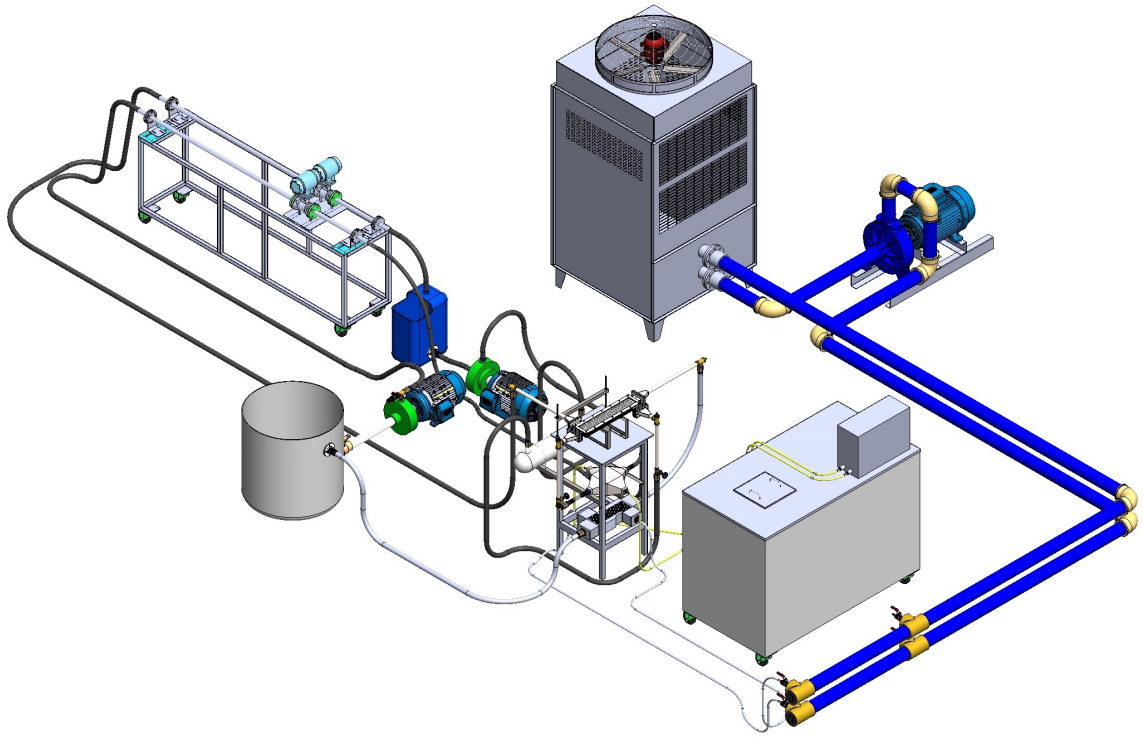

would vary throughout the day and from one day to another. Moreover, other equipment in the laboratory also depended on the cooling tower, which would increase even more temperature variations as the total demand would vary. Beyond the lack of constancy, water from the cooling tower would be close to room temperature, so the cold stream inlet temperature would not only be too unstable, but also too high for most tests, specially under fouling conditions, given the behavior of diluted calcium carbonate. The solution was then to use both systems. The cooling tower would absorb most of the thermal load, while the cryostat would only be responsible for the final temperature drop, also allowing a finer temperature control if desired.

The other reason behind the two stage cooling is related to the avoidance of excessive fouling in the peripheral equipment. Since one of the main substances related to fouling is calcium carbonate, it was highly likely that future tests would involve adding this substance to the water. Calcium carbonate has inverse solubility, meaning its solubility diminishes as temperature rises. Therefore, one would have to apply this solute to the cold stream water, allowing the deposition to gradually increase along the heat exchanger, as flow temperature rises. Since the counterflow heat exchanger was located directly downstream of the prototype, water was directly cooled down once it left prototype, increasing the solubility of calcium carbonate and thus avoiding fouling further downstream.

Figure 49 – Cold water circuit, first perspective.

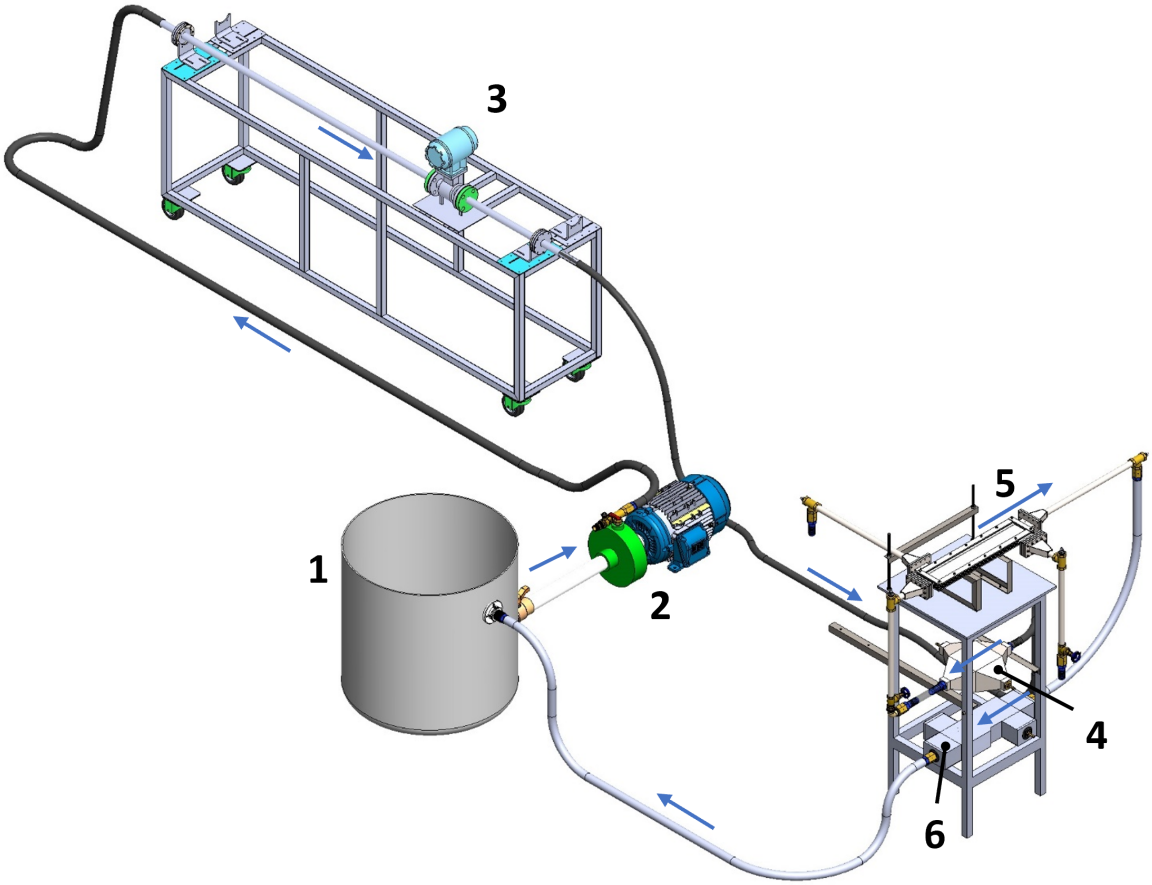

Table 13 – Components of cold water circuit as shown in figure 49.

Number	Component
1	Water tank
2	Centrifugal pump
3	Electromagnetic flow meter
4	Crossflow heat exchanger (secondary cooling stage)
5	Test section
6	Countercurrent heat exchanger (primary cooling stage)

Figure 50 – Hot water circuit.

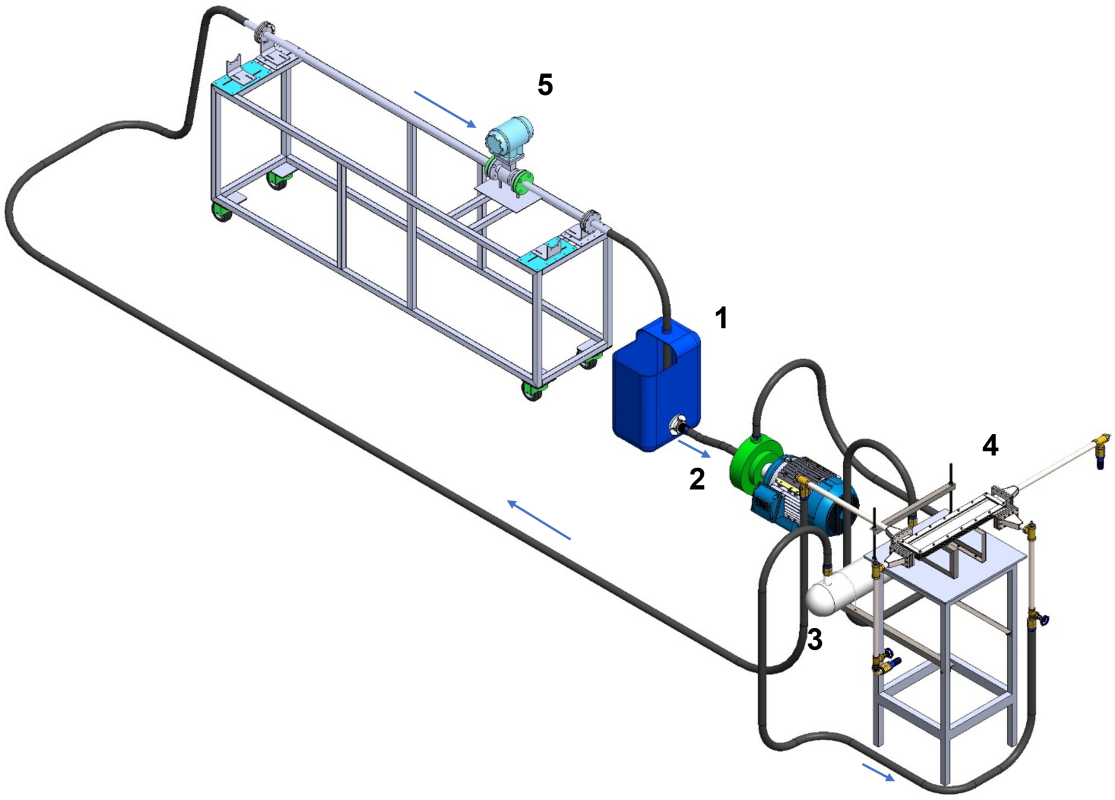

Table 14 – Components of hot water circuit as shown in figure 50.

Number	Component
1	Water tank
2	Centrifugal pump
3	Electric heater
4	Test section
5	Electromagnetic flow meter

The hot water circuit is shown in figure 50, and its components are numbered from 1 to 5 and described in table 14. This circuit also has a tank (1) open to the atmosphere. As soon as water leaves the tank through an outlet near the bottom, it flows through a centrifugal pump (2). An electric water heater (3) is located downstream. The heater was custom built for the workbench and possesses two 5kW electric resistances, which are connected to an electric tension regulator controlled by the operator. Once water is heated up, it flows directly to the prototype (4), where it cools down. Further downstream, an electromagnetic flow meter (5) is located. Likewise, a thermocouple is present to measure the flow temperature at the flow meter's inlet. The water then returns to the tank.

The three heat exchangers were mounted on a support, at three different levels

Figure 51 – Heat exchanger placement.

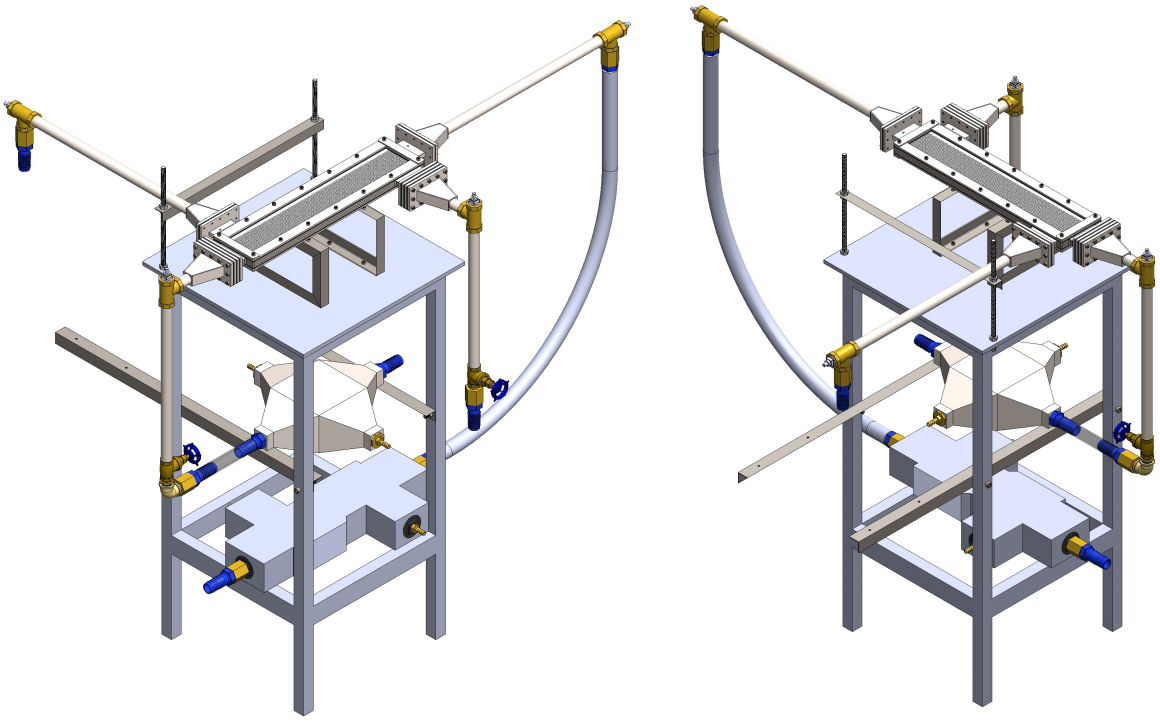

(a) (b)

Figure 52 – Test section.

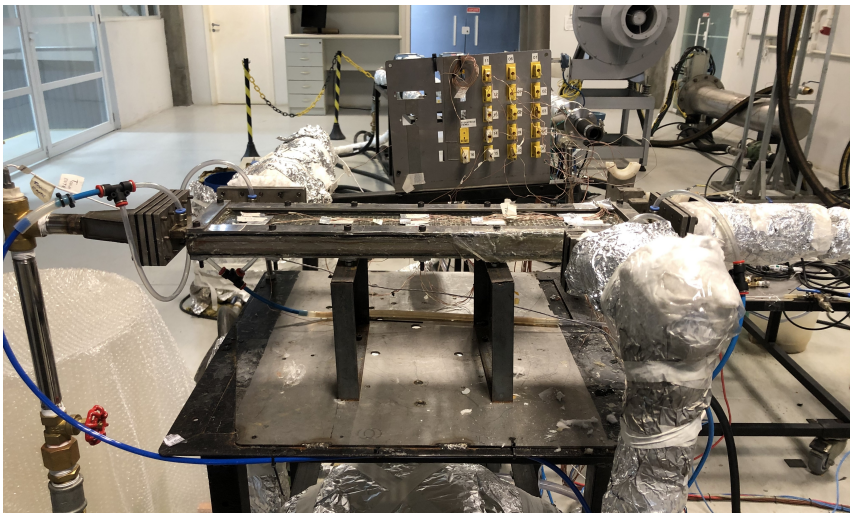

(figure 51). The bottom level contains the counterflow heat exchanger, which is connected to the cooling tower. The crossflow heat exchanger was placed above the former one, on top of two beams that also acted as a support for the electric heater (which is not shown in the figure). Finally, the prototype was positioned above all others, on top of two frames bolted to the structure's surface, forming the test section. Figure 52 shows the assembled test section (additional thermal insulation was added for testing).

Figure 53 – Electric heater.

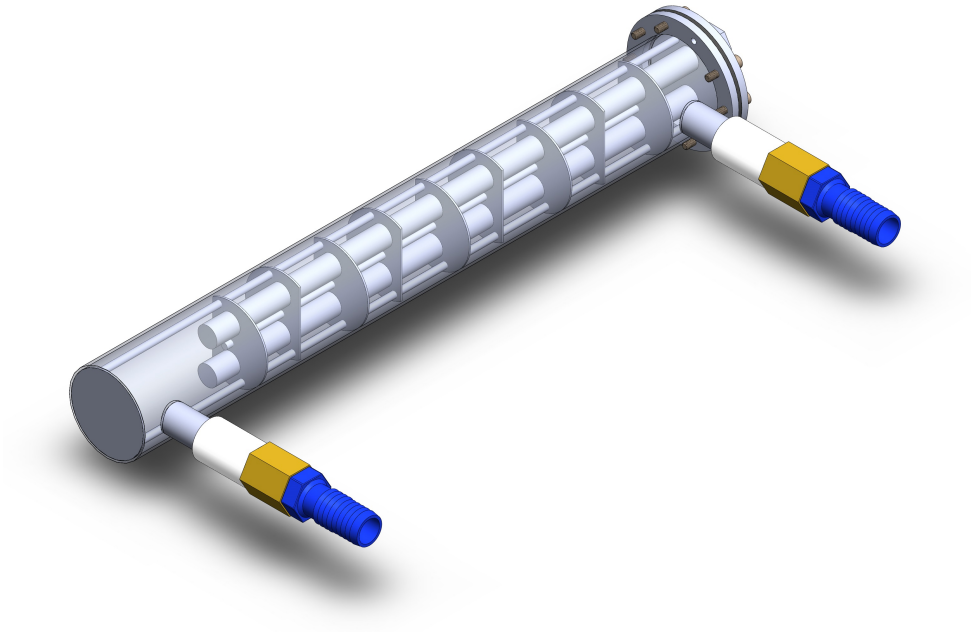

Figure 54 – Internal assembly of the electric water heater.

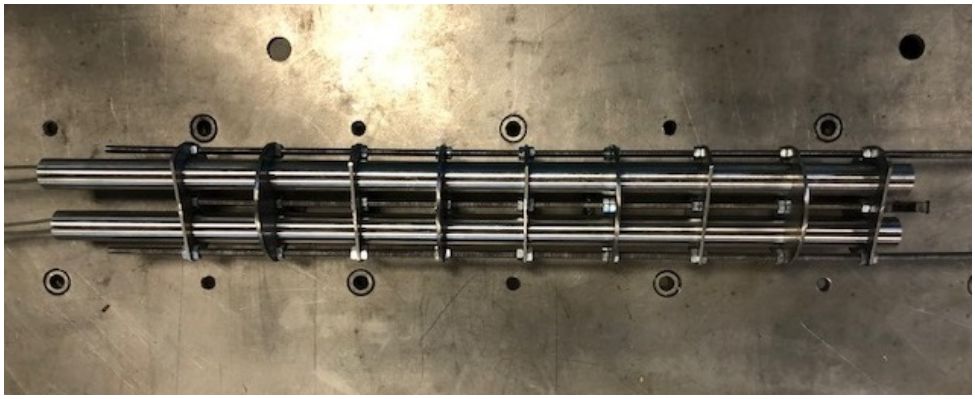

The electric heater consists of a hull built from a stainless steel tube. This is shown in figure 53. Inside the hull, two electric resistances with maximum power of 5kW were placed. Baffles were positioned inside the hull to support the electric resistances and enhance convection. A picture of the internal assembly can be seen in figure 54. The hull has a welded wall on one side and a flange on the other.

The flange enabled an external plate to be mounted with bolts. Between the flange and the plate, a rubber layer was added to prevent water leakage. The plate was fabricated with two holes through which the electric resistances were inserted. Tightening devices were welded to the plate to hold the resistances in place and prevent leakage.

Such assembly allowed the resistances' electrical contacts to be externally insulated. The insulation consists of a polymeric tube housing the electrical contacts. The tube was mounted directly over the heater's external plate. On the other side of the tube, a polymeric cover was placed. The cover had an access for electrical wiring that would later

connect the resistances to the electric tension regulator.

The hull's inlet and outlet holes were created using a hole saw. Tubes were then externally welded and appropriate fittings were added to connect the heater to the external hoses.

The workbench monitored both stream's volumetric flows and pressure drops at the test section. Volumetric flows were measured by two *Rosemount-8732* electromagnetic flow meters. Pressure drops were measured by two differential pressure sensors manufactured by Omega. Temperature was monitored in multiple locations. The most important measurements were performed by PT-100 P-M-1/3-1/8-6-1/8-T-3 thermoresistances. Thermocouples were also present at various spots. As previously mentioned, two of them were placed near the electromagnetic flow meters. Most of the other ones were positioned directly on the heat exchanger's external surfaces and were only used for quick inspections of temperature distribution, but played no role in data analysis.

All measuring devices were connected to a *National Instruments cDAQ-9178* chassis, which was, in turn, connected to a computer, where signal readings were saved in text files. This was performed by a *LabVIEW* program, which also allowed data to be monitored during workbench adjustment and testing.

The employed thermoresistances have maximum uncertainty values corresponding to one third of the uncertainties of Class B equipment, according to DIN 60751:2009-05. The norm states that Class B measurement devices have a linearly increasing maximum measurement uncertainty, for temperatures greater or equal to 0°C. More specifically, at 0°C the maximum uncertainty is $\pm 0,30$°C, whereas at 100°C the maximum uncertainty is $\pm 0,80$°C. Values between these points can be obtained via linear interpolation. The employed thermoresistances, therefore, will present uncertainties corresponding to one third of the above mentioned values.

All thermoresistances were installed in such a way that their tip was further upstream than their base. Furthermore, the piping was built so that the water flow could develop until meeting the thermoresistance.

Pressure drops were measured by differential pressure transducers manufactured by *Omega*, model *PX409*. These sensors provide an output signal in form of an electric current, which is a function of the pressure difference between the sensor's terminals. Because of the different geometries, each stream would be subjected to a different pressure drop, even if at similar Reynolds numbers. A quick test using polymeric hoses was performed to estimate the maximum pressure drop on each stream under achievable testing conditions. Based on the results, two differential transducers were selected among the available ones. For the hot stream, a sensor with maximum allowed pressure difference of 6psi was selected, whereas for the cold stream, a 50psi unit was chosen. Calibration data were provided by the manufacturer for one sensor and by a third-party laboratory for the other.

Each terminal of each sensor was connected to a hose, which was, in turn, connected

Figure 55 – (a) Pressure intakes and (b) pressure transducer with valves.

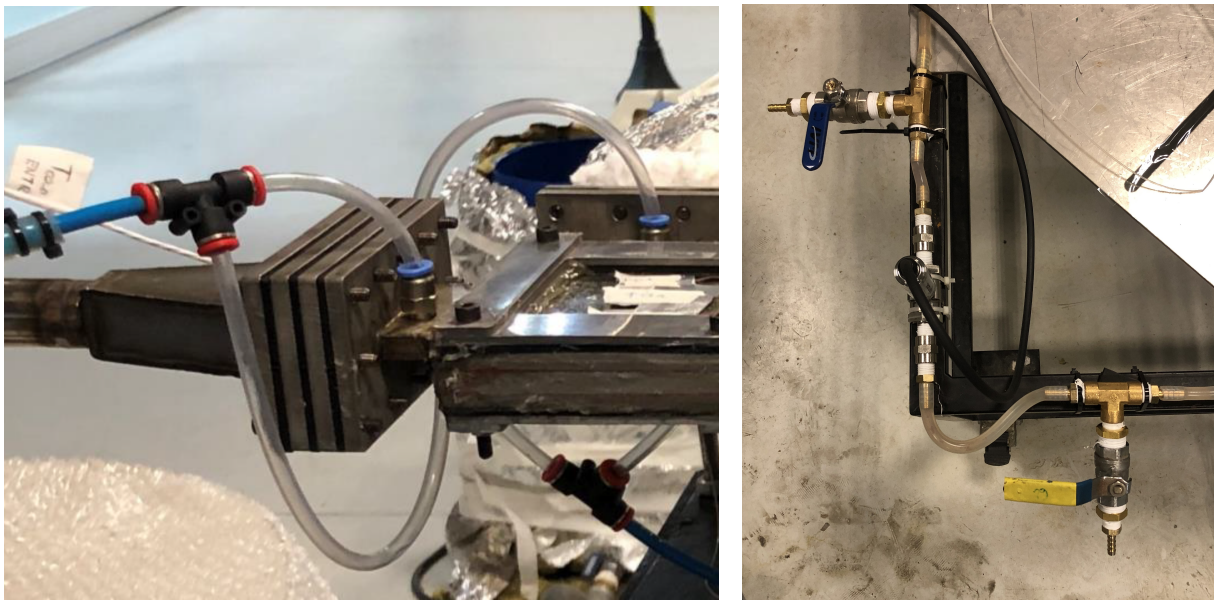

(a) (b)

to a pair of intakes, such as shown in figure 55a. Each pair of intakes was installed at a specific water inlet or outlet of the heat exchanger. Further details regarding the pressure intakes are given in section 4.2. Near each terminal, a valve was installed, which could be opened to the atmosphere. Every time the water pumps were started up, the valves were opened to allow imprisoned air to leave the system. This would avoid any deviations in pressure readings due to hydrostatic effects. Both assemblies, each one consisting of a pressure transducer and two valves, were installed on a horizontal surface. One of the assemblies can be seen in figure 55b.

After complete assembly of the workbench, thermal insulation was added to the prototype and other necessary spots. Glass wool was added not only to the prototype's core, but also to the inlet and outlet tubes, where the thermoresistances were placed. The insulated test section can be seen in figure 56. The cross-flow auxiliary heat exchanger was also insulated, and so were parts of the piping, such as the metallic inlet and outlet tubes of the hot circuit's electromagnetic flow meter. The hot water tank was also thermally insulated. Both tanks were filled with deionized water to avoid fouling, and then covered with plastic sheets to avoid contamination. Eventual leakages were detected and repaired.

Figure 56 – Insulated test section.

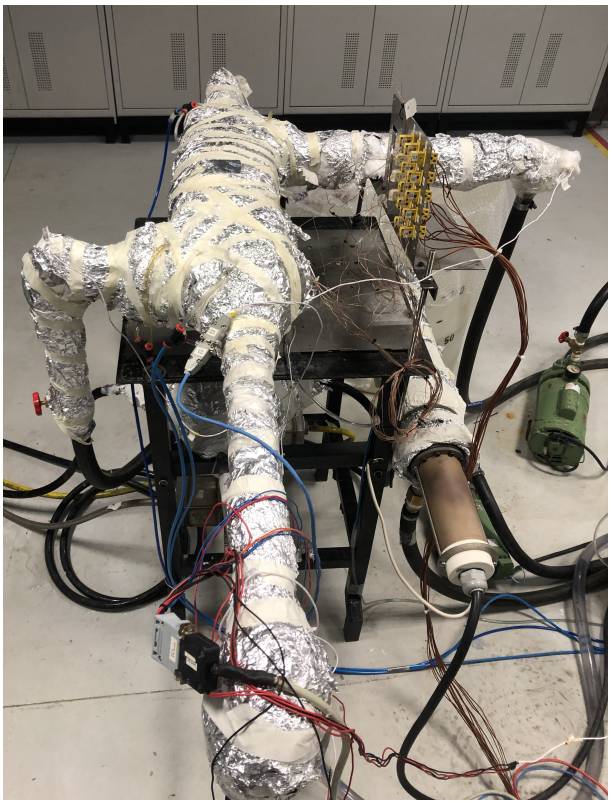

4.4 TEST PROCEDURE

In order to gather data to develop correlations for this new heat transfer geometry, the test procedure described in this section was performed. To start the workbench up, the first step was to turn on the cooling tower and open its valves, so water would flow inside the counterflow heat exchanger and the cryostat could then be turned on[3]. Subsequently, the computer and all measuring devices could be switched on. In the next step, the cold water circuit's pump was turned on and the volumetric flow rate was roughly adjusted based on test specifications. It was important to begin by starting the cold circuit up before the hot circuit was switched on to avoid overheating the prototype, which could make the glass shatter.

The second step was to turn the hot circuit's pump on and make sure water was flowing. Again, the volumetric flow rate was roughly adjusted based on targeted test specifications. Since the hot circuit pump was not connected to a control panel, the pump's rotational velocity could not be adjusted; it could only be switched on and off. Therefore, flow rate setting was made by a valve. Only then, the heater could be turned on by adjusting the electric tension controller.

Once water was flowing in both streams, it was time to remove the bubbles from the hoses used for pressure drop measurements by opening the valves and letting water

[3] The cryostat demanded an external cold water circuit to operate, so it was also connected to the cooling tower

and the air bubbles leave the system.

When the hot stream inlet temperature approached the desired test value, the operator successively adjusted the tension controller multiple times to bring system closer to a steady-state regime. In the meantime, the operator could set the cryostat to control the cold stream inlet temperature. In practice, however, the cold stream inlet temperature was kept as low as possible, by setting the lowest possible temperature in the cryostat without freezing the water near its serpentine.

After this initial setting, a cycle of adjustments would begin. At first, the operator needed to verify the flow meters and make necessary changes to obtain the desired values of volumetric flow rate. Afterwards, the operator checked once again the inlet temperatures to make sure they were adequate. This fine adjustment cycle would be repeated as many times as necessary to ensure adequate operating conditions in steady-state regime. Once all controllable parameters were correct and steady-state flow was achieved in both streams, data acquisition was performed.

The hot stream inlet temperature was set at two different levels for testing: 70°C and 80°C. For this stream, three target mass flow rates were specified: $0,1$kg/s, $0,15$kg/s and $0,2$kg/s. Such as mentioned, during all tests, the cold stream inlet temperature would be kept as low as possible. This was done to maximize the difference between the temperature distributions inside the heat exchanger. For each pair of parameters of the hot stream, the cold stream mass flow rate was varied covering a total of twelve test points. The minimum mass flow rate target was $0,01$kg/s followed by increases of $0,01$kg/s up to $0,06$kg/s. The following mass flow increases were of $0,02$kg/s until $0,16$kg/s was obtained. The final test consisted of adjusting the pump to its maximum power. In total, 72 test points were obtained. Table 15 shows all test configurations.

It is important to mention that test planning considered mass flow rates, because this is the important physical quantity related to the heat transfer rate inside the heat exchanger. The flow meters, however, measured the mean flow velocity, and since the tube's diameter had been previously set to both devices, the outputs were the volumetric flow rates of both streams. For the practical adjustment of the workbench, however, this did not impose any issues. During data analysis, the actual mass flow rates were calculated based on the measured volumetric flow rates and the water density. The density could be determined based on the temperature readings from the thermocouples placed near the flow meters.

Table 15 – Targeted hot stream inlet temperature and mass flow rates for every test point.

$T_{h,in}$ [°C]	$\dot{m}_h$ [kg/s]	$\dot{m}_c$ [kg/s]	$T_{h,in}$ [°C]	$\dot{m}_h$ [kg/s]	$\dot{m}_c$ [kg/s]
70	0,1	0,01	80	0,1	0,01
		0,02			0,02
		0,03			0,03
		0,04			0,04
		0,05			0,05
		0,06			0,06
		0,08			0,08
		0,10			0,10
		0,12			0,12
		0,14			0,14
		0,16			0,16
		0,17			0,17
	0,15	0,01		0,15	0,01
		0,02			0,02
		0,03			0,03
		0,04			0,04
		0,05			0,05
		0,06			0,06
		0,08			0,08
		0,10			0,10
		0,12			0,12
		0,14			0,14
		0,16			0,16
		0,17			0,17
	0,2	0,01		0,2	0,01
		0,02			0,02
		0,03			0,03
		0,04			0,04
		0,05			0,05
		0,06			0,06
		0,08			0,08
		0,10			0,10
		0,12			0,12
		0,14			0,14
		0,16			0,16
		0,17			0,17

5 HEAT EXCHANGER ANALYSIS AND MODELLING

5.1 THE FIRST LAW OF THERMODYNAMICS

The well-known First Law of Thermodynamics for an open system is

$$\sum_{in} \dot{m} \left(h + \frac{1}{2}\alpha_V \overline{V}^2 + gz \right) - \sum_{out} \dot{m} \left(h + \frac{1}{2}\alpha_V \overline{V}^2 + gz \right) + \dot{Q} - \dot{W} = \frac{dE}{dt} \tag{5.1}$$

where $\dot{Q}$ is the net heat rate absorbed by the system, $\dot{W}$ is the net work rate performed by the system, E is the system energy, $\dot{m}$ is the mass flow rate and the terms in parenthesis are the total specific enthalpy at each mass inlet and outlet. More specifically, h is the specific enthalpy, α_V is the kinetic energy coefficient, $\overline{V}$ is the mean fluid velocity, g is the acceleration of gravity and z is the height.

For a single stream of a heat exchanger, we can assume $\dot{W} = 0$. For steady state conditions, $dE/dt = 0$. Usually, negligible variations of kinetic energy and gravitational potential energy can be assumed. For the common case of a single inlet and a single outlet, this yields

$$\dot{m} \left(h_{in} - h_{out} \right) + \dot{Q} = 0 \tag{5.2}$$

which gives

$$\dot{Q} = \dot{m} \left(h_{out} - h_{in} \right) \tag{5.3}$$

Equation 5.3 enables the calculation of the net heat rate absorbed by a fluid stream. Therefore, for an exchanger isolated from the outer environment, the heat transfer rate from the hot stream to the cold one is

$$q = \dot{Q}_c = -\dot{Q}_h \tag{5.4}$$

where the sub-indexes c and h refer to the cold and hot streams, respectively. This yields

$$q = \dot{m}_c \left(h_{c,out} - h_{c,in} \right) = \dot{m}_h \left(h_{h,in} - h_{h,out} \right) \tag{5.5}$$

5.2 THERMAL CONDUCTANCE

The overall thermal resistance of a heat exchanger is given by the sum of all elementary resistances in serial arrangement, such as shown in Figure 57. The result is

$$\frac{1}{UA} = \frac{1}{\left(\eta_o \hbar A\right)_c} + \frac{R''_{f,c}}{\left(\eta_o A\right)_c} + R_w + \frac{R''_{f,h}}{\left(\eta_o A\right)_h} + \frac{1}{\left(\eta_o \hbar A\right)_h} \tag{5.6}$$

where η_o is the overall surface efficiency, $\hbar$ is the convection heat transfer coefficient, A is the total heat transfer area, R''_f is the fouling factor and R_w is the wall resistance. Such as in the last equation, the sub-indexes c and h refer to the cold a hot streams, respectively. The thermal conductance UA is the inverse of the overall resistance and is usually written as the product of the global heat transfer coefficient U and a reference area A.

Figure 57 – Thermal resistances in a heat exchanger.

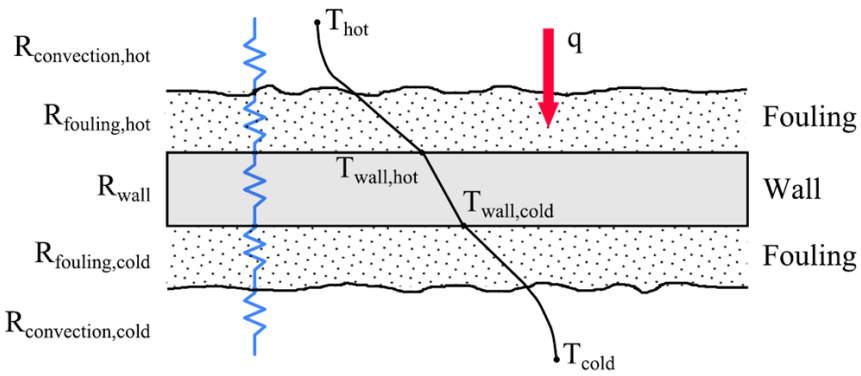

Sarmiento, Soares, Carqueja, et al. (2020)

To obtain the heat transfer rate based on the thermal conductance, equation 5.5 must be written in terms of the terminal temperatures. Assuming an enthalpy variation can be expressed as $\Delta h = c_p \Delta T$, one has

$$q = C_c \left(T_{c,o} - T_{c,i}\right) = C_h \left(T_{h,i} - T_{h,o}\right) \tag{5.7}$$

where $C = \dot{m} c_p$ is the thermal capacity rate.

It is widely shown in heat exchanger texts that, when considering parallel or counterflow configurations, the heat transfer rate is related to the terminal temperatures by

$$q = UA\Delta T_{lm} \tag{5.8}$$

where

$$\Delta T_{lm} = \frac{\Delta T_B - \Delta T_A}{\ln\left(\dfrac{\Delta T_B}{\Delta T_A}\right)} \tag{5.9}$$

is the logarithmic mean temperature difference (INCROPERA et al., 2014). In the last equation, ΔT_A and ΔT_B are the temperature differences of the fluid streams at each extremity of the heat exchanger. In the case of a counterflow arrangement, this yields

$$\Delta T_A = T_{h,i} - T_{c,o} \tag{5.10}$$

$$\Delta T_B = T_{h,o} - T_{c,i} \tag{5.11}$$

Notice that the definitions of ΔT_A and ΔT_B can be switched, without altering ΔT_{lm}.

When considering flow arrangements other than pure counterflow, a correction factor F can be introduced to equation 5.8 to reflect the departure from the counterflow arrangement (HESSELGREAVES, 2000):

$$q = FUA\Delta T_{lm} \tag{5.12}$$

When $F \to 1$, the operating performance tends to that of a pure counterflow heat exchanger under the same operating conditions.

In a heat exchanger, the stream with minimum thermal capacity rate C has the highest temperature variation, which can be verified by quickly examining equation 5.7. Therefore, the maximum possible heat transfer rate in a heat exchanger is

$$q_{max} = C_{min}\left(T_{h,i} - T_{c,i}\right) \tag{5.13}$$

where $C_{min} = \min\{C_c, C_h\}$.

The heat exchanger effectiveness is defined as the ratio of the actual heat transfer rate to the maximum possible heat transfer rate:

$$\varepsilon \coloneqq \frac{q}{q_{max}} \tag{5.14}$$

The ratio of heat capacity rates is defined as

$$C_r \coloneqq \frac{C_{min}}{C_{max}} \tag{5.15}$$

where $C_{max} = \max\{C_c, C_h\}$. The number of thermal units is defined as

$$Ntu \coloneqq \frac{UA}{C_{min}} \tag{5.16}$$

It is widely shown, in heat exchanger textbooks, that the effectiveness can be expressed, for any flow arrangement, as a function of C_r and Ntu (INCROPERA et al., 2014; SHAH; SEKULIC, 2003). Each flow arrangement will have a specific function form $\varepsilon = f(C_r, Ntu)$. Considering a counterflow heat exchanger, this is given by

$$\varepsilon = \frac{\exp\left[Ntu\left(C_r - 1\right)\right] - 1}{C_r \exp\left[Ntu\left(C_r - 1\right)\right] - 1} \tag{5.17}$$

in the case where $C_r \neq 1$ and

$$\varepsilon = \frac{Ntu}{Ntu + 1} \tag{5.18}$$

if $C_r = 1$. This is an expected result, since

$$\lim_{C_r \to 1} \frac{\exp\left[Ntu\left(C_r - 1\right)\right] - 1}{C_r \exp\left[Ntu\left(C_r - 1\right)\right] - 1} = \frac{Ntu}{Ntu + 1} \tag{5.19}$$

5.3 IMPLEMENTATION

For the present analysis, absence of fouling is assumed. This yields (see equation 5.6)

$$\frac{1}{UA} = \frac{1}{\left(\eta_o \hbar A\right)_c} + R_w + \frac{1}{\left(\eta_o \hbar A\right)_h} \tag{5.20}$$

Hence, the thermal conductance is a function of the heat transfer coefficients, the total heat transfer areas and overall efficiencies of the cold and hot streams, as well as the wall resistance.

In a standard modelling problem, the convective coefficients of both streams must be calculated, just as the wall resistance (the surface efficiencies also depend on the convective coefficients), so the thermal conductance can be determined. An appropriate $\varepsilon = f\left(C_r, Ntu\right)$ relationship allows for the determination of the heat transfer rate and hence the outlet temperatures. Because thermodynamic properties are temperature-dependent, iterations might be performed for higher accuracy.

In the present case, however, the thermal conductance can be obtained from experimental data. Furthermore, there are no specific convective correlations for the developed pin-fin geometry. Therefore, it is our goal to determine the cold stream convective coefficient based on the experimental data from the tests and on other necessary theoretical data. Hence, $\hbar_h$ and R_w will be theoretically calculated by validated models, so that the first term on the right-hand side of equation 5.20 can be determined (as already mentioned, $1/UA$ arises from experimental data). The convective coefficient can then be later used for performance calculations, as will be shown in chapter 6.

The hot stream convective coefficient will be calculated by the implementation of Gnielinski's correlation, which has previously been successfully used in other studies (CARQUEJA, 2017). The channel length is an important parameter when developing flow is present. Sarmiento, Soares, Carqueja, et al. (2020) showed that, for S-shaped channels, an optimal length consisting of the intermediate value between the core length and the effective S-shaped channel length can be used. The effective length consists of the length of the S-shaped channels inside the heat transfer region, which means that the inlet and outlet regions are discounted from the total channel length.

The heat exchanger's core can be modelled as a flat plate (separation plate) with fins on both sides. Therefore, the wall conduction resistance is

$$R_w = \frac{\delta_w}{kA_w} \tag{5.21}$$

where δ_w is the wall thickness, k is the material's thermal conductivity and A_w the heat conduction area.

To consider the presence of fins in the analysis, fin efficiency must be defined. Denoted by η_f, it is the ratio of the actual heat transfer rate through the fin to its maximum theoretical value, which would be obtained if the entire fin were kept at the same temperature as its base. One then obtains

$$\eta_f \coloneqq \frac{q_f}{q_{f,max}} = \frac{q_f}{\hbar A_f \theta_b} \tag{5.22}$$

where q is the heat transfer rate through the fin, $\hbar$ is the heat transfer coefficient, A_f is the heat transfer area and θ_b is the temperature difference between the base of the fin and the free stream.

The extended surface theory defines the overall surface efficiency η_o as the actual heat transfer rate of the entire surface divided by its maximal theoretical value, which

would be obtained if the entire surface were maintained at the same temperature as the base of the fins. This allows one to write

$$\eta_o \coloneqq \frac{q}{q_{max}} = \frac{q}{\hbar A_t \theta_b} \tag{5.23}$$

where A_t is the total heat transfer area. For N_f fins, each with a heat transfer area A_f and a base with heat transfer area A_b, it can be shown that

$$\eta_o = 1 - \frac{N_f A_f}{A_t}\left(1 - \eta_f\right) \tag{5.24}$$

Fin efficiency has been calculated for many different fin geometries and the results are well documented in the literature (INCROPERA et al., 2014; ÇENGEL; GHAJAR, 2014). Considering the particular case of a fin with an adiabatic tip, its efficiency is given by

$$\eta_f = \frac{\tanh\left(m_f L_f\right)}{m_f L_f} \tag{5.25}$$

being L_f the fin length and

$$m_f^2 = \frac{\hbar P}{k A_{cf}} \tag{5.26}$$

where P is the fin perimeter and A_{cf} its cross-sectional area.

The computational implementation involves, at first, reading the experimental data, which are subjected to metrological procedures to determine the directly measured variables (temperatures, pressure drops and volumetric flow rates). This is explained in detail in appendix B. Specific enthalpy variations of both streams are calculated to, combined with the mass flow rates, determine the heat transfer rate of each test point. Terminal temperatures are used to calculate the logarithmic mean temperature difference in each case. The thermal conductance is then obtained.

At this point, a hypothetical temperature distribution inside the heat exchanger is assumed. More specifically, temperatures for all nodes in the thermal circuit of figure 57 are first estimated. Mean fluid temperatures along the streams are directly determined based on the measured tempratures. The hot stream convective coefficient is then determined based on Gnielinski's correlation (equation 2.7). Thermodynamic properties are determined based on mean temperatures, whereas properties based on wall temperature are calculated based on the hypothetical temperature distribution. The wall resistance is then determined based on geometric parameters and the neighboring nodes' temperatures, which are used to calculate thermal conductivity. So far, the left-hand side and the first two terms on the right-hand side of equation 5.20 are known, allowing the calculation of the last term $1/\left(\eta_o \hbar A\right)_c$. The results are used to determine a more accurate temperature distribution inside the heat exchanger. The new temperature values are used to determine thermophysical properties with higher accuracy and a new iteration begins. Iterations are carried out until convergence.

Figure 58 – Algorithm structure.

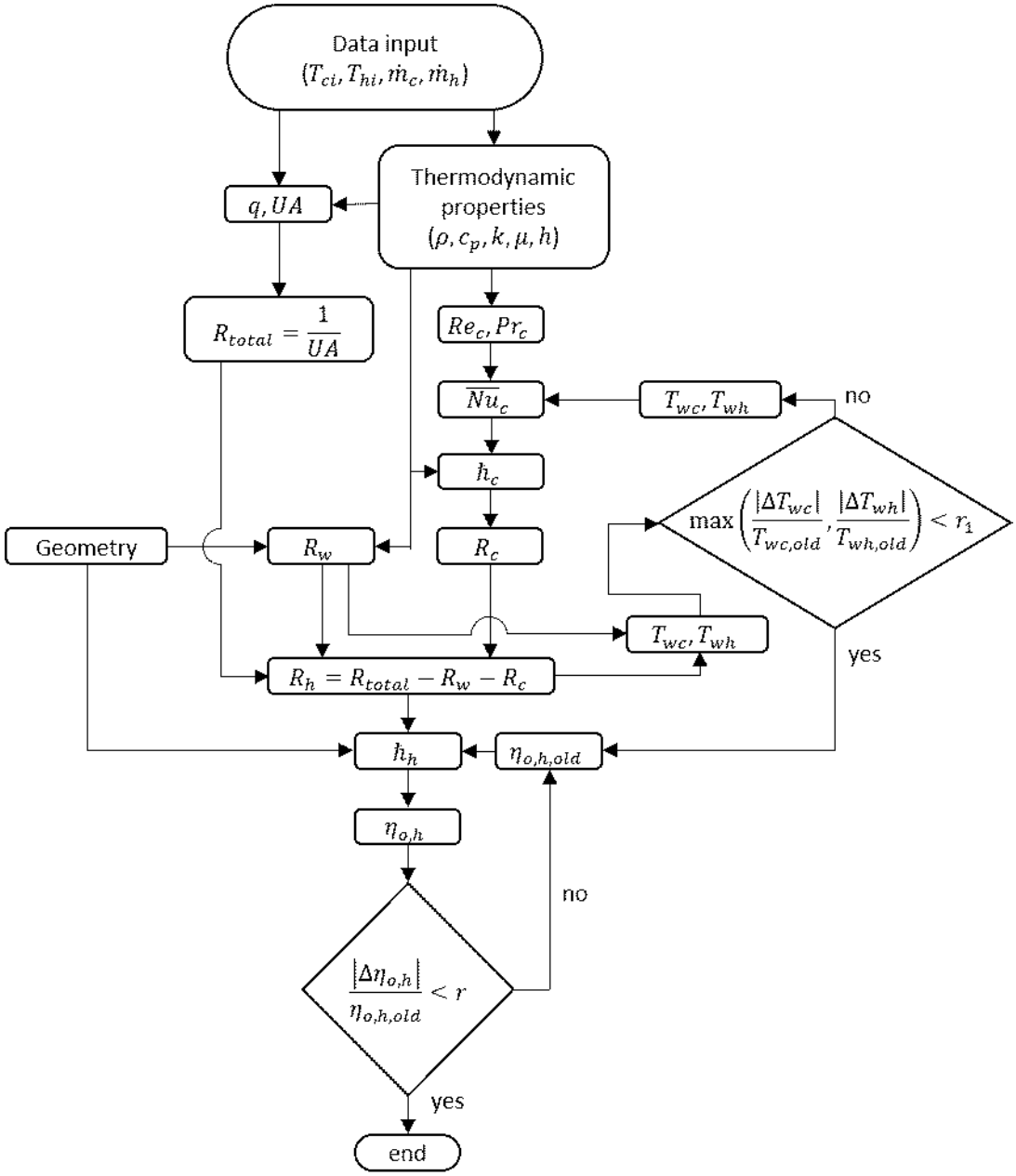

In the end, a converged value of $1/(\eta_o \hbar A)_c$ is found. At this point, $\hbar_c$ must be determined. An initial estimate of η_o is considered. This allows the convective coefficient to be calculated for the first time. Based on the obtained value, the overall surface efficiency is calculated. The new value of η_o is used to determine $\hbar_c$ with higher accuracy. Once again, iterations are carried out until convergence. The entire structure of the algorithm can be seen in figure 58.

5.4 PRESSURE DROP

Since pumping power is directly proportional to pressure drop, it is of great importance to analyze and model such phenomenon when dealing with heat exchangers. In

the case of phase change, the pressure distribution determines the temperature distribution along the stream. For the purposes of this work, only single-phase heat transfer is considered.

According to Fox, Mcdonald, and Pritchard (2014), head loss is defined as the irreversible conversion of mechanical energy into thermal energy, either in the form of internal energy or in the form of heat, due to friction. Considering an internal, steady-state incompressible flow, the head loss between points 1 and 2 (where point 2 is located downstream relative to point 1) is

$$h_{lT} = \left(\frac{p}{\rho} + \alpha_V \frac{\overline{V}^2}{2} + gz\right)_1 - \left(\frac{p}{\rho} + \alpha_V \frac{\overline{V}^2}{2} + gz\right)_2 = u_2 - u_1 - \frac{\delta Q}{\delta m} \tag{5.27}$$

where the terms in parenthesis represent the specific mechanical energy. The specific internal energy is denoted by u, whereas $\delta Q/\delta m$ represents the heat transfer per unit mass. In a horizontal tube with constant cross-section and fully developed incompressible flow, the head loss is

$$h_{lT} = \frac{\Delta p}{\rho} \tag{5.28}$$

where Δp is the pressure drop.

The total head loss can be expressed as the sum of major and minor losses, denoted by h_l and h_{lm}, respectively. Major losses are the ones related to fully developed flows inside ducts with constant cross-section, whereas minor losses are related to entries and exits, area changes and so on. The major losses can be expressed as

$$h_l = f_D \frac{L}{d} \frac{\overline{V}^2}{2} \tag{5.29}$$

where f_D is the Darcy friction factor, L is the tube length and d the tube's internal diameter. When laminar flow is present, $f_D = 64/Re$. Considering turbulent flow, the Darcy friction factor can be obtained by the Colebrook equation (equation 2.12)

$$\frac{1}{\sqrt{f_D}} = -2,0 \log\left(\frac{e/d}{3,7} + \frac{2,51}{Re\sqrt{f_D}}\right)$$

Minor losses are calculated either by

$$h_{lm} = K_l \frac{\overline{V}^2}{2} \tag{5.30}$$

where K_l is the loss coefficient, or by

$$h_{lm} = f_D \frac{L_e}{d} \frac{\overline{V}^2}{2} \tag{5.31}$$

where L_e is the equivalent tube length.

When considering heat exchangers, pressure drops are associated with two major contributions: pressure drop due to the core and pressure drop resulting from peripheral

devices, such as headers, manifolds, ducts and so on. The further analysis assumes that the flow distribution through the core is uniform.

The core pressure drop consists of one or more of the following contributions (SHAH; SEKULIC, 2003):

- Skin friction and form drag
- Changes of fluid density in the core
- Sudden contraction and expansion at inlet and outlet
- Change in elevation between inlet and outlet

Figure 59 shows a flow passage in a plate-fin heat exchanger and an associated, arbitrary pressure distribution. The incoming flow is assumed to be uniform. As it enters the passage, contraction happens due to a change in flow area. Flow separation followed by expansion takes place. Inside the core, skin friction is present. Depending on the core geometry, form drag and further expansions and contractions can take place. Variations in fluid density related to the heat transfer process and its inherent temperature variations can cause velocity changes as well. At the core exit, there is another change in flow area, so that expansion takes place. The total pressure drop related to one stream, based on the nomenclature presented in Figure 59, can be expressed as

$$\Delta p = \Delta p_{21} + \Delta p_{32} - \Delta p_{34} \tag{5.32}$$

where $\Delta p_{ij} = p_j - p_i$ is the pressure difference between points j and i, according to Figure 55. Hence, Δp_{21} is the pressure drop at the entrance, Δp_{32} is the core pressure drop and Δp_{34} is the pressure rise at the exit.

Figure 59 – Pressure drop along a stream.

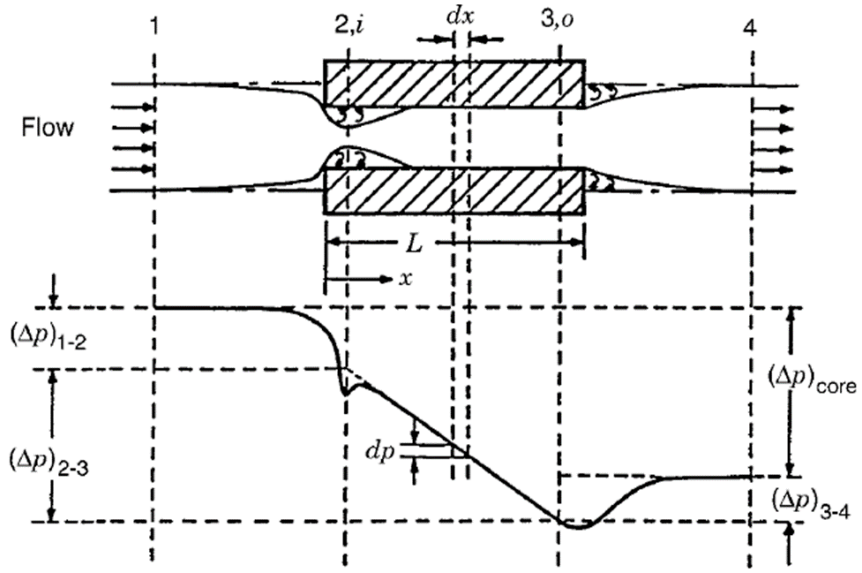

Shah and Sekulic (2003)

5.4.1 Core pressure drop

The core pressure drop consists of two contributions: pressure loss due to fluid friction and pressure change due to momentum rate change. The first contribution takes into account both skin friction and form drag. The influence of internal contractions and expansions due to flow area changes, if present, are also lumped into the core friction loss term.

Consider a differential control volume inside a flow passage in steady state regime. The fluid enters the control volume with a velocity V and leaves it with a velocity V_{x+dx}. Let A_o be the control volume's cross-sectional area. This yields

$$\dot{m}V_{x+dx} - \dot{m}V = (p - p_{x+dx})\, A_o - \tau_w P dx$$

where p is the pressure at the inlet, p_{x+dx} is the pressure at the outlet, τ_w is the wall shear stress and P is the wetted perimeter. This yields

$$-\frac{dp}{dx} = G^2 \frac{d}{dx}\left(\frac{1}{\rho}\right) + \tau_w \frac{P}{A_o}$$

It is important to mention that, in the present analysis, A_o is considered to be constant, which is normally the case in many heat exchangers. It will be explained later that the same analysis can be expanded to the more general case where the cross-sectional area is not constant along flow length.

The last equation can be rewritten as

$$-\frac{dp}{dx} = \frac{G^2}{2}\left[2\frac{d}{dx}\left(\frac{1}{\rho}\right) + f\frac{1}{\rho\dfrac{A_o}{P}}\right]$$

where the concept of friction factor was used. Mathematically, it is given by

$$f = \frac{\tau_w}{\dfrac{1}{2}\rho\overline{V}^2} \tag{5.33}$$

Recognizing that

$$\frac{d}{dx}\left(\frac{1}{\rho}\right) = -\frac{1}{\rho^2}\frac{d\rho}{dx}$$

one has

$$-\frac{dp}{dx} = \frac{G^2}{2}\left[-2\frac{1}{\rho^2}\frac{d\rho}{dx} + f\frac{1}{\rho\dfrac{A_o}{P}}\right]$$

The last equation can be integrated throughout the entire core length, yielding

$$\Delta p_{32} = \frac{G^2}{2}\left[2\left(\frac{1}{\rho_o} - \frac{1}{\rho_i}\right) + f\frac{4}{d_h}\int_0^L \frac{dx}{\rho}\right]$$

The sub-index i refers to the inlet, whereas the sub-index o refers to the outlet. Defining the mean specific volume as

$$\left(\frac{1}{\rho}\right)_m = \frac{1}{L}\int_0^L \frac{dx}{\rho} \tag{5.34}$$

one gets

$$\Delta p_{32} = \frac{G^2}{2\rho_i}\left[2\left(\frac{\rho_i}{\rho_o} - 1\right) + f\frac{4L}{d_h}\rho_i\left(\frac{1}{\rho}\right)_m\right] \tag{5.35}$$

Hence, the pressure drop consists of the contribution of two terms. The first term represents momentum rate changes related to variations in density. The second term is related to frictional losses.

This equation was obtained based on the analysis a one-dimensional flow with constant flow area. However, as previously stated, the influence of internal contractions and expansions due to flow area changes, if present, are also lumped into the core friction loss term. In practice, heat transfer surfaces are characterized by the friction factor as a function of the Reynolds number.

In the case of an incompressible fluid, this can be simplified to

$$\Delta p_{32} = \frac{G^2}{2\rho_i} f\frac{4L}{d_h} \tag{5.36}$$

This result is in accordance with the previously presented result for the head loss, provided that $f_D = 4f$.

5.4.2 Core entrance pressure drop

Considering no difference in height between points 1 and 2, upstream and downstream of the entrance region, respectively, equation 5.27 becomes

$$h_{lT} = \left(\frac{p}{\rho_i} + \frac{\overline{V}^2}{2}\right)_1 - \left(\frac{p}{\rho_i} + \frac{\overline{V}^2}{2}\right)_2 \tag{5.37}$$

where it is assumed that $\alpha_{V,1} = \alpha_{V,2} = 1$. Hence, the pressure drop between these points is given by

$$p_1 - p_2 = \rho_i \left[h_{lT} + \frac{1}{2}\left(\overline{V}_2^2 - \overline{V}_1^2\right)\right] \tag{5.38}$$

The core entrance pressure drop consists of two contributions: pressure drop due to flow area change and pressure losses associated with irreversible effects. The first term is represented by $\frac{\rho}{2}\left(\overline{V}_2^2 - \overline{V}_1^2\right)$, which is the pressure drop related to an inviscid, incompressible flow subjected to the same area change as the real flow. Based on the continuity equation,

$$\rho_i \overline{V}_1 A_{o,1} = \rho_i \overline{V}_2 A_{o,2} \tag{5.39}$$

The ratio of the inlet flow area to the total frontal area is defined as

$$\sigma_i \coloneqq \frac{A_{o,2}}{A_{o,1}} \tag{5.40}$$

This enables one to write

$$\frac{\rho_i}{2}\left(\overline{V}_2^2 - \overline{V}_1^2\right) = \frac{\rho_i \overline{V}_2^2}{2}\left(1 - \sigma_i^2\right) = \frac{G_2^2}{2\rho_i}\left(1 - \sigma_i^2\right) \tag{5.41}$$

where $G_2 = \rho_i \overline{V}_2$ is the core mass velocity at section 2.

The second contribution to the pressure drop is related to irreversible losses associated to area change at the inlet. This is represented by the associated head loss between points 1 and 2 and is represented by ρh_{lT} in equation 5.38. Being a minor loss, this is modelled by equation 5.30:

$$h_{lT} = h_{lm} = K_c \frac{\overline{V}_2^2}{2} = K_c \frac{G_2^2}{2\rho_i^2} \tag{5.42}$$

where K_c is the contraction loss coefficient. Values for K_c are given in Figure 60.

Hence, the core entrance pressure drop is given by

$$\Delta p_{21} = p_1 - p_2 = \frac{G_2^2}{2\rho_i}\left(1 - \sigma_i^2 + K_c\right) \tag{5.43}$$

Again, one can see that the total pressure drop is the sum of two contributions, one associated to area contraction and represented by $\frac{G_2^2}{2\rho_i}\left(1 - \sigma_1^2\right)$, and the other associated to head loss and represented by $\frac{G_2^2}{2\rho_i} K_c$.

Figure 60 – K_c and K_e.

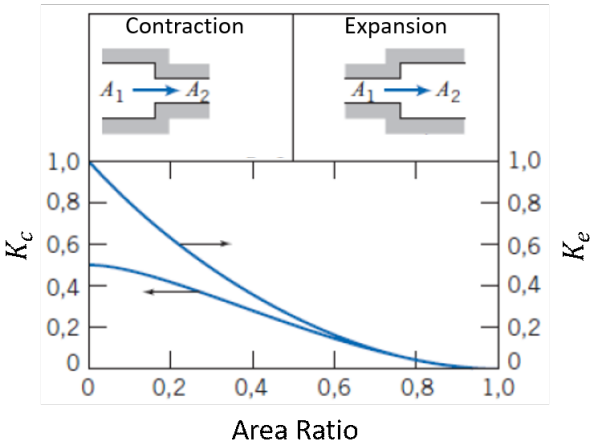

Adapted from Fox, Mcdonald, and Pritchard (2014).

5.4.3 Core exit pressure rise

Just as before, the core exit pressure rise consists of two contributions: the first one is associated to a velocity decrease due to flow area increase, whereas the second one is associated to the related head loss. Considering no difference in height between points 3 and 4, equation 5.27 becomes:

$$h_{lT} = \left(\frac{p}{\rho_o} + \frac{\overline{V}^2}{2}\right)_3 - \left(\frac{p}{\rho_o} + \frac{\overline{V}^2}{2}\right)_4 \tag{5.44}$$

where, again, it is assumed that $\alpha_{V,3} = \alpha_{V,4} = 1$. After appropriate development, one gets

$$\Delta p_{34} = \frac{G_3^2}{2\rho_o}\left(1 - \sigma_o^2 - K_e\right) \tag{5.45}$$

where σ_o is the ratio of minimal to maximal flow area at the outlet and K_e is the expansion loss coefficient, also shown in figure 60.

5.4.4 Total core pressure drop

The total core pressure drop is given by the sum of all elementary pressure drops previously considered. This yields

$$\Delta p = \frac{G^2}{2\rho_i}\left[1 - \sigma_i^2 + K_c + 2\left(\frac{\rho_i}{\rho_o} - 1\right) + f\frac{4L}{d_h}\rho_i\left(\frac{1}{\rho}\right)_m - \frac{\rho_i}{\rho_o}\left(1 - \sigma_o^2 - K_e\right)\right] \tag{5.46}$$

This equation was obtained based on the analysis of a one-dimensional flow with constant flow area. However, as previously stated, the influence of internal contractions and expansions due to flow area changes, if present, are also lumped into the core friction loss term. In practice, heat transfer surfaces are characterized by the friction factor as a function of the Reynolds number.

6 BASIC PERFORMANCE PARAMETERS

According to Hesselgreaves (2000), when considering a a heat transfer surface, or, equivalently, a heat exchanger stream, *the design requirement is specified by Number of Thermal Units, pressure drop and mass flow rate for the side considered.* Aiming the selection of the best heat exchange technologies, the performance of different surfaces can be compared based on appropriate functions of relevant variables. In this chapter, parameters will be introduced, which will allow the thermohydraulic performance of the present pin-fin geometry to be compared to that of other heat transfer surfaces. Results will be given in the next chapter.

In the present development, the surface performance is assumed to be describable by the Colburn j factor and the Fanning friction factor f, both functions of the Reynolds number. According to Hesselgreaves (2000), the Colburn factor gives an approximate rationalization of the heat transfer coefficient over a wide range of Prandtl numbers. According to the author, *this will be valid for most high performance surfaces down to Reynolds numbers of about 400, but excludes laminar flows.*

According to Hesselgreaves (2000), the fundamental parameter describing compactness is the hydraulic diameter d_h, defined as

$$d_h \coloneqq \frac{4A_cL}{A_s} \tag{6.1}$$

where A_c is the cross-sectional flow area, L is the flow length and A_s is the total heat transfer area of the stream. In the case where A_c varies with flow length, one can write

$$d_h = \frac{4V_s}{A_s} \tag{6.2}$$

where V_s is the enclosed volume.

The porosity is defined as the ratio between the enclosed volume and the heat exchanger's total volume V:

$$\sigma \coloneqq \frac{V_s}{V} \tag{6.3}$$

Still according to Hesselgreaves (2000), the surface area density is defined as the ratio between the surface's total heat transfer area and the heat exchanger's total volume, yielding

$$\beta \coloneqq \frac{A_s}{V} \tag{6.4}$$

which can also be expressed as

$$\beta = \frac{4\sigma}{d_h} \tag{6.5}$$

The Stanton number is defined as the ratio between the Nusselt number and the Péclet number, the latter one being equal to the product of the Reynolds number by the Prandtl number:

$$St \coloneqq \frac{Nu}{RePr} = \frac{\hbar}{Gc_p} \tag{6.6}$$

where $G = \rho\overline{V} = \dot{m}/A_c$ is the mass velocity. Thus, the Stanton number, just as the Nusselt number, is a way of non-dimensionalizing the heat transfer coefficient.

The Colburn j factor is defined as

$$j \coloneqq \frac{Nu}{RePr^{1/3}} \tag{6.7}$$

which can also be expressed as

$$j = StPr^{2/3} \tag{6.8}$$

Thus, the heat transfer coefficient $\hbar$ can be expressed in terms of the Nusselt number, the Stanton number and the Colburn factor. In the latter case, one has

$$\hbar = Gc_p jPr^{-2/3} = \frac{\dot{m}}{\mu} kPr^{1/3} \frac{j}{A_c} \tag{6.9}$$

Just as previously mentioned in chapter 5, it can be written, for any stream, that

$$\dot{Q} = \dot{m}c_p \left(T_{out} - T_{in}\right) = \hbar A_s \overline{\Delta T} \tag{6.10}$$

The stream's Number of Thermal Units N can then be defined as

$$N \coloneqq \frac{T_{out} - T_{in}}{\overline{\Delta T}} \tag{6.11}$$

which yields

$$N = \frac{\hbar A_s}{C} \tag{6.12}$$

Notice that N designates number of thermal units of a single stream, whereas Ntu refers to the heat exchanger as a whole. Those are, therefore, different definitions.

To compare both definitions of number of transfer units, one can consider a heat exchanger whose resultant thermal resistance can be approximated by the convective resistance of a single stream. In this case,

$$\frac{1}{UA} \approx \frac{1}{\hbar A_s}$$

As long as $A = A_s$, then $U \approx \hbar$. Note that, if the conduction resistance is negligible, it is probably safe to assume that $\eta_o \approx 1$ if fins are not too long. If the considered stream has, in fact, the minimum heat capacity rate C, then $Ntu = UA/C_{min} \approx \hbar A_s/C = \mathrm{N}$.

When specifying the constraints of heat exchanger design, it is common practice to know inlet temperatures and mass flow rates, as well as the required temperature variation of one stream, which, in turn, allows one to obtain the outlet temperature of the other stream. In this case, both the heat transfer rate and the logarithmic mean temperature difference between the streams are constrained, and so is the thermal conductance, given that $UA = q/\Delta T_{lm}$. Therefore, the heat exchanger's Number of Transfer Units Ntu will also be constrained, since $Ntu = UA/C_{min}$. Considering again the case where the resultant thermal resistance can be represented by one stream's convective resistance,

then this side's Number of Transfer Units will also be constrained, since, in this case, $N \approx Ntu$. The assumption that the stream's Number of Transfer Units is constrained by design specifications will be kept throughout the following development, just as done by Hesselgreaves (2000).

To further illustrate the meaning of constraining parameter N, a simple example can be examined. Consider a heat transfer surface kept at a constant temperature T_s. Fluid, at a specific mass flow rate $\dot{m}$, flows around the surface. Its inlet temperature is T_{in}, whereas the outlet temperature T_{out} must be downstream as a design constraint. As the fluid flows along the surface, its temperature gradually changes from T_{in} to T_{out}, forming a temperature distribution along the flow direction. Naturally, the temperature distribution depends on both terminal temperatures and on the convective coefficient. The mean temperature difference between fluid and plate is $\overline{\Delta T}$. If the convective coefficient is constant, the temperature distribution will always have the same shape. Therefore, $\overline{\Delta T}$ will always be the same function of T_{in} and T_{out}, regardless of the surface's outer dimensions. More specifically, it will be given by the logarithmic mean temperature difference. Since all fluid temperatures are constrained, so is the temperature distribution and also the mean temperature difference $\overline{\Delta T}$. Therefore, the stream's Number of Transfer Units is also constrained (see equation 6.11). The degrees of freedom the designer has left to work with are hydraulic diameter, cross-sectional surface and flow length. It is important to notice that these three parameters demand a further constraint for the solution to be unique.

Based on equations 6.9 and 6.11, the Colburn factor can be expressed as

$$j = \frac{\hbar A_c}{\dot{m} c_p} Pr^{2/3} = \frac{A_c}{A_s} Pr^{2/3} N \tag{6.13}$$

Since $d_h = 4A_c L / A_s$,

$$j = \frac{d_h}{4L} Pr^{2/3} N \tag{6.14}$$

This result will be often used in further developments. For given conditions, the product $Pr^{2/3}N$ is fixed (notice that the fluid is also prescribed by assuming Pr is fixed), so for two surfaces suffixed 1 and 2 to be compared **under the same thermal constraint**, their lengths must be related by

$$\frac{L_1}{L_2} = \frac{d_{h1}}{d_{h2}} \frac{j_2}{j_1} \tag{6.15}$$

Thus, flow length is directly proportional to hydraulic diameter, and inversely proportional to the Colburn factor, which, in turn, is a function of the Reynolds number. In fact, j rises as the Reynolds number decreases, the latter being proportional to the hydraulic diameter. Hence, reducing the hydraulic diameter reduces Re, which, in turn, increases j. Therefore, the flow length decreases as the hydraulic diameter decreases.

The pressure drop can be expressed, for the general case, by[1]

$$\Delta p = \frac{1}{2}\rho \overline{V}^2 \frac{4L}{d_h} f \tag{6.16}$$

This yields, after some manipulation,

$$\frac{2\rho \Delta p}{\dot{m}^2} = f \frac{4L}{d_h A_c^2} \tag{6.17}$$

Combining equations 6.14 and 6.17, one has

$$\frac{2\rho \Delta p}{\dot{m}^2} = \frac{f Pr^{2/3} N}{j A_c^2} \tag{6.18}$$

which yields

$$\frac{G^2}{2\rho \Delta p} = \frac{j/f}{Pr^{2/3} N} \tag{6.19}$$

This equation is known as the core mass velocity equation.

The pumping power of a stream with volumetric flow rate $\dot{V}$ and pressure drop Δp is $\dot{W}_p = \dot{V} \Delta p$. Hence, for a stream in a heat exchanger,

$$\dot{W}_p = \frac{\dot{m} \Delta p}{\rho} \tag{6.20}$$

which is fixed if Δp is fixed. If, however, the pressure drop is not previously informed, one can write, based on equation 6.17 and, afterwards, on equation 6.18,

$$\dot{W}_p = \frac{2 f L \dot{m}^3}{\rho^2 d_h A_c^2} = \frac{f}{j} \frac{1}{A_c^2} \frac{\dot{m}^3 Pr^{2/3} N}{2\rho^2} \tag{6.21}$$

Consider two heat transfer surfaces 1 and 2 with **similar mass flow and pressure drop requirements**. This means that Δp and $\dot{m}$ are the same for both surfaces. The corresponding flow cross-sectional areas can be compared, based on equation 6.17, by

$$\frac{A_{c1}^2}{A_{c2}^2} = \frac{f_1}{f_2} \frac{L_1}{L_2} \frac{d_{h2}}{d_{h1}} \tag{6.22}$$

where, again, the same fluid is used in both cases. In order to consider not only the pressure drop, but also the thermal requirement in the cross-sectional area comparison, the hydraulic diameters in equation 6.22 are substituted by a function of thermal requirement, i.e., equation 6.14. A similar procedure was performed to obtain equation 6.19. Recognizing that $G = \dot{m}/A_c$ and that all terms, except for j/f, must remain constant, one finds

$$\frac{A_{c1}^2}{A_{c2}^2} = \frac{f_1}{f_2} \frac{j_2}{j_1}$$

The same result could be found by combining equations 6.15 and 6.22. This yields

$$\frac{A_{c1}}{A_{c2}} = \left(\frac{j_2/f_2}{j_1/f_1} \right)^{1/2} \tag{6.23}$$

[1] Comparison between this equation and equation 5.46 reveals that core inlet and outlet effects were neglected, and fluid density was assumed constant.

The ratio j/f is called Flow Area Goodness Factor (HESSELGREAVES, 2000). The last equation is the ratio of cross-sectional flow areas for two surfaces under the same thermal and pressure drop requirements. This means that, for two heat transfer surfaces of different geometries subjected to the same values of N, $\dot{m}$ and Δp, the cross-sectional flow areas are related according to equation 6.23. One can see that A_c decreases as the area goodness factor increases. Once again, the same fluid is used in the comparison. Since Δp, $\dot{m}$ and ρ are the same for both surfaces, the pumping power is also the same.

The cross-sectional area of the heat exchanger is $C_s = A_c/\sigma$, so for this parameter to be compared between two heat exchangers **under the same pressure drop and thermal requirements**, this equation is combined with equation 6.23, yielding

$$\frac{C_{s1}}{C_{s2}} = \frac{(j_2/f_2)^{1/2}\,\sigma_2}{(j_1/f_1)^{1/2}\,\sigma_1} \tag{6.24}$$

Again, this comparison is valid for the case where N, $\dot{m}$ and Δp are the same for both surfaces, and the same fluid is used.

The overall volume of the heat exchanger is given by $V = C_s L$. Thus, based on equations 6.15 and 6.24, the volume ratio of two heat exchangers using two different heat transfer surfaces 1 and 2 **under the same thermal and pressure drop requirements** is

$$\frac{V_1}{V_2} = \frac{\left(j_2^3/f_2\right)^{1/2} d_{h1}\sigma_2}{\left(j_1^3/f_1\right)^{1/2} d_{h2}\sigma_1} \tag{6.25}$$

Notice that this result compares the resulting heat exchanger volumes when two different heat transfer surfaces are considered for a specific stream. The overall volume depends, naturally, on the other stream as well, and the solid volume of the heat exchanger core must also be taken into consideration. All these factors are represented by the porosity. Given that $V_s = \sigma V$, the fluid volumes related to both heat transfer surfaces when **subjected to the same thermal and pressure drop requirements** are related by

$$\frac{V_{s,1}}{V_{s,2}} = \frac{\left(j_2^3/f_2\right)^{1/2} d_{h1}}{\left(j_1^3/f_1\right)^{1/2} d_{h2}} \tag{6.26}$$

Hence, the fluid volume decreases as the hydraulic diameter decreases, j increases and the area goodness factor increases.

The material volume of the heat exchanger is $V_m = V - V_{s,c} - V_{s,h} = V\,(1 - \sigma_c - \sigma_h) = V\,(1 - \sigma')$. Notice that the fluid volumes of both streams (cold and hot) were subtracted from the overall volume. In the equation, $\sigma' = \sigma_c + \sigma_h$ is the resulting porosity, and represents the total fluid volume of both streams divided by the exchanger's overall volume. Therefore, **for the same pressure drop and thermal requirements**, the ratio of material volumes of two heat exchangers using two different heat transfer

surfaces 1 and 2 for a stream is

$$\frac{V_{m1}}{V_{m2}} = \frac{V_1\,(1-\sigma_1')}{V_2\,(1-\sigma_2')} = \frac{\left(j_2^3/f_2\right)^{1/2} d_{h1}\sigma_2'\,(1-\sigma_1')}{\left(j_1^3/f_1\right)^{1/2} d_{h2}\sigma_1'\,(1-\sigma_2')} \tag{6.27}$$

This shows one that, when comparing two surfaces with compatible j/f ratios, for the same operating conditions, both exchanger volume and material volume are low when j is high, d_h is low and the porosity is high (σ' increases when any stream-related porosity increases). Once again, it is worth mentioning that the porosity depends on more characteristics than only the ones relative to a single stream.

6.1 OPERATING PARAMETER

The last equations do not give any indication of the operating Reynolds number. Considering again the same operating conditions (which includes the same fluid), the Reynolds numbers of two heat exchange surfaces can be compared by writing

$$\frac{Re_1}{Re_2} = \frac{\overline{V}_1 d_{h1}}{\overline{V}_2 d_{h2}} = \frac{d_{h1}}{d_{h2}}\frac{A_{c2}}{A_{c1}}$$

When considering two heat transfer surfaces **under the same thermal and pressure drop requirements**, equation 6.23 can be used, which enables one to write

$$\frac{Re_1}{Re_2} = \left(\frac{j_1/f_1}{j_2/f_2}\right)^{1/2} \frac{d_{h1}}{d_{h2}} \tag{6.28}$$

This means that, for the same operating (thermal and pressure drop related) conditions,

$$\frac{Re_1}{d_{h1}\,(j_1/f_1)^{1/2}} = \frac{Re_2}{d_{h2}\,(j_2/f_2)^{1/2}} \tag{6.29}$$

This equation defines a criterion for equivalence of operating points (HESSELGREAVES, 2000). This motivates the definition of the operating parameter, which is an indicator of the operating point:

$$P_o \coloneqq \frac{Re}{d_h\,(j/f)^{1/2}} \tag{6.30}$$

The operating parameter is a reduced flow velocity and it links the overall (thermal and hydraulic) performance requirements to the necessary Reynolds number (HESSELGREAVES, 2000). **Any two surfaces operating under the same thermal and pressure drop requirements must be at the same operating parameter**. In SI units, P_o is given in m^{-1}.

It is important to mention that P_o is only a function of Re, since j and f are functions of Re themselves. Furthermore, j/f is not normally strongly Reynolds number sensitive (HESSELGREAVES, 2000). Therefore, the straightforward interpretation of this function is that the operating Reynolds number is close to directly proportional to the

hydraulic diameter, once the operating conditions and thus the operating parameter are defined.

Manipulating the definition of the operating parameter using the core mass velocity equation (equation 6.19) yields

$$P_o = \frac{1}{\mu}\left(\frac{2\rho\Delta p}{Pr^{2/3}N}\right)^{1/2} \tag{6.31}$$

This shows that the operating parameter is, in fact, a function of the operating conditions Δp and N and fluid properties.

6.2 FACE AREA AND THROUGHFLOW AREA PARAMETERS

Equation 6.24 compares two cross-sectional areas under the same operating conditions or, equivalently, at the same operating parameter. It can be rewriten as

$$\frac{C_{s1}}{\frac{1}{\sigma_1}\left(\frac{f_1}{j_1}\right)^{1/2}} = \frac{C_{s2}}{\frac{1}{\sigma_2}\left(\frac{f_2}{j_2}\right)^{1/2}} \tag{6.32}$$

meaning that the term on either side of the equation is constant, **whenever the operating conditions and thus the operating point are determined**. This means that the denominator on either side of the equation is proportional to the corresponding heat exchanger's total cross-sectional area. Furthermore, it is solely a function of the operating conditions and thus the operating parameter, once the heat transfer geometry is defined. In fact, if the operating parameter remains constant, the cross-sectional area does not change, and so does not each of the denominators. Hence, a good way to compare overall cross-sectional areas is to compare the value of the face area parameter, defined as

$$P_f \coloneqq \frac{1}{\sigma}\left(\frac{f}{j}\right)^{1/2} \tag{6.33}$$

as a function of the operating parameter. Just as mentioned, the cross-sectional area of the heat exchanger is then proportional to the face area parameter. To illustrate its application, consider an arbitrary number of surfaces subjected to the same operating conditions. All of them will operate with the same value of P_o. For all of them, the ratio C_s/P_f will also be the same. Therefore, the overall cross-sectional areas will be all proportional to P_f, which solely a function of P_o.

It is clear that C_s is proportional to P_f. To find the proportionality factor, one uses the definition of porosity and equation 6.18. After some manipulation, one has

$$C_s = \frac{1}{\sigma}\left(\frac{f}{j}\right)^{1/2}\dot{m}\left(\frac{Pr^{2/3}N}{2\rho\Delta p}\right)^{1/2} \tag{6.34}$$

which allows one to write

$$P_f = \frac{1}{\sigma}\left(\frac{f}{j}\right)^{1/2} = \frac{C_s}{\dot{m}\left(\frac{Pr^{2/3}N}{2\rho\Delta p}\right)^{1/2}} \tag{6.35}$$

The last equation shows that, in fact, P_f is simply the cross-sectional area of the heat exchanger divided by a function of operating conditions. Equation 6.35 can be rewritten as

$$C_s = \dot{m}\left(\frac{Pr^{2/3}N}{2\rho\Delta p}\right)^{1/2} P_f$$

which shows that the overall cross-sectional area is proportional to the mass flow rate $\dot{m}$, which is expected, and is also proportional to a function of operating conditions. It is worth mentioning that the proportionality factor C_s/P_f is also a function of the operating conditions.

The face area parameter involves knowing the stream's porosity, which, as previously explained, does not depend exclusively on the considered surface's characteristics. In this sense, an analogous area parameter can be defined based solely on the throughflow area of a stream. This can be done by performing a similar development using equation 6.23. Alternatively, all members of equation 6.35 can be multiplied by the porosity. Either way, the *throughflow area parameter* can then be defined as:

$$P_A \coloneqq \left(\frac{f}{j}\right)^{1/2} \tag{6.36}$$

Similarly, A_c can be written as a function of P_A. Recognizing that $A_c = \sigma C_s$ and using equation 6.34, one gets

$$A_c = \sigma C_s = \left(\frac{f}{j}\right)^{1/2} \dot{m}\left(\frac{Pr^{2/3}N}{2\rho\Delta p}\right)^{1/2} \tag{6.37}$$

Thus, P_A is the throughflow area divided by a function of operating conditions:

$$P_A = \frac{A_c}{\dot{m}\left(\frac{Pr^{2/3}N}{2\rho\Delta p}\right)^{1/2}} \tag{6.38}$$

Since, when comparing surfaces, the operating conditions are the same, the cross-sectional flow areas can be directly compared by comparing the values of P_A.

The throughflow area parameter is defined as the inverse of the square root of the area goodness factor. Thus, greater values of area goodness factor imply smaller values of throughflow area parameter and hence of the throughflow area itself.

The throughflow area parameter is useful when directly comparing two heat transfer surfaces, without regarding the actual dimensions of the completely designed heat exchanger. The face area parameter, such as defined in equation 6.33, is a function of the porosity σ. To determine the porosity, the heat exchanger core must be completely designed, which is frequently not the case when analyzing heat exchanger surfaces, especially in early design stages.

Again, the throughflow area parameter is unique once the operating conditions and thus the operating parameter are defined.

It is worth mentioning, though, that caution must be taken when using the throughflow area parameter. Although the actual porosity can only be determined once the heat exchanger core is designed, some types of surfaces, because of geometrical reasons, impose an upper limit to the achievable porosity. If, for instance, prismatic channels with square cross-sections are considered, the separation walls can be designed as thin as desired by the engineer, so there is no geometrical constraint making it impossible for the porosity to be set as close to 1 as wished for. If, however, circular channels are used, porosity will be limited to a maximum value, which corresponds to the limit case where channels are tangent to each other. Even in this case, there will be solid material in the core. When considering different heat transfer surfaces, it is useful to use the face area parameter with the maximum possible value for the porosity, so a more realistic comparison can be made.

6.3 VOLUME AND FLUID VOLUME PARAMETERS

In a similar way, equation 6.25 can be rewritten as

$$\frac{V_1}{\frac{d_{h1}}{\sigma_1}\left(\frac{f_1}{j_1^3}\right)^{1/2}} = \frac{V_2}{\frac{d_{h2}}{\sigma_2}\left(\frac{f_2}{j_2^3}\right)^{1/2}}$$

Again, the therms on each side of the last equation are constant for the same operating conditions and thus the same operating parameter for any two surfaces being compared. This enables the definition of the volume parameter

$$P_v := \frac{d_h}{\sigma}\left(\frac{f}{j^3}\right)^{1/2} \tag{6.39}$$

which is proportional to the heat exchanger's overall volume. Therefore, P_v links the total volume V of the heat exchanger to its operating conditions. In fact, writing $V = C_s L$ and using equations 6.14 and 6.34, one has

$$V = \frac{d_h}{\sigma}\left(\frac{f}{j^3}\right)^{1/2} \frac{\dot{m} Pr N^{3/2}}{4\left(2\rho\Delta p\right)^{1/2}}$$

hence,

$$P_v = \frac{V}{\dot{m}\dfrac{PrN^{3/2}}{4\left(2\rho\Delta p\right)^{1/2}}} \tag{6.40}$$

Similarly, the volume parameter is the total volume divided by a function of operating conditions. Again, any number of heat transfer surfaces subjected to the same thermal and pressure drop requirements will operate with the same value of P_o. For all of them, the ratio V/P_v will be the same, so the resulting heat exchanger's volumes will be proportional to the respective values of P_v.

In an analogous way, if one only considers the fluid volume of the stream, the fluid volume parameter can be defined:

$$P_{fv} \coloneqq d_h \left(\frac{f}{j^3}\right)^{1/2} \tag{6.41}$$

Considering only the fluid volume in the analysis is useful when directly comparing two different heat transfer surfaces, without any concern regarding the actual dimensions of the heat exchanger. This is analogous to using the throughflow area parameter for direct comparison of flow areas, such as explained in the previous section. Naturally, the volume parameter, such as defined in equation 6.39, is a function of the porosity σ, which depends on the heat exchanger's dimensions. When the surface geometry imposes an upper limit for the porosity, it is recommended to use its maximum theoretical value and then determine the volume parameter.

7 RESULTS

The newly developed heat exchanger has been experimentally tested, so new thermal and hydraulic correlations could be developed for the pin-fin geometry. This chapter is dedicated to the presentation of results, as well as the inherent discussion.

7.1 EXPERIMENTAL HEAT TRANSFER RATE

The first results usually calculated based on experimental data correspond the heat transfer rates. As already mentioned, they can be determined based on energy balances, on either stream, for every test. Figure 61 shows the experimental heat transfer rates based on energy balances of both streams for the test battery where the targeted hot stream inlet temperature was 70°C and the targeted mass flow rate was $0,1\text{kg/s}$. Results for the other five test batteries are presented in appendix C.

The figure shows good agreement between the calculated data based on both streams. This indicates that heat transfer to the outer environment is negligible, given that otherwise higher heat transfer rates of the hot stream would be found. This can be observed in all test batteries (see appendix C). One can also notice a clear tendency where the heat transfer rate rises as the cold stream mass flow rate increases.

Results of all test batteries can be seen in Figure 62. The figure shows that the heat

Figure 61 – Heat transfer rate. Hot stream inlet temperature at 70°C and mass flow at $0,1\text{kg/s}$.

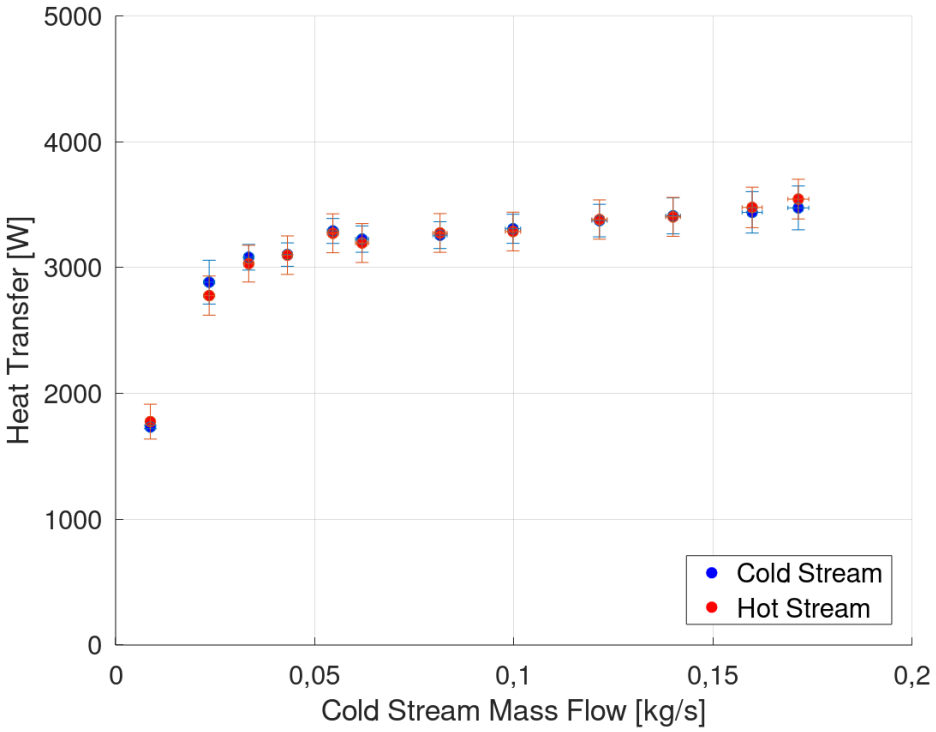

Figure 62 – Heat transfer rates of all test batteries.

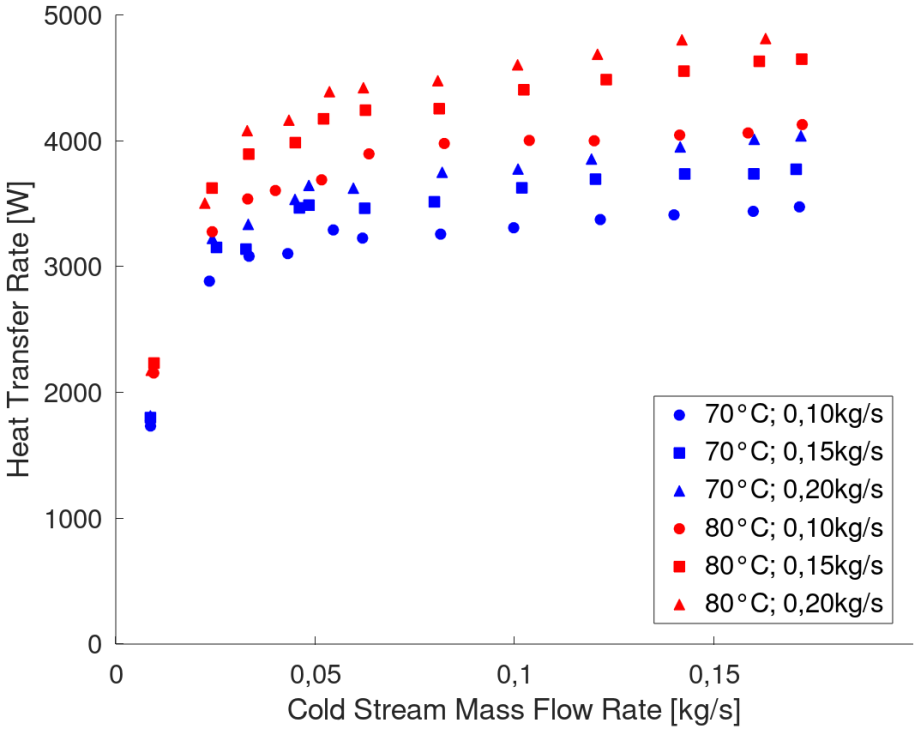

transfer rate rises as both mass flow rates increase and as the hot stream inlet temperature rises as well. This figure also does not bring uncertainty ranges of the calculated values, as this would excessively pollute the image. The uncertainty ranges are presented in the figures bringing the results of individual test batteries. One of these figures was previously introduced in this section, whereas the other ones, just as mentioned, are presented in appendix C.

7.2 THERMAL CONDUCTANCE

As the heat transfer rate depends strongly on the inlet temperatures, caution is needed when directly comparing the results. The thermal conductance, however, is the inverse of the overall thermal resistance. It is, in this sense, only a weak function of the inlet temperatures, which arises solely from the fact that thermophysical properties are functions of temperature. Thermal conductance, therefore, represents the heat exchanger's performance being only marginally affected by inlet temperatures. Actually, convection and conduction phenomena determine its value. Hence, thermal conductance has a deeper physical meaning regarding heat exchanger performance, being only weakly influenced by inlet temperatures and more strongly represented by the physical phenomena that occur inside the heat exchanger. It is a strong function of the Reynolds numbers of both streams. It is thus safe to say that the overall thermal conductance has a physically deeper meaning concerning heat exchanger performance. Figure 63 shows the experimental

Figure 63 – Thermal conductance. Hot stream inlet temperature at 70°C and mass flow at 0, 1kg/s.

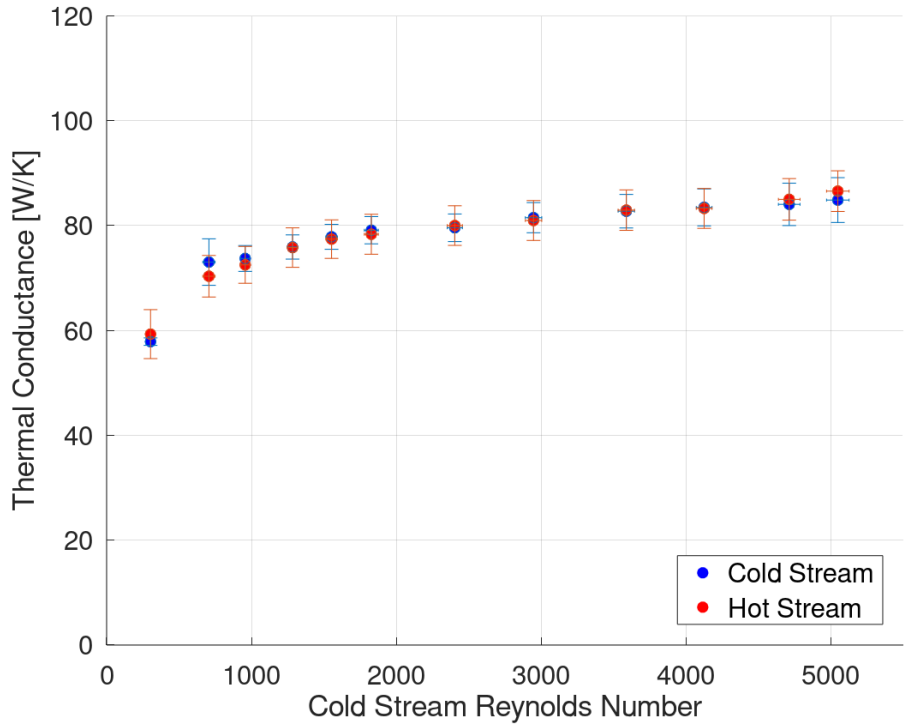

thermal conductance based on measurements from both streams. The same test battery of Figure 61 was considered.

The data show a monotonic increase in thermal conductance as the cold stream Reynolds number rises. This is expected, since increasing the Reynolds number increases the Nusselt number, which makes the corresponding convective resistance to diminish.

Results of all test batteries can be seen in Figure 64. It is worth to compare figures 62 and 64. Test batteries with the same targeted values of the hot stream mass flow rate are represented by the same symbol, whereas test batteries with the same targeted hot stream inlet temperature are represented by symbols of the same color. Test batteries with the same targeted mass flow rates present similar values of thermal conductance, regardless of the targeted hot stream inlet temperature. Therefore, the higher temperature difference in half the test batteries did not create any appreciable difference in the values of thermal conductance, just as they did for the heat transfer rate. Thus, one can conclude that the thermal conductance does not present a strong dependency on the mean temperature difference between both streams. Therefore, thermal conductance is, indeed, a good way to remove the effect of varying inlet temperatures between tests from the analysis and focus only the heat exchanger's performance.

The data show that all test batteries present the same monotonic increase in thermal conductance as the cold stream Reynolds number increases. Similarly, higher hot stream Reynolds numbers also make the thermal conductance rise, as can be verified by

Figure 64 – Thermal conductance of all test batteries.

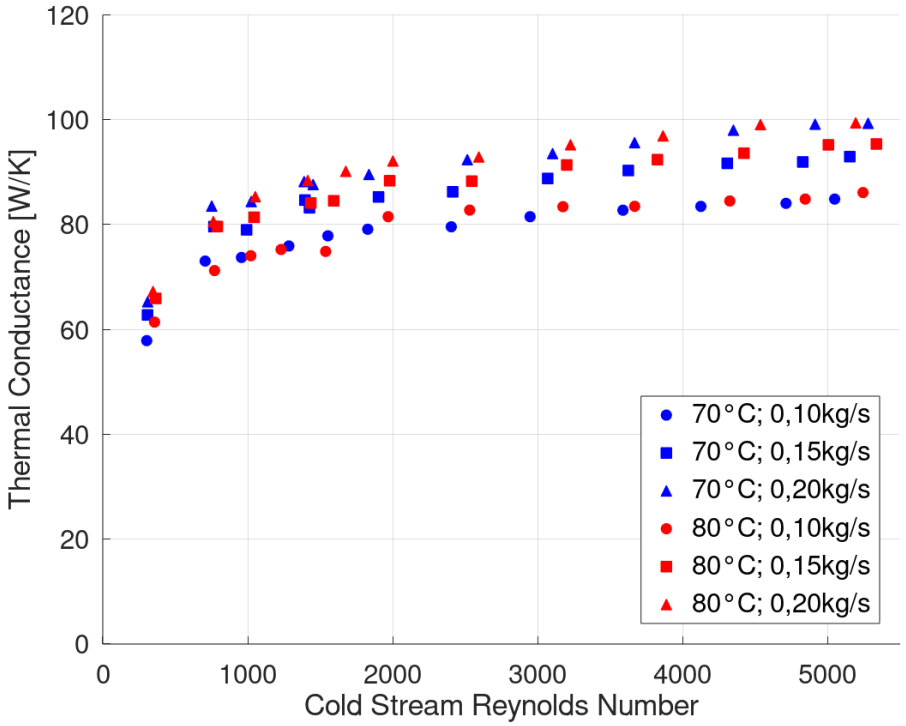

comparing test batteries.

It is possible to recognize from the data that even expressive variations of Reynolds numbers of both streams are not able to create big variations of thermal conductance. As already stated before, the thermal conductance can be expressed as

$$UA = (R_c + R_w + R_h)^{-1} \tag{7.1}$$

where R_c is the cold side convective resistance, R_w is the wall resistance and R_h is the hot side convective resistance. This yields

$$\frac{\partial UA}{\partial R_c} = \frac{\partial UA}{\partial R_w} = \frac{\partial UA}{\partial R_h} = -(R_c + R_w + R_h)^{-2} = -(UA)^2 \tag{7.2}$$

However,

$$\frac{\partial R_c}{\partial \hbar_c} \approx -\frac{1}{(\eta_o A)_c}\frac{1}{\hbar_c^2} = -\frac{1}{(\eta_o \hbar A)_c}\frac{1}{\hbar_c} = -\frac{R_c}{\hbar_c} \tag{7.3}$$

This is an approximate result, since η_o is a function of the convective coefficient. This yields

$$\frac{\partial UA}{\partial \hbar_c} = \frac{\partial UA}{\partial R_c}\frac{\partial R_c}{\partial \hbar_c} \approx (UA)^2 \frac{R_c}{\hbar_c} \tag{7.4}$$

Similarly, for the hot stream,

$$\frac{\partial UA}{\partial \hbar_h} = \frac{\partial UA}{\partial R_h}\frac{\partial R_h}{\partial \hbar_h} \approx (UA)^2 \frac{R_h}{\hbar_h} \tag{7.5}$$

Any relative variation in a stream's Reynolds number creates a relative variation in the corresponding Nusselt number, and thus in the convective coefficient, in the same

order of magnitude. Figure 64 shows that despite the hot stream mass flow doubling its value from $0,1\text{kg/s}$ to $0,2\text{kg/s}$, and therefore creating a corresponding relative increase in Reynolds number, no appreciable increase in thermal conductance is observed. The same is true for the cold stream. Comparing results for the cold stream Reynolds number at around 1000 and around 5000 shows a comparably small relative increase in thermal conductance as well. We can conclude that

$$\frac{\Delta UA/\left(UA\right)}{\Delta\hbar_c/\hbar_c} \ll 1 \tag{7.6}$$

which can be rewritten as

$$\frac{\Delta UA}{\Delta\hbar_c}\frac{\hbar_c}{UA} \ll 1 \tag{7.7}$$

Taking the limit where $\Delta\hbar_c \to 0$, one has

$$\frac{\partial UA}{\partial\hbar_c}\frac{\hbar_c}{UA} \ll 1 \tag{7.8}$$

yielding

$$UAR_c \ll 1 \tag{7.9}$$

Therefore, one finds that

$$\frac{R_c + R_w + R_h}{R_c} \gg 1 \tag{7.10}$$

An analogous result is valid for the hot stream. One has

$$\frac{R_c + R_w + R_h}{R_h} \gg 1 \tag{7.11}$$

This shows that the conduction resistance is the highest one in the heat exchanger, which could have been directly concluded from Figure 64, simply by recognizing that the important relative variations in the convective resistances due to expressive changes in Reynolds numbers did not have an appreciable effect on conductance, meaning that the big variations in the convective resistances did not play an important role in the overall thermal resistance. This could only mean that the dominating resistance is the one related to wall conduction for the given operating conditions.

7.3 COLBURN FACTOR

According to the model previously presented in section 5.3, the cold stream convective coefficient was calculated. Then, equation 6.9 was used to calculate the Colburn factor. Results are presented as a function of the Reynolds number and a correlation is found by the least-squares method. This can be seen in Figure 65. The correlation is

$$j = 1,0887Re^{-0,58421} \tag{7.12}$$

The minimum Reynolds number of all experimental tests is 303, whereas the maximum one is 5477.

It can be seen that, just as mentioned by Hesselgreaves (2000), the Colburn factor decreases as the Reynolds number rises.

Figure 65 – Colburn factor.

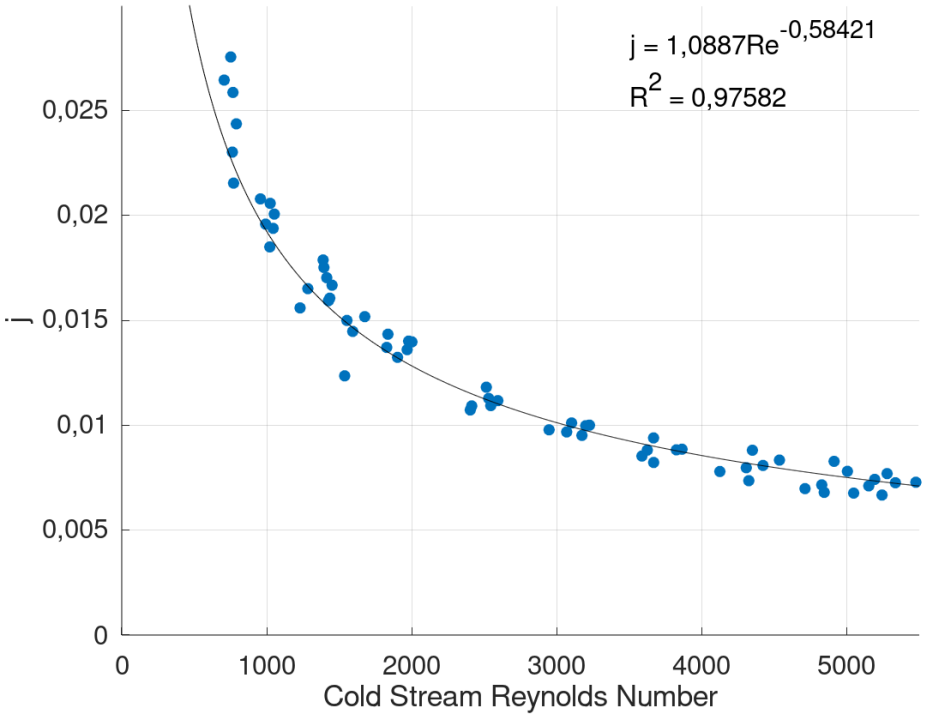

7.4 HEAD LOSS

As previously explained, the pressure drop inside a heat exchanger is proportional to the pumping power. Hence, it is an essential parameter to be used in heat exchanger design. For every test battery, the total experimental pressure drop can be presented as a function of the mass flow rate, such as in Figure 66. It is emphasized here that the values shown in this figure represent the total measured core pressure drops, including core inlet and outlet effects. Results of all test batteries can be seen in Figure 67.

The core inlet and outlet effects are calculated based on the modelling presented in section 5.4, so the pressure drop related only to the heat transfer surface can be obtained. The results are then non-dimensionalized in the form of the friction factor. Non-dimensional results are only presented for $Re \geq 2000$, otherwise the high relative uncertainties of the pressure drop data will provide inaccurate results. Implementation of the least squares method provided the following correlation:

$$f = 0,9581 Re^{-0,1097} \tag{7.13}$$

Results can be seen in Figure 68, which shows the experimental values, highlights the mean value of experimental observations, and also shows the adjusted function. One can see that the friction factor is relatively constant throughout the Reynolds number domain, which translates into pressure drop being proportional to the square of the mean flow velocity. Model implementation shows that inlet and outlet effects account for, on

Figure 66 – Total cold stream pressure drop. Hot stream inlet temperature at 70°C and mass flow at $0,1$kg/s.

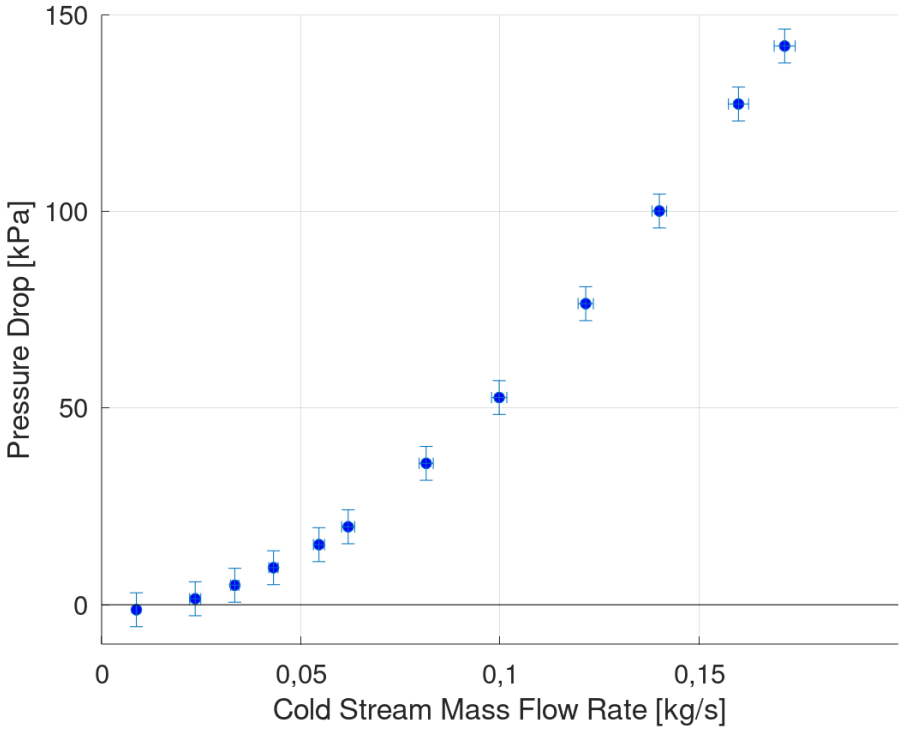

Figure 67 – Experimental cold stream pressure drop.

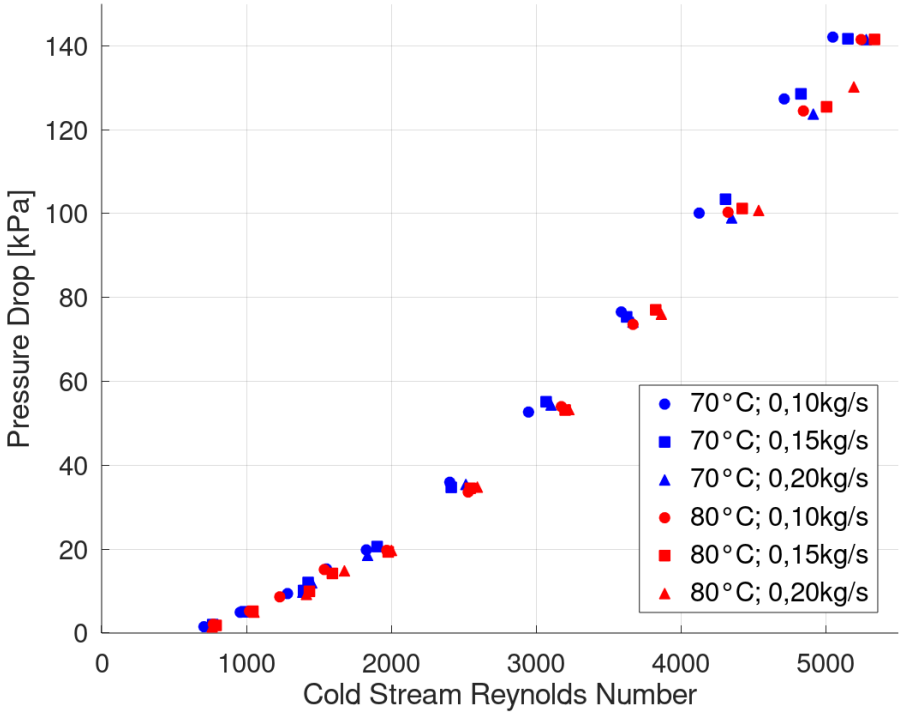

Figure 68 – Friction factor.

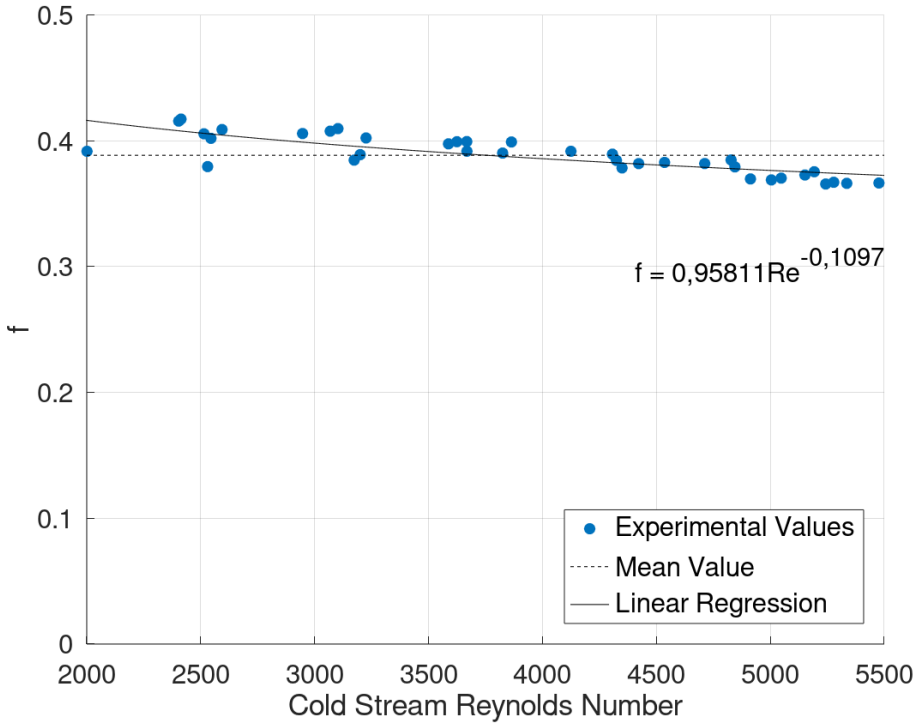

average, 0,91% of the total pressure drop.

7.5 PERFORMANCE PARAMETERS

This section is dedicated to the performance evaluation of the pin-fin geometry tested in the development of this work. Two benchmark heat transfer surfaces will be considered for comparison purposes. The first one consists of square cross-sectional prismatic channels with a side length of 3mm. This corresponds to the design of the prototype's hot stream channels. The Colebrook equation is used to provide the Darcy friction factor, whereas Gnielinski's correlation is used for the Nusselt number.

The second benchmark geometry consists of zigzag channels with a fin angle of 52°, just as the one studied by Ngo et al. (2007). In order to have the same channel height of 3mm, the entire geometry was scaled up. The original channels present a fin gap of $1,31$mm and a fin depth (equivalent to channel height) of $0,94$mm. Thus, the scaling factor is $3/0,94$, so the resulting channel height is 3mm whereas the resulting channel gap is $4,18$mm. The zigzag geometry is shown in figure 1.

7.5.1 Area Goodness Factor

Before analyzing the new pin-fin geometry using the performance parameters presented in chapter 6, it is worth analyzing the area goodness factor based on the results of the previous two sections. Figure 69 shows the area goodness factor as a function of the

Figure 69 – Area goodness factor.

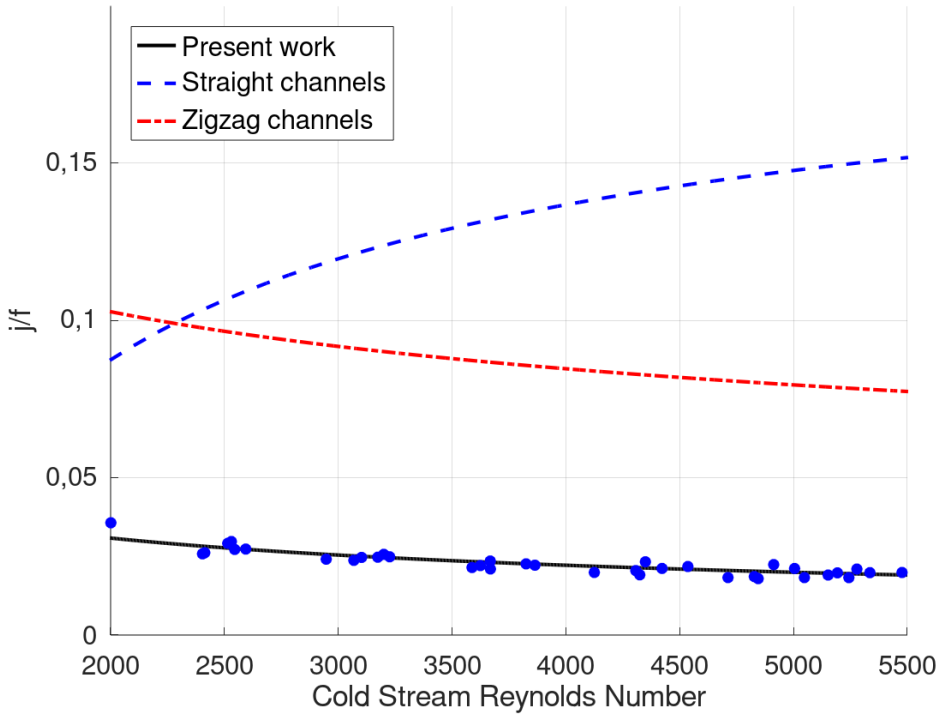

Reynolds number. As previously pointed out, performance parameters should be compared on a same operating parameter basis. Therefore, the results presented in this figure should not be used for direct comparison of heat transfer surfaces. It is useful, however, to analyze the behavior of area goodness factor as a function of the Reynolds number.

As can be seen in the definitions of the area and volume parameters, heat exchangers get more compact as j/f increases. This means that higher values of area goodness factor are desired when developing a compact heat exchanger. Although these parameters will be analyzed in detail in the following sections, one can expect the pin-fin geometry to perform better at lower Reynolds numbers.

7.5.2 Operating Parameter

The operating parameter can be determined based on the Reynolds number, the hydraulic diameter and the area goodness factor. The results are shown in figures 70 and 71. It is possible to see that the operating parameter of the pin-fin surface is greater than that of both benchmark geometries for the same Reynolds number.

To illustrate what this means, consider all three heat transfer surfaces were to be used in the same application, and were therefore subjected to the same thermal and hydraulic requirements[1]. This means that all surfaces would have to operate with the same operating parameter, such as explained in chapter 6. If P_o is the same for all surfaces,

[1] This means that the Number of Transfer Units (NTU), the mass flow ($\dot{m}$) and the pressure drop (Δp) are the same for both surfaces.

Figure 70 – Operating parameter.

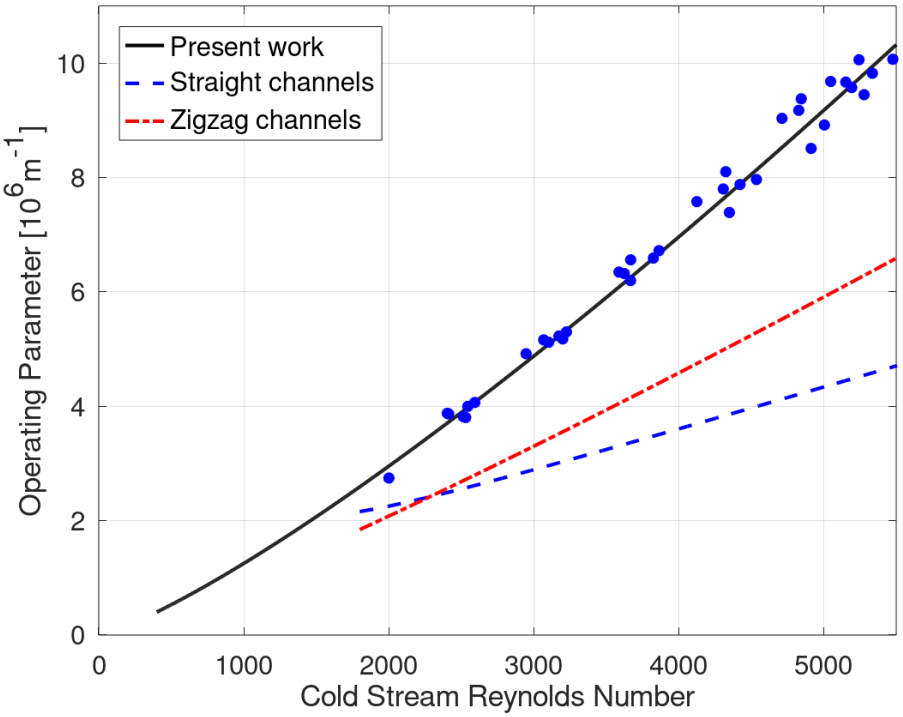

Figure 71 – Operating parameter.

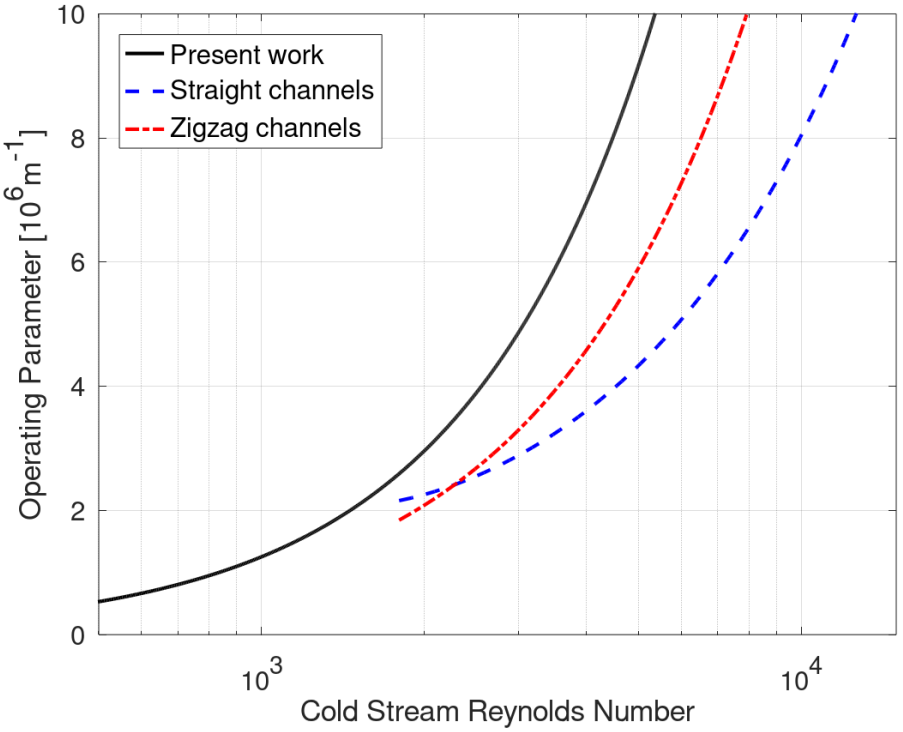

the results show that the square cross-sectional channels must operate at a much higher Reynolds number than both other geometries. The zigzag channels would operate with an intermediate Reynolds number for most part of the plotted domain.

To further illustrate this, one can consider, at first, subjecting a specific heat transfer surfaces with a certain geometry to specific values of mass flow rate and pressure drop. In order to respect the pressure drop constraint, one can either vary flow length or flow velocity until the correct value of Δp is met[2]. Since the mass flow rate is fixed, the only way to vary the flow velocity without varying fluid properties is to change the cross-sectional area. Therefore, two geometric variables appear: flow length and cross-sectional area. Mathematically, this is expressed as

$$\Delta p = \Delta p(L, A_c) \tag{7.14}$$

It is important to notice that the hydraulic diameter is fixed once the surface geometry is selected, so the cross-sectional area can only be increased by replicating the geometric pattern perpendicularly to flow length. This can be done by adding layers of channels or increasing the number of channels per layer in a heat exchanger. Likewise, the opposite can be done if the cross-sectional area were to be reduced.

Both independent variables of equation 7.14 are coupled by the pressure drop constraint. Therefore, this creates a problem with one degree of freedom. The thermal constraint, i.e. the prescription of the Number of Transfer Units, is the final condition that indicates the only possible solution.

It is useful to graphically represent this problem by plotting the pressure drop as a function of both independent variables, creating a three-dimensional surface. This yields the surface shown in figure 72. The pressure drop increases linearly as flow length increases. When form drag is the most important contribution to pressure drop, Δp is essentially proportional to the square of the mean flow velocity, which, in turn, is inversely proportional to the mean cross-sectional area. It is important to mention that the goal here is to convey the theory behind the graphic assessment of the problem. However, for figure plotting, the pin-fin geometry was considered, so equations 7.12 and 7.13 were used alongside equation 6.16.

Prescribing the pressure drop corresponds to constraining the solution to a plane at a constant Δp. Therefore, all possible solutions will be at the intersection of that plane and the surface given by equation 7.14. For the arbitrary case of prescribing $\Delta p = 40\text{kPa}$, the intersection is shown as a thicker curve in the figure.

The only possible solution is at the intersection of the constant pressure drop curve with the appropriate curve of constant N. Points closer to the origin correspond to heat exchangers with both less cross-sectional area and flow length. Thus, such solutions provide a low Number of Transfer Units. On the other hand, solutions far away from the

[2] see equation 6.16.

Figure 72 – Pressure drop as a function of A_c and L.

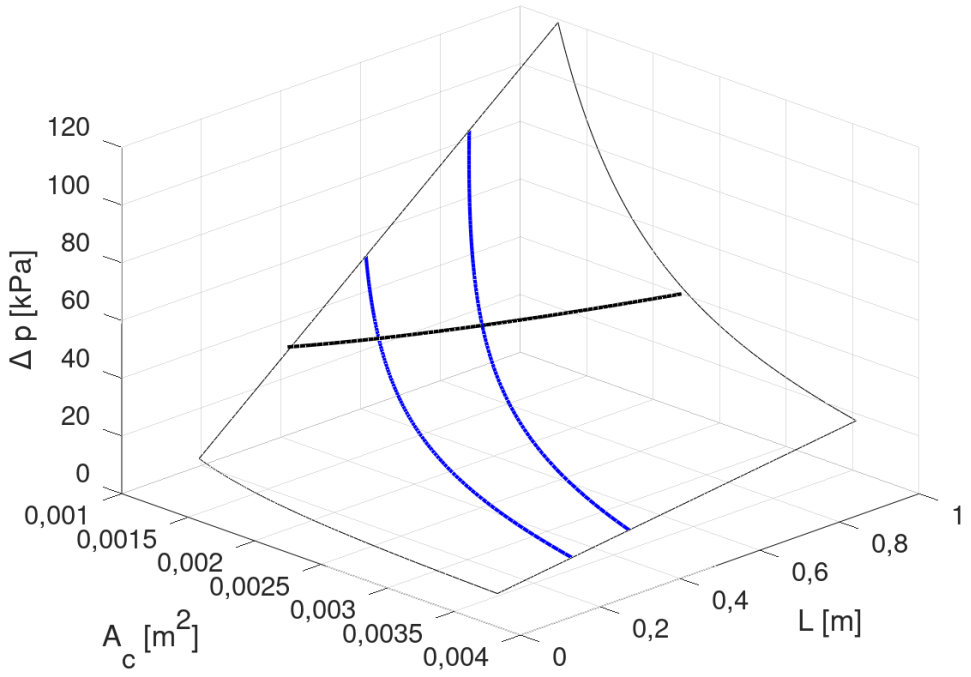

origin provide a higher Number of Transfer Units. Two curves with constant values of N are shown in blue in figure 72.

To find the curves of constant N, one can substitute equation 6.9 in equation 6.12, which yields

$$N = \dot{m}\frac{kPr^{1/3}}{\mu}\frac{j}{A_c}\frac{A_s}{C} \tag{7.15}$$

Assuming that the total heat transfer area A_s is proportional to flow length, one can write

$$P' = \frac{A_s}{L} \tag{7.16}$$

For prismatic channels, P' corresponds to the perimeter of the flow cross-sectional area. For non-prismatic channels, A_s may not increase linearly with L. In fact, for the pin-fin geometry, whenever a new set of pin fins is added, the upstream and downstream faces of the fins (which are perpendicular to the main flow direction) make the total heat transfer area to suddenly increase in a non continuous way. Considering, however, a large number of fin rows, one can assume that the real function $A_s(L)$ can be approximated by a straight line, just as given in the last equation. Since the hydraulic diameter is kept constant P' is proportional to A_c. Therefore, one can write

$$P' = \Omega A_c \tag{7.17}$$

where Ω is a proportionality factor.

Assuming that the Colburn factor can be expressed as $j = \alpha Re^{\beta}$, one has

$$N = \left(\frac{k}{\mu c_p}\right)^{2/3} \alpha \left(\frac{\dot{m} d_h}{\mu}\right)^{\beta} \Omega \frac{L}{A_c^{\beta}} \tag{7.18}$$

For each geometry considered by the designer, a surface can be plotted. The pressure drop constraint defines, for each surface, a curve on the surface. The thermal requirement determines another curve on the surface. The solution would be at the intersection of both curves. Thus, for every heat transfer surface, the flow length and flow are will be known. These parameters can then be compared to determine the best suited geometry.

There is, in fact, a more practical way to compare geometries, by using the formerly introduced performance parameters. The following sections will present the solution to this problem, considering all benchmark surfaces, in the form of area and volume parameters as functions of the operating parameter.

7.5.3 Face area and throughflow area parameters

As previously explained, for two surfaces to be compared under the same thermal and hydraulic requirements, they must operate with the same operating parameter. The Throughflow area parameter is a function of the operating parameter. At this point, equation 6.38 comes in handy:

$$P_A = \frac{A_c}{\dot{m}\left(\frac{Pr^{2/3} N}{2\rho\Delta p}\right)^{1/2}}$$

This shows that the throughflow area parameter is the throughflow area divided by a function of operating conditions, such as explained in section 6.2. Since the denominator only depends on the operating constraints, it will be the same when comparing different surfaces for the same application, the cross-sectional flow area of different surface geometries can be directly compared by comparing the values of P_A.

Figure 73 shows the throughflow area parameter as a function of the operating parameter. It is possible to see that the pin-fin geometry requires a higher cross-sectional area for fluid flow. This is related to the fact that, for the same operating parameter, the pin-fin Reynolds number is lower than the benchmark value.

The only difference between the face area and throughflow area parameters is that while the former considers the actual cross-section of the entire heat exchanger, the latter only considers the cross-sectional flow area. This arises by the presence of the porosity σ in equation 6.33. The actual dimensions of a heat exchanger depend on multiple requirements, such as structural demands, manufacturing costs, transportation issues, header development and placement etc. Therefore, when considering purely convective performance of heat transfer surfaces, without accounting for the specific characteristics

Figure 73 – Throughflow area parameter.

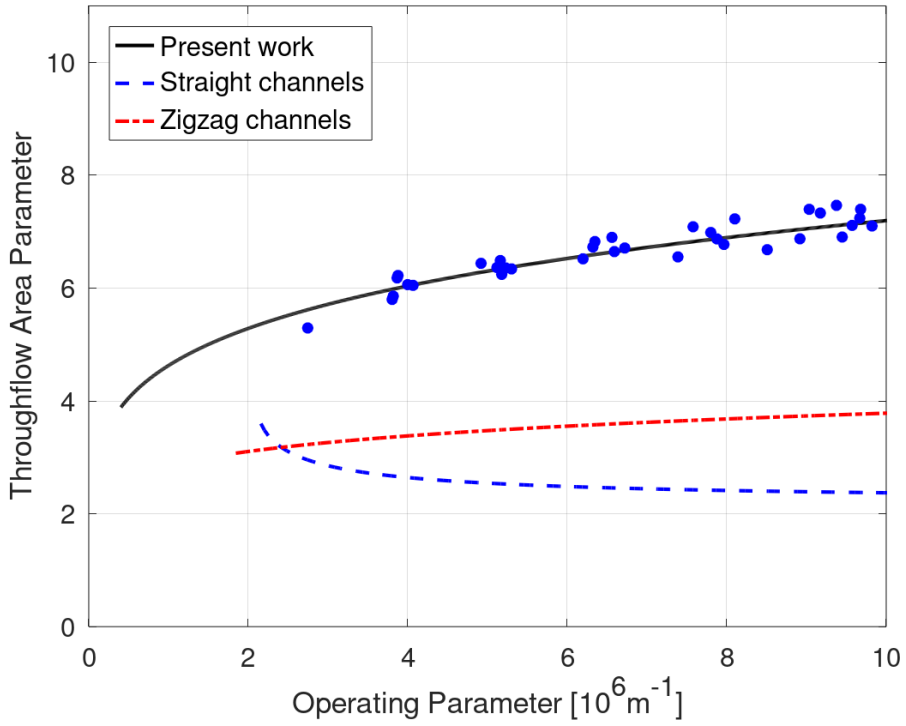

concerning heat exchanging design, the use of the throughflow area parameter is tempting. However, pure geometrical aspects of heat transfer surfaces provide different limitations to increase porosity.

Prismatic channels with square cross-section do not present any limitation to porosity. Geometrically, the distance between channels can be made as little as desired, so porosity can be set as close to 1 as desired. The same is true for zigzag channels. When considering the pin-fin geometry, however, that is not the case. Even if flow layers can be as close to each other as desired, the mere existence of fins sets an upper limit for the porosity. The maximum possible porosity of the pin-fin geometry is given by:

$$\sigma_{max} = \frac{V_{s,max}}{V} \tag{7.19}$$

where $V_{s,max}$ is the maximum enclosed fluid volume. The maximum enclosed volume condition corresponds to the minimal solid material condition, which arises when the separation walls are negligibly thin. Analyzing figure 22 allows one to find $\sigma_{max} = 3/4$. Results for the face area parameter are shown in figure 74. Comparing results allows one to see that the pin-fin geometry is limited as for the highest achievable compactness, provided that the porosity cannot be set as high as in the case where the benchmark geometries are used.

Figure 74 – Face area parameter for maximum porosity.

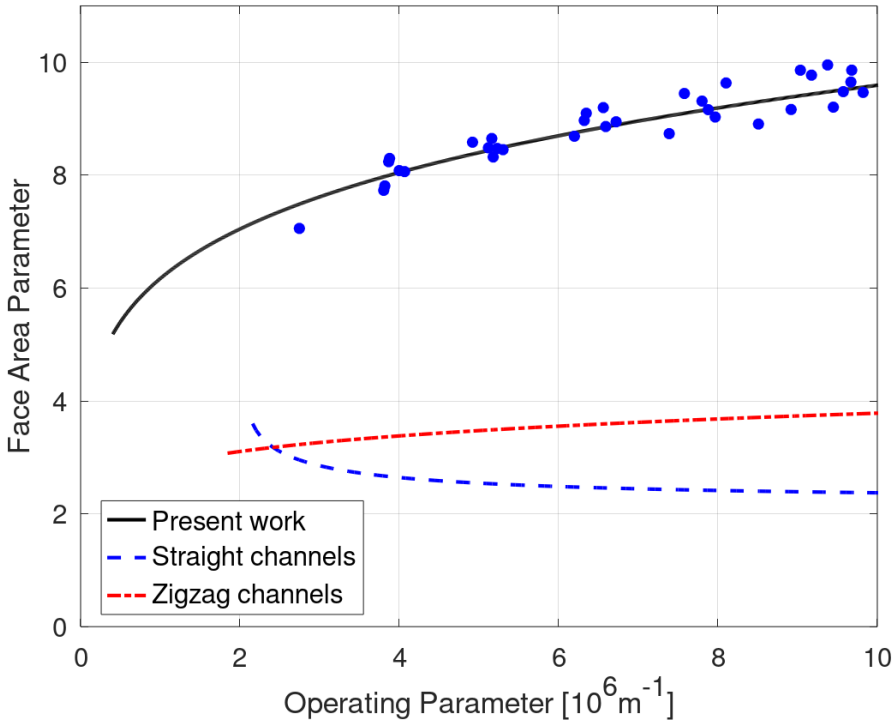

7.5.4 Volume parameter

As previously explained in section 6.3, the volume parameter is the total volume divided by a function of operating conditions. This can be seen based on equation 6.40:

$$P_v = \frac{V}{\dot{m}\dfrac{PrN^{3/2}}{4\left(2\rho\Delta p\right)^{1/2}}}$$

Similarly, when comparing heat transfer surfaces for the same application, the denominator will be the same for both of them, so the volume parameter allows a direct comparison of heat exchanger volume to be made between both surfaces.

The volume parameter also depends on the porosity, since it accounts for the entire volume of the heat exchanger. To directly compare two different heat transfer surfaces without any concern about the specific application, the same strategies used in the previous section can be implemented. First, the fluid volume parameter can be used, so only the fluid volume is considered. Afterwards, the maximum possible porosity can be used for a more reliable comparison.

Figure 75 shows fluid volume parameter as a function of the operating parameter for both surfaces. It is possible to see that, despite presenting a higher cross-sectional flow area, the pin-fin geometry produces a heat exchanger of lower fluid volume. This means that the new geometry requires a much smaller flow length compared to the first benchmark geometry (straight channels). To have the same pressure drop as in straight channels, the

Figure 75 – Fluid volume parameter.

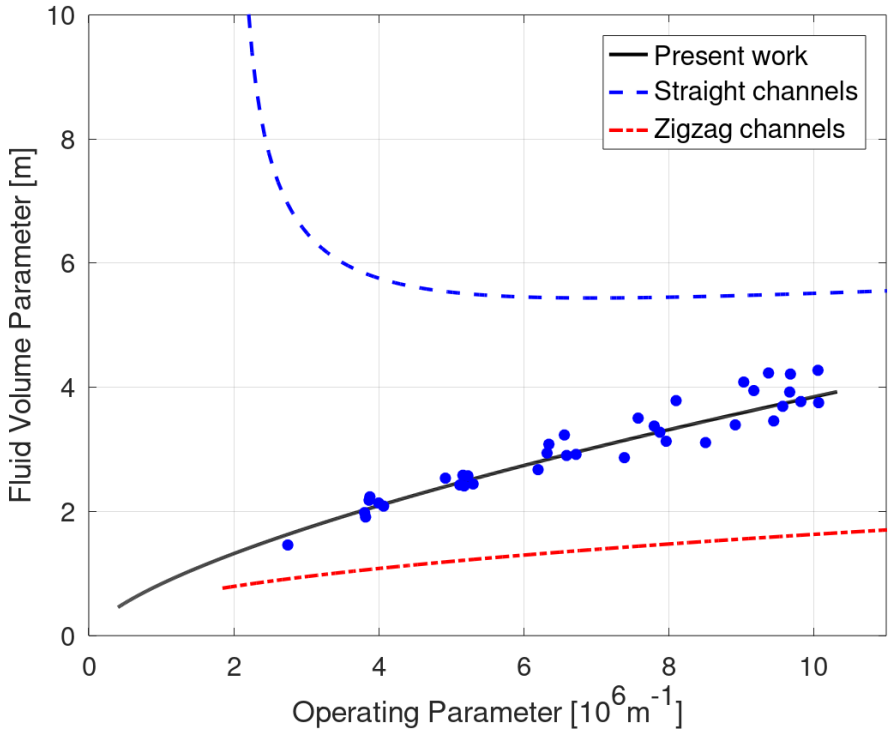

pin-fin geometry must operate with a smaller Reynolds number, which translates into a greater cross-sectional area, such as shown in section 7.5.3, more specifically in figure 73. However, its thermal performance is so high that the flow length is much shorter than the benchmark geometry's flow length. This can be seen based on the fact that even with a larger cross-sectional area, the overall fluid volume is smaller for the pin-fin geometry.

As previously stated based on the observation of figures 70 and 71, the pin-fin geometry operates at a lower Reynolds number than its counterparts, for the same operating conditions. This translates into larger throughflow areas, such as shown in the previous section (the mass flow rate is constrained). On the other hand, the resulting heat exchanger core is so much shorter that the total fluid volume is smaller than that of straight channels. Given that the pin-fin geometry requires larger values of cross-sectional area and creates shorter heat exchangers, one can conclude that, comparably, such geometry tends to create high pressure drops.

Considering now the maximum porosity for both geometries, the volume parameter values of figure 76 are obtained. The results show that the pin-fin geometry provides a much lower overall volume for lower values of operating parameter, which corresponds to lower Reynolds numbers. For higher values of operating parameter, the heat exchanger volume gets closer to that of straight channels. Across all the analyzed domain, the zigzag geometry produces a more compact heat exchanger.

It is important to mention that the values considered for the porosity are merely theoretical and practically not achievable. If, all three geometries, one considers separation

Figure 76 – Volume parameter for maximum porosity.

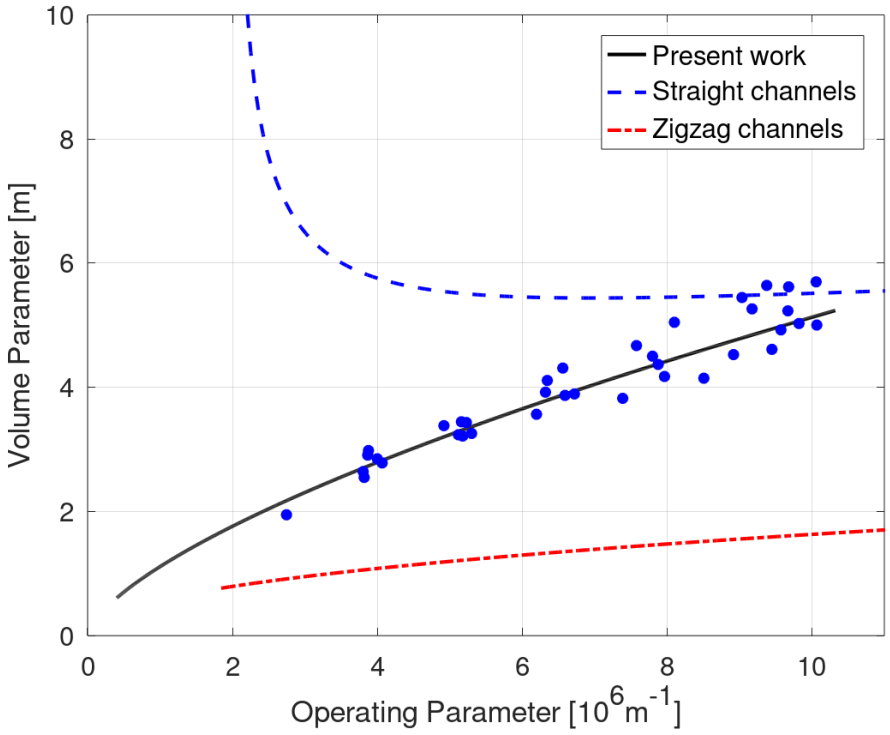

walls with the same thickness, the values of porosity of all heat exchangers will be closer, which will imply in a better relative performance of the pin-fin geometry compared to benchmark ones. The zigzag channels, will, though, still be the best performer.

These results show that, for the same thermal and hydraulic requirements, the pin-fin geometry demands a lower Reynolds number, a larger flow area and a much shorter flow length compared to straight channels with square cross-section. On one hand, the larger flow area is necessary to avoid high pressure drops. On the other hand, the enhanced convection allows the designer to create a much shorter heat exchanger. The volume parameter shows that, in the end, a more compact heat exchanger can be designed using the pin-fin geometry.

The benchmark surface with zigzag channels, in turn, also operates with a lower Reynolds number across the entire analysis domain, when compared to the pin-fin geometry. For most part of the domain, however, it requires a higher Reynolds number than the considered prismatic channels. This implies a smaller throughflow area for this geometry, especially when the porosity limitation is considered. For the small part of the domain where the zigzag channels operate at a lower Reynolds number than the square cross-sectional channels, the zigzag channels have smaller throughflow area and face area parameters.

When it comes to volume, zigzag channels are the best performer, presenting lower values of both fluid volume and volume parameters.

8 CONCLUSION

The present monograph encompasses all phases from designing, to testing and analyzing a new conception of compact heat exchanger. Here, the most relevant conceptual aspects concerning the development of a compact, diffusion bonded heat exchanger core with pin-fin geometry were presented.

The design suggestion of chapter 3 shows how the here presented manufacturing technique can be used to developed heat exchanger cores for practical purposes. Because, however, of the interest in testing the newly developed pin-fin geometry under fouling conditions, a special prototype was built using an adapted manufacturing technique, so a heat exchanger core with only two stream layers could be obtained. Because of the same reason, a new workbench had to be assembled, with two closed water streams, to allow future testing with deposition.

The theoretical modelling presented in chapter 5 was used to obtain experimental correlations for the Colburn factor and the friction factor. It is important to mention that the prototype's pin-fin geometry is different from that of all pin-fin surfaces presented in the chapter 2. This means that none of the authors tested this specific geometry, and therefore no previously known correlation was developed considering the present case.

As already explained, within the considered range of Reynolds number, the friction factor is fairly constant and can be approximated by its mean value $\overline{f} = 0,388$. The Colburn factor, however, is given by the correlation given in equation 7.12:

$$j = 1,0887 Re^{-0,58421}$$

A study based on the parameters introduced in chapter 6 showed that the new pin-fin geometry has an intermediate performance when compared to straight and zig-zag channels. The results can be summarized by figures 74 and 75, which are shown side by side in figure 77.

It becomes clear, based on the figures, that to respect the pressure drop constraint, the pin-fin geometry requires a larger flow area, or, equivalently, a lower Reynolds number. This can also be verified by comparing the Reynolds numbers of all surfaces for the same Operating Parameter, such as shown in figure 71. However, the enhanced convection produces a shorter core, which translates into having an overall volume lower than that of the straight channel counterpart. The zig-zag geometry, however, is still the best performer.

Although the prototype was manufactured with a pin-fin geometry such as idealized for the first design, it must be recognized, though, that the prototype was not manufactured using the specifically developed technique, because of the reasons explained in chapter 4. As a suggestion, a new prototype can be manufactured, such as the one presented in chapter 3, in order to completely validate the manufacturing process.

At the same time, further study is necessary to examine the convective behavior of pin-fin surfaces. Considering the particular geometry here presented, one could perform

Figure 77 – (a) Face Area Parameter and (b) Fluid Volme Parameter.

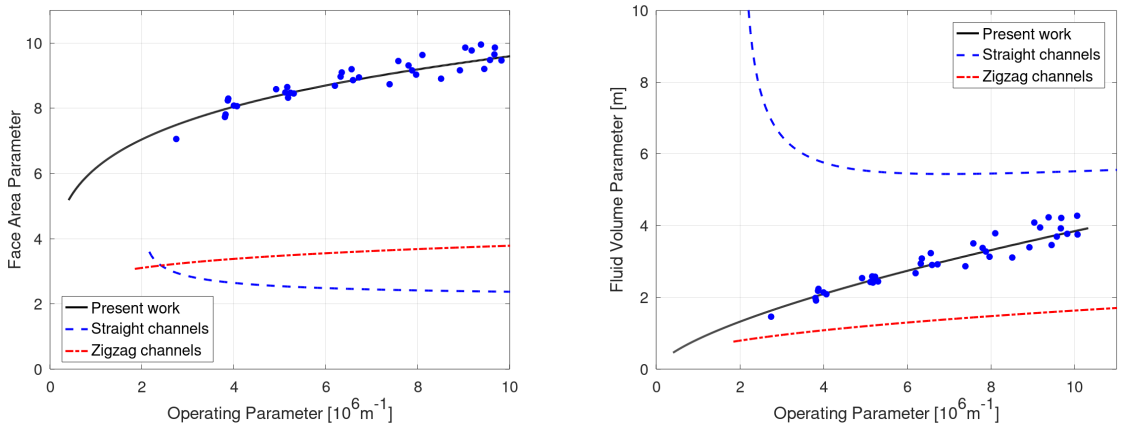

(a) (b)

tests using other fluids, such as air, to increase the convective resistances of both streams. When one of the three resistances is dominant (in the present case, the wall resistance), any uncertainty concerning its calculation will create big relative uncertainties in the calculation of the other resistances, which affects the quality of the resulting correlation. By using air instead of water, the wall resistance would no longer be the dominant one, meaning that the convective coefficient of the pin-fin surface could be obtained with higher accuracy. Furthermore, testing the geometry with fluids with different Prandtl numbers also allows one to obtain a correlation with a larger applicability.

Another suggestion is to test the pin-fin geometry under high-fouling conditions. This comes in second place because knowing the surface's convective behavior is important to support the development of fouling-related studies.

At last, it must be said that this work intends to add new knowledge to the field of heat transfer, specially considering heat exchangers. Given the vast use of such equipment, it is important for the designer to have as many tools as possible to develop more efficient and better suited solutions for any given application. In this sense, this work presents not only a constructive alternative to manufacture heat exchangers, but also highlights a way to compare heat transfer surface geometries. Thus, this author hopes this text becomes a useful tool for designers in the field of thermal engineering.

REFERENCES

BATISTA, J. V.C. **MODELAGEM E ANÁLISE EXPERIMENTAL DE UM TROCADOR DE CALOR COMPACTO DE CANAIS EM ZIGUE-ZAGUE**. [S.l.: s.n.], 2017.

BIPM. **International vocabulary of metrology – Basic and general concepts and associated terms (VIM)**. [S.l.: s.n.], 2012. Disponível em: https://www.bipm.org/utils/common/documents/jcgm/JCGM_200_2012.pdf..

CARQUEJA, Guilherme Grando. **Modelagem e Análise Experimental de Trocador de Calor Compacto com canais de Perfil Quadrado**. [S.l.: s.n.], 2017.

CARVALHO DOS SANTOS, Mauricio et al. **PROCESSO PARA FABRICAÇÃO DE UM NÚCLEO DE UM TROCADOR DE CALOR**. [S.l.: s.n.], 2016.

ÇENGEL, Yunus A; GHAJAR, A J. **Transferência de Calor e Massa: uma Abordagem Prática**. [S.l.]: McGraw-Hill Education, 2014.

CHURCHILL, Stuart W. Comprehensive Correlating Equations for Heat, Mass and Momentum Transfer in Fully Developed Flow in Smooth Tubes. **Industrial and Engineering Chemistry Fundamentals**, 1977. ISSN 01964313. DOI: 10.1021/i160061a021.

DONG, Junqi et al. Air-side thermal hydraulic performance of offset strip fin aluminum heat exchangers. **Applied Thermal Engineering**, 2007. ISSN 13594311. DOI: 10.1016/j.applthermaleng.2006.08.005.

FILONENKO, G. K. Hydraulic resistance in pipes. **Teploenergetika**, 1954.

FOX, Robert W.; MCDONALD, Alan T.; PRITCHARD, Philip J. **Introdução à mecânica dos fluidos**. [S.l.: s.n.], 2014.

GHAJAR, Afshin J.; TAM, Lap Mou. Heat transfer measurements and correlations in the transition region for a circular tube with three different inlet configurations. **Experimental Thermal and Fluid Science**, 1994. ISSN 08941777. DOI: 10.1016/0894-1777(94)90075-2.

GNIELINSKI, Volker. Neue Gleichungen für den Wärme- und den Stoffübergang in turbulent durchströmten Rohren und Kanälen. **Forschung im Ingenieurwesen**, 1975. ISSN 00157899. DOI: 10.1007/BF02559682.

GUPTA, Raghvendra et al. Thermohydraulic performance of a periodic trapezoidal channel with a triangular cross-section. **International Journal of Heat and Mass Transfer**, 2008. ISSN 00179310. DOI: 10.1016/j.ijheatmasstransfer.2007.09.017.

HAALAND, S. E. Simple and explicit formulas for the friction factor in turbulent pipe flow. **Journal of Fluids Engineering, Transactions of the ASME**, 1983. ISSN 1528901X. DOI: 10.1115/1.3240948.

HESSELGREAVES, John E. **Compact heat exchangers: selection, design and operation**. [S.l.]: Butterworth-Heinemann, 2000.

HUANG, Changye et al. **Review on the characteristics of flow and heat transfer in printed circuit heat exchangers**. [S.l.: s.n.], 2019. DOI: 10.1016/j.applthermaleng.2019.02.131.

HULSE, P. M. **Fabricação e Análise Estrutural, morfológica e Termo Hidráulica de um Trocador de Calor Tipo Circuito Impresso**. [S.l.: s.n.], 2020.

INCROPERA, Frank P et al. **Fundamentos de Transferência de Calor E de Massa**. [S.l.]: Grupo Gen-LTC, 2014.

JENG, Tzer Ming; TZENG, Sheng Chung. Pressure drop and heat transfer of square pin-fin arrays in in-line and staggered arrangements. **International Journal of Heat and Mass Transfer**, 2007. ISSN 00179310. DOI: 10.1016/j.ijheatmasstransfer.2006.10.028.

JUNIOR, Armando Albertazzi Gonçalves; SOUSA, Andre Roberto de. **Fundamentos de Metrologia Científica e Industrial**. [S.l.]: Manole, 2008.

KIM, Dong Eok et al. Numerical investigation on thermal-hydraulic performance of new printed circuit heat exchanger model. **Nuclear Engineering and Design**, 2008. ISSN 00295493. DOI: 10.1016/j.nucengdes.2008.08.002.

LEE, Sang Moon; KIM, Kwang Yong. Comparative study on performance of a zigzag printed circuit heat exchanger with various channel shapes and configurations. **Heat and Mass Transfer/Waerme- und Stoffuebertragung**, 2013. ISSN 09477411. DOI: 10.1007/s00231-013-1149-4.

MANGLIK, Raj M.; BERGLES, Arthur E. Heat transfer and pressure drop correlations for the rectangular offset strip fin compact heat exchanger. **Experimental Thermal and Fluid Science**, 1995. ISSN 08941777. DOI: 10.1016/0894-1777(94)00096-Q.

MORTEAN, Marcus Vinícius Volponi. **Trocadores de calor compactos soldados por difusão: fabricação e modelagem**. 2017. PhD thesis – Universidade Federal de Santa Catarina.

MUZYCHKA, Yuri Stephan. **Analytical and experimental study of fluid friction and heat transfer in low Reynolds number flow heat exchangers**. 1999. PhD thesis – University of Waterloo.

NGO, Tri Lam et al. Heat transfer and pressure drop correlations of microchannel heat exchangers with S-shaped and zigzag fins for carbon dioxide cycles. **Experimental Thermal and Fluid Science**, 2007. ISSN 08941777. DOI: 10.1016/j.expthermflusci.2007.06.006.

PETUKHOV, BS; KURGANOV, VA; GLADUNTSOV, AI. Heat transfer in turbulent pipe flow of gases with variable properties. **Heat Transfer-Soviet Research**, v. 5, 1973.

ŞARA, O. N. Performance analysis of rectangular ducts with staggered square pin fins. **Energy Conversion and Management**, 2003. ISSN 01968904. DOI: 10.1016/S0196-8904(02)00185-1.

SARMIENTO, A. P.C.; SOARES, V. H.T.; CARQUEJA, G. G., et al. Thermal performance of diffusion-bonded compact heat exchangers. **International Journal of Thermal Sciences**, Elsevier Masson SAS, v. 153, April 2019, p. 106384, 2020. ISSN 12900729. DOI: 10.1016/j.ijthermalsci.2020.106384. Disponível em: https://doi.org/10.1016/j.ijthermalsci.2020.106384.

SARMIENTO, A. P.C.; SOARES, V. H.T.; MILANEZ, F. H., et al. Heat transfer correlation for circular and non-circular ducts in the transition regime. **International Journal of Heat and Mass Transfer**, 2020. ISSN 00179310. DOI: 10.1016/j.ijheatmasstransfer.2019.119165.

SHAH, R. K. A Correlation for Laminar Hydrodynamic Entry Length Solutions for Circular and Noncircular Ducts. **Journal of Fluids Engineering, Transactions of the ASME**, 1978. ISSN 00982202. DOI: 10.1115/1.3448626.

SHAH, Ramesh K.; SEKULIC, Dušan P. **Fundamentals of Heat Exchanger Design**. [S.l.: s.n.], 2003. DOI: 10.1002/9780470172605.

TAM, Hou Kuan; TAM, Lap Mou; GHAJAR, Afshin J. Effect of inlet geometries and heating on the entrance and fully-developed friction factors in the laminar and transition regions of a horizontal tube. **Experimental Thermal and Fluid Science**, 2013. ISSN 08941777. DOI: 10.1016/j.expthermflusci.2012.09.008.

TAM, Lap Mou; GHAJAR, Afshin J. Transitional heat transfer in plain horizontal tubes. In: 5. HEAT Transfer Engineering. [S.l.: s.n.], 2006. P. 23–38. DOI: 10.1080/01457630600559538.

TSUZUKI, Nobuyoshi; KATO, Yasuyoshi; ISHIDUKA, Takao. High performance printed circuit heat exchanger. **Applied Thermal Engineering**, v. 27, n. 10, p. 1702–1707, 2007. ISSN 1359-4311. DOI: https://doi.org/10.1016/j.applthermaleng.2006.07.007. Disponível em: https://www.sciencedirect.com/science/article/pii/S1359431106002493.

VANFOSSEN, G. J. Heat-transfer coefficients for staggered arrays of short pin fins. **Journal of Engineering for Gas Turbines and Power**, 1982. ISSN 15288919. DOI: 10.1115/1.3227275.

YOON, Seung Hyun; NO, Hee Cheon; KANG, Gil Beom. Assessment of straight, zigzag, S-shape, and airfoil PCHEs for intermediate heat exchangers of HTGRs and SFRs. **Nuclear Engineering and Design**, 2014. ISSN 00295493. DOI: 10.1016/j.nucengdes.2014.01.006.

ZHENG, Xiangyang; QI, Zhaogang. **A comprehensive review of offset strip fin and its applications**. [S.l.: s.n.], 2018. DOI: 10.1016/j.applthermaleng.2018.04.101.

APPENDIX A – TEST DATA

Below, the direct measurements of inlet and outlet temperatures, pressure drops and mass flow rates are shown. Test nomenclature follows the following rules: to each test, three numbers are given: targeted hot stream inlet temperature, targeted hot stream mass flow rate and targeted cold stream mass flow rate. A hyphen is used to separate them, whereas an underscore is used to substitute the comma. Therefore, test 70-0_100-0_010 corresponds to a targeted hot stream inlet temperature of 70°C, a targeted hot stream mass flow rate of $0,100$kg/s and a targeted cold stream mass flow rate of $0,010$kg/s.

Table 16 shows measured data relative to the cold stream, whereas table 17 refers to the hot stream. Measurement uncertainties were calculated following the method described in appendix B for a level of confidence of 95,45%.

Table 16 – Cold stream data.

Test	$T_{c,in}$ [°C]	$T_{c,out}$ [°C]	$\dot{m}_c$ [kg/s]	Δp_c [kPa]
70-0_100-0_010	$9,40 \pm 0,13$	$56,94 \pm 0,23$	$0,008716 \pm 0,000048$	$-1,3 \pm 4,3$
70-0_100-0_020	$11,66 \pm 0,14$	$41,01 \pm 0,19$	$0,0235 \pm 0,0014$	$1,5 \pm 4,3$
70-0_100-0_030	$13,13 \pm 0,14$	$35,18 \pm 0,18$	$0,0334 \pm 0,001$	$5,0 \pm 4,3$
70-0_100-0_040	$17,25 \pm 0,15$	$34,47 \pm 0,18$	$0,0431 \pm 0,0012$	$9,4 \pm 4,3$
70-0_100-0_050	$16,71 \pm 0,15$	$31,15 \pm 0,18$	$0,0546 \pm 0,0014$	$15,3 \pm 4,3$
70-0_100-0_060	$19,28 \pm 0,15$	$31,77 \pm 0,18$	$0,0619 \pm 0,0016$	$19,8 \pm 4,3$
70-0_100-0_080	$20,70 \pm 0,16$	$30,29 \pm 0,17$	$0,0815 \pm 0,0018$	$36 \pm 4,3$
70-0_100-0_100	$21,55 \pm 0,16$	$29,52 \pm 0,17$	$0,0998 \pm 0,0019$	$52,7 \pm 4,3$
70-0_100-0_120	$22,18 \pm 0,16$	$28,86 \pm 0,17$	$0,1215 \pm 0,0019$	$76,6 \pm 4,3$
70-0_100-0_140	$22,50 \pm 0,16$	$28,37 \pm 0,17$	$0,1400 \pm 0,0018$	$100,1 \pm 4,3$
70-0_100-0_160	$22,85 \pm 0,16$	$28,05 \pm 0,17$	$0,1599 \pm 0,0025$	$127,3 \pm 4,3$
70-0_100-0_170	$22,95 \pm 0,16$	$27,85 \pm 0,17$	$0,1715 \pm 0,0026$	$142,1 \pm 4,3$
70-0_150-0_010	$9,45 \pm 0,13$	$58,96 \pm 0,23$	$0,008691 \pm 0,000026$	$-1,3 \pm 4,3$
70-0_150-0_020	$11,84 \pm 0,14$	$41,67 \pm 0,20$	$0,0253 \pm 0,0018$	$2,0 \pm 4,3$
70-0_150-0_030	$15,30 \pm 0,14$	$38,30 \pm 0,19$	$0,0327 \pm 0,0014$	$5,1 \pm 4,3$
70-0_150-0_040	$17,63 \pm 0,15$	$35,64 \pm 0,18$	$0,0461 \pm 0,0016$	$10,2 \pm 4,3$
70-0_150-0_050	$16,76 \pm 0,15$	$33,99 \pm 0,18$	$0,0484 \pm 0,0014$	$12,1 \pm 4,3$
70-0_150-0_060	$20,28 \pm 0,15$	$33,57 \pm 0,18$	$0,0624 \pm 0,0021$	$20,6 \pm 4,3$
70-0_150-0_080	$21,27 \pm 0,16$	$31,82 \pm 0,18$	$0,0799 \pm 0,0017$	$34,7 \pm 4,3$
70-0_150-0_100	$22,15 \pm 0,16$	$30,70 \pm 0,17$	$0,1019 \pm 0,0019$	$55,1 \pm 4,3$
70-0_150-0_120	$22,73 \pm 0,16$	$30,12 \pm 0,17$	$0,1203 \pm 0,0023$	$75,4 \pm 4,3$
70-0_150-0_140	$23,35 \pm 0,16$	$29,67 \pm 0,17$	$0,1427 \pm 0,0019$	$103,4 \pm 4,3$
70-0_150-0_160	$23,66 \pm 0,16$	$29,31 \pm 0,17$	$0,16 \pm 0,0024$	$128,6 \pm 4,3$
70-0_150-0_170	$23,85 \pm 0,16$	$29,20 \pm 0,17$	$0,1706 \pm 0,0027$	$141,7 \pm 4,3$
70-0_200-0_010	$9,45 \pm 0,13$	$59,41 \pm 0,23$	$0,008681 \pm 0,000073$	$-1,3 \pm 4,3$

70-0_200-0_020	$11,84 \pm 0,14$	$43,67 \pm 0,20$	$0,0242 \pm 0,0019$	$1,7 \pm 4,3$
70-0_200-0_030	$15,44 \pm 0,15$	$39,45 \pm 0,19$	$0,0332 \pm 0,0013$	$5,1 \pm 4,3$
70-0_200-0_040	$18,15 \pm 0,15$	$36,97 \pm 0,19$	$0,0449 \pm 0,0015$	$9,8 \pm 4,3$
70-0_200-0_050	$17,16 \pm 0,15$	$35,17 \pm 0,18$	$0,0484 \pm 0,0015$	$12 \pm 4,3$
70-0_200-0_060	$20,15 \pm 0,15$	$34,71 \pm 0,18$	$0,0596 \pm 0,0015$	$18,6 \pm 4,3$
70-0_200-0_080	$21,80 \pm 0,16$	$32,79 \pm 0,18$	$0,0819 \pm 0,0018$	$35,4 \pm 4,3$
70-0_200-0_100	$22,86 \pm 0,16$	$31,85 \pm 0,18$	$0,1009 \pm 0,0021$	$54,4 \pm 4,3$
70-0_200-0_120	$23,45 \pm 0,16$	$31,23 \pm 0,18$	$0,1193 \pm 0,0019$	$74,2 \pm 4,3$
70-0_200-0_140	$23,95 \pm 0,16$	$30,68 \pm 0,17$	$0,1416 \pm 0,002$	$99 \pm 4,3$
70-0_200-0_160	$24,22 \pm 0,16$	$30,28 \pm 0,17$	$0,1601 \pm 0,0026$	$123,7 \pm 4,3$
70-0_200-0_170	$24,46 \pm 0,16$	$30,14 \pm 0,17$	$0,1718 \pm 0,0027$	$141,5 \pm 4,3$
80-0_100-0_010	$9,95 \pm 0,13$	$64,06 \pm 0,24$	$0,009519 \pm 0,000025$	$-1 \pm 4,3$
80-0_100-0_020	$12,81 \pm 0,14$	$45,19 \pm 0,20$	$0,0242 \pm 0,0017$	$2,1 \pm 4,3$
80-0_100-0_030	$14,72 \pm 0,14$	$40,29 \pm 0,19$	$0,0331 \pm 0,0012$	$5,2 \pm 4,3$
80-0_100-0_040	$16,53 \pm 0,15$	$38,07 \pm 0,19$	$0,04 \pm 0,0018$	$8,6 \pm 4,3$
80-0_100-0_050	$17,35 \pm 0,15$	$34,46 \pm 0,18$	$0,0516 \pm 0,0017$	$15,1 \pm 4,3$
80-0_100-0_060	$20,36 \pm 0,15$	$35,06 \pm 0,18$	$0,0635 \pm 0,0024$	$19,7 \pm 4,3$
80-0_100-0_080	$21,50 \pm 0,16$	$33,08 \pm 0,18$	$0,0824 \pm 0,0023$	$33,6 \pm 4,3$
80-0_100-0_100	$22,49 \pm 0,16$	$31,76 \pm 0,18$	$0,1037 \pm 0,0026$	$54 \pm 4,3$
80-0_100-0_120	$23,08 \pm 0,16$	$31,09 \pm 0,18$	$0,12 \pm 0,0021$	$73,6 \pm 4,3$
80-0_100-0_140	$23,65 \pm 0,16$	$30,55 \pm 0,17$	$0,1414 \pm 0,0019$	$100,3 \pm 4,3$
80-0_100-0_160	$23,96 \pm 0,16$	$30,15 \pm 0,17$	$0,1586 \pm 0,0025$	$124,5 \pm 4,3$
80-0_100-0_170	$24,01 \pm 0,16$	$29,81 \pm 0,17$	$0,1722 \pm 0,0031$	$141,5 \pm 4,3$
80-0_150-0_010	$9,92 \pm 0,13$	$65,61 \pm 0,24$	$0,00959 \pm 0,000033$	$-1 \pm 4,3$
80-0_150-0_020	$12,29 \pm 0,14$	$48,19 \pm 0,21$	$0,0241 \pm 0,0013$	$1,8 \pm 4,3$
80-0_150-0_030	$14,19 \pm 0,14$	$42,11 \pm 0,20$	$0,0334 \pm 0,0012$	$5,2 \pm 4,3$
80-0_150-0_040	$18,39 \pm 0,15$	$39,57 \pm 0,19$	$0,045 \pm 0,0018$	$10 \pm 4,3$
80-0_150-0_050	$17,49 \pm 0,15$	$36,66 \pm 0,19$	$0,0521 \pm 0,0015$	$14,2 \pm 4,3$
80-0_150-0_060	$20,47 \pm 0,15$	$36,71 \pm 0,19$	$0,0626 \pm 0,0018$	$19,4 \pm 4,3$
80-0_150-0_080	$21,97 \pm 0,16$	$34,55 \pm 0,18$	$0,0811 \pm 0,0019$	$34,5 \pm 4,3$
80-0_150-0_100	$22,94 \pm 0,16$	$33,28 \pm 0,18$	$0,1023 \pm 0,0022$	$53,2 \pm 4,3$
80-0_150-0_120	$23,47 \pm 0,16$	$32,24 \pm 0,18$	$0,123 \pm 0,0019$	$77,1 \pm 4,3$
80-0_150-0_140	$23,92 \pm 0,16$	$31,62 \pm 0,18$	$0,1425 \pm 0,002$	$101,2 \pm 4,3$
80-0_150-0_160	$24,27 \pm 0,16$	$31,19 \pm 0,18$	$0,1614 \pm 0,0024$	$125,5 \pm 4,3$
80-0_150-0_170	$24,47 \pm 0,16$	$31,00 \pm 0,18$	$0,172 \pm 0,0028$	$141,5 \pm 4,3$
80-0_200-0_010	$9,71 \pm 0,13$	$68,32 \pm 0,25$	$0,00888 \pm 0,000030$	$-1,3 \pm 4,3$
80-0_200-0_020	$13,51 \pm 0,14$	$51,02 \pm 0,21$	$0,0223 \pm 0,0021$	$1,5 \pm 4,3$
80-0_200-0_030	$14,24 \pm 0,14$	$43,84 \pm 0,20$	$0,033 \pm 0,0012$	$5,0 \pm 4,3$
80-0_200-0_040	$18,51 \pm 0,15$	$41,46 \pm 0,20$	$0,0434 \pm 0,0014$	$9,2 \pm 4,3$

80-0_200-0_050	$18,32 \pm 0,15$	$37,93 \pm 0,19$	$0,0536 \pm 0,0015$	$14,9 \pm 4,3$
80-0_200-0_060	$20,97 \pm 0,16$	$38,03 \pm 0,19$	$0,0621 \pm 0,0016$	$19,7 \pm 4,3$
80-0_200-0_080	$22,70 \pm 0,16$	$35,99 \pm 0,18$	$0,0808 \pm 0,0017$	$34,8 \pm 4,3$
80-0_200-0_100	$23,71 \pm 0,16$	$34,68 \pm 0,18$	$0,1008 \pm 0,002$	$53,3 \pm 4,3$
80-0_200-0_120	$24,49 \pm 0,16$	$33,82 \pm 0,18$	$0,1208 \pm 0,0021$	$76 \pm 4,3$
80-0_200-0_140	$25,03 \pm 0,16$	$33,18 \pm 0,18$	$0,142 \pm 0,0020$	$100,8 \pm 4,3$
80-0_200-0_160	$25,41 \pm 0,16$	$32,55 \pm 0,18$	$0,163 \pm 0,0024$	$130,2 \pm 4,3$
80-0_200-0_170	$25,53 \pm 0,16$	$32,37 \pm 0,18$	$0,172 \pm 0,0027$	$141,6 \pm 4,3$

Table 17 – Hot stream data.

Test	$T_{h,in}$ [°C]	$T_{h,out}$ [°C]	$\dot{m}_h$ [kg/s]	Δp_h [Pa]
70-0_100-0_010	$70,38 \pm 0,25$	$65,77 \pm 0,24$	$0,0919 \pm 0,0018$	$4088,1 \pm 1,7$
70-0_100-0_020	$70,26 \pm 0,25$	$63,51 \pm 0,24$	$0,0982 \pm 0,0023$	$4627,3 \pm 1,8$
70-0_100-0_030	$70,22 \pm 0,25$	$62,51 \pm 0,24$	$0,0939 \pm 0,0017$	$4291,2 \pm 1,5$
70-0_100-0_040	$70,63 \pm 0,25$	$63,22 \pm 0,24$	$0,0998 \pm 0,0017$	$4993 \pm 2,1$
70-0_100-0_050	$70,19 \pm 0,25$	$62,37 \pm 0,24$	$0,10 \pm 0,0018$	$5102,1 \pm 3,7$
70-0_100-0_060	$70,18 \pm 0,25$	$62,53 \pm 0,24$	$0,0997 \pm 0,0018$	$4998 \pm 2,0$
70-0_100-0_080	$70,37 \pm 0,25$	$62,49 \pm 0,24$	$0,0992 \pm 0,0018$	$5014,3 \pm 1,8$
70-0_100-0_100	$70,09 \pm 0,25$	$62,16 \pm 0,24$	$0,0989 \pm 0,0018$	$5027,2 \pm 1,7$
70-0_100-0_120	$70,34 \pm 0,25$	$62,24 \pm 0,24$	$0,0997 \pm 0,0019$	$5025,7 \pm 1,9$
70-0_100-0_140	$70,41 \pm 0,25$	$62,20 \pm 0,24$	$0,099 \pm 0,0018$	$5023 \pm 1,6$
70-0_100-0_160	$70,54 \pm 0,25$	$62,23 \pm 0,24$	$0,10 \pm 0,0021$	$5019,2 \pm 1,6$
70-0_100-0_170	$70,55 \pm 0,25$	$62,17 \pm 0,24$	$0,1009 \pm 0,0018$	$4988,6 \pm 1,7$
70-0_150-0_010	$70,40 \pm 0,25$	$67,42 \pm 0,25$	$0,1499 \pm 0,0019$	9897 ± 24
70-0_150-0_020	$70,15 \pm 0,25$	$65,11 \pm 0,24$	$0,1452 \pm 0,0022$	$9204,1 \pm 5,6$
70-0_150-0_030	$69,80 \pm 0,25$	$64,58 \pm 0,24$	$0,1444 \pm 0,0020$	$9290 \pm 3,2$
70-0_150-0_040	$70,65 \pm 0,25$	$65,12 \pm 0,24$	$0,1476 \pm 0,0020$	9711 ± 27
70-0_150-0_050	$70,38 \pm 0,25$	$64,75 \pm 0,24$	$0,1488 \pm 0,0019$	$10383,7 \pm 4,1$
70-0_150-0_060	$70,51 \pm 0,25$	$64,80 \pm 0,24$	$0,1474 \pm 0,0025$	9719 ± 35
70-0_150-0_080	$70,27 \pm 0,25$	$64,39 \pm 0,24$	$0,1473 \pm 0,0019$	9612 ± 31
70-0_150-0_100	$70,27 \pm 0,25$	$64,26 \pm 0,24$	$0,1475 \pm 0,0019$	9696 ± 35
70-0_150-0_120	$70,38 \pm 0,25$	$64,28 \pm 0,24$	$0,1477 \pm 0,0022$	9685 ± 29
70-0_150-0_140	$70,33 \pm 0,25$	$64,18 \pm 0,24$	$0,1472 \pm 0,0019$	9702 ± 35
70-0_150-0_160	$70,22 \pm 0,25$	$64,04 \pm 0,24$	$0,1488 \pm 0,0021$	9746 ± 39
70-0_150-0_170	$70,22 \pm 0,25$	$64,01 \pm 0,24$	$0,1479 \pm 0,0021$	9708 ± 34
70-0_200-0_010	$69,87 \pm 0,25$	$67,54 \pm 0,25$	$0,1926 \pm 0,0033$	$15891,7 \pm 4,8$
70-0_200-0_020	$69,95 \pm 0,25$	$66,09 \pm 0,24$	$0,1882 \pm 0,0035$	15525 ± 39
70-0_200-0_030	$69,82 \pm 0,25$	$65,78 \pm 0,24$	$0,1958 \pm 0,0034$	16322 ± 19
70-0_200-0_040	$70,24 \pm 0,25$	$65,87 \pm 0,24$	$0,1911 \pm 0,0034$	$16061 \pm 6,0$

70-0_200-0_050	$70,40 \pm 0,25$	$65,83 \pm 0,24$	$0,1898 \pm 0,0033$	15941 ± 26
70-0_200-0_060	$70,37 \pm 0,25$	$65,79 \pm 0,24$	$0,1904 \pm 0,0033$	$16065,5 \pm 6,2$
70-0_200-0_080	$70,33 \pm 0,25$	$65,58 \pm 0,24$	$0,191 \pm 0,0033$	$16070,3 \pm 5,5$
70-0_200-0_100	$70,15 \pm 0,25$	$65,33 \pm 0,24$	$0,1908 \pm 0,0033$	$16026 \pm 4,5$
70-0_200-0_120	$70,10 \pm 0,25$	$65,21 \pm 0,24$	$0,1916 \pm 0,0033$	$16022,4 \pm 4,6$
70-0_200-0_140	$70,07 \pm 0,25$	$65,18 \pm 0,24$	$0,194 \pm 0,0035$	$16697,9 \pm 4,4$
70-0_200-0_160	$70,18 \pm 0,25$	$65,24 \pm 0,24$	$0,1931 \pm 0,0034$	$16776,9 \pm 4,8$
70-0_200-0_170	$70,46 \pm 0,25$	$65,46 \pm 0,24$	$0,1952 \pm 0,0034$	16746 ± 11
80-0_100-0_010	$80,26 \pm 0,27$	$74,84 \pm 0,26$	$0,099 \pm 0,0022$	4603 ± 18
80-0_100-0_020	$80,17 \pm 0,27$	$71,93 \pm 0,25$	$0,0956 \pm 0,0019$	$4215,3 \pm 1,6$
80-0_100-0_030	$80,20 \pm 0,27$	$71,29 \pm 0,25$	$0,0951 \pm 0,0017$	$4225,2 \pm 3,2$
80-0_100-0_040	$79,74 \pm 0,27$	$71,23 \pm 0,25$	$0,1013 \pm 0,0023$	$5541,9 \pm 1,5$
80-0_100-0_050	$79,96 \pm 0,27$	$70,58 \pm 0,25$	$0,0995 \pm 0,0019$	$4900,9 \pm 4,4$
80-0_100-0_060	$80,24 \pm 0,27$	$70,86 \pm 0,25$	$0,0977 \pm 0,0026$	5034 ± 16
80-0_100-0_080	$80,26 \pm 0,27$	$70,46 \pm 0,25$	$0,098 \pm 0,0021$	4886 ± 14
80-0_100-0_100	$80,11 \pm 0,27$	$70,11 \pm 0,25$	$0,0961 \pm 0,0023$	4881 ± 12
80-0_100-0_120	$80 \pm 0,27$	$69,99 \pm 0,25$	$0,0967 \pm 0,0019$	$4990,9 \pm 7,0$
80-0_100-0_140	$80,03 \pm 0,27$	$69,93 \pm 0,25$	$0,097 \pm 0,0017$	$4995,3 \pm 7,0$
80-0_100-0_160	$80,04 \pm 0,27$	$69,85 \pm 0,25$	$0,0958 \pm 0,002$	$4991 \pm 7,4$
80-0_100-0_170	$80,02 \pm 0,27$	$69,75 \pm 0,25$	$0,0969 \pm 0,0022$	$4991 \pm 9,4$
80-0_150-0_010	$79,92 \pm 0,27$	$76,12 \pm 0,26$	$0,1455 \pm 0,0023$	9270 ± 19
80-0_150-0_020	$80,29 \pm 0,27$	$74,50 \pm 0,26$	$0,1435 \pm 0,0018$	9120 ± 11
80-0_150-0_030	$79,90 \pm 0,27$	$73,69 \pm 0,26$	$0,1487 \pm 0,0019$	$9746 \pm 2,5$
80-0_150-0_040	$80 \pm 0,27$	$73,44 \pm 0,26$	$0,1452 \pm 0,002$	9588 ± 30
80-0_150-0_050	$80,10 \pm 0,27$	$73,31 \pm 0,26$	$0,1478 \pm 0,002$	10221 ± 10
80-0_150-0_060	$80,19 \pm 0,27$	$73,31 \pm 0,26$	$0,1453 \pm 0,0019$	9631 ± 23
80-0_150-0_080	$80,08 \pm 0,27$	$72,92 \pm 0,26$	$0,1436 \pm 0,0019$	9466 ± 34
80-0_150-0_100	$79,97 \pm 0,27$	$72,70 \pm 0,26$	$0,1454 \pm 0,0021$	$9513,1 \pm 4,3$
80-0_150-0_120	$80,16 \pm 0,27$	$72,67 \pm 0,26$	$0,1439 \pm 0,0019$	$9325,7 \pm 3,9$
80-0_150-0_140	$80,20 \pm 0,27$	$72,60 \pm 0,26$	$0,1448 \pm 0,002$	$9231,8 \pm 3,7$
80-0_150-0_160	$80,20 \pm 0,27$	$72,54 \pm 0,26$	$0,1438 \pm 0,0018$	$9251,7 \pm 2,7$
80-0_150-0_170	$80,32 \pm 0,27$	$72,63 \pm 0,26$	$0,1466 \pm 0,0024$	$9419,7 \pm 3,2$
80-0_200-0_010	$80,44 \pm 0,27$	$77,59 \pm 0,26$	$0,1877 \pm 0,0032$	$15176,7 \pm 5,3$
80-0_200-0_020	$79,87 \pm 0,27$	$75,90 \pm 0,26$	$0,2057 \pm 0,0041$	19053 ± 14
80-0_200-0_030	$80,41 \pm 0,27$	$75,40 \pm 0,26$	$0,1938 \pm 0,0033$	15931 ± 43
80-0_200-0_040	$80,21 \pm 0,27$	$75,06 \pm 0,26$	$0,191 \pm 0,0033$	16919 ± 43
80-0_200-0_050	$79,82 \pm 0,27$	$74,48 \pm 0,26$	$0,1958 \pm 0,0035$	16749 ± 11
80-0_200-0_060	$80,46 \pm 0,27$	$74,98 \pm 0,26$	$0,1913 \pm 0,0033$	$16919,1 \pm 6,4$
80-0_200-0_080	$80,49 \pm 0,27$	$74,77 \pm 0,26$	$0,1901 \pm 0,0032$	16665 ± 19

80-0_200-0_100	$80,51 \pm 0,27$	$74,64 \pm 0,26$	$0,1879 \pm 0,0032$	16547 ± 14
80-0_200-0_120	$80,45 \pm 0,27$	$74,61 \pm 0,26$	$0,1937 \pm 0,0034$	$17338,4 \pm 4,9$
80-0_200-0_140	$80,54 \pm 0,27$	$74,61 \pm 0,26$	$0,1936 \pm 0,0035$	$17335,2 \pm 7,4$
80-0_200-0_160	$80,39 \pm 0,27$	$74,39 \pm 0,26$	$0,1929 \pm 0,0034$	$17254,7 \pm 5,4$
80-0_200-0_170	$80,58 \pm 0,27$	$74,52 \pm 0,26$	$0,1922 \pm 0,0034$	$17185,2 \pm 6,0$

APPENDIX B – METROLOGICAL PROCEDURE

The present appendix is dedicated to the presentation of the metrological procedure used to obtain both directly and indirectly measured physical quantities. Details concerning metrology in general as well as explanations in further detail can be found in Junior and Sousa (2008).

Metrology is defined as the *science of measurement and its application*, including *all theoretical and practical aspects of measurement, whatever the measurement uncertainty and field of application.* BIPM (2012).

B.1 DIRECT MEASUREMENTS

Direct measurements are obtained when no further mathematical manipulation is needed, once an adequate result is obtained from a measuring system. In the present work, direct measurements involve temperature, pressure drop and mass flow rate.

The result of a direct measurement is given by the base result R_B plus or minus the measurement precision P. Therefore,

$$R_M = R_B \pm P \tag{B.1}$$

where R_M is the measurement result. The measurement precision is defined as *closeness of agreement between indications or measured quantity values obtained by replicate measurements on the same or similar objects under specified conditions* BIPM (2012). This means that the measured quantity is in the interval between $R_B - P$ and $R_B + P$.

If only the maximum error E_{max} of the system is known, the precision assumes its value and the base result is simply the indication provided by the system. In this case, $P = E_{max}$. If, however, the statistical behavior of the system is known, a more refined result can be obtained.

Measurement systems present two types of errors: systematic and random. Systematic error is the predictable part of the error. It represents the mean deviation between the indication and the real value of the measurand. The random component, on the other hand, cannot be predicted. Its behavior, however, can be described by statistical analysis. In the end, a final result consisting of an interval is obtained. Mathematically,

$$R_M = \overline{I} + C \pm U \tag{B.2}$$

where C is the sum of all corrections and U is the expanded uncertainty.

Systematic effects may arise from the system's behavior itself and from external sources as well. One example of an external source of systematic effect is temperature variation. System intrinsic correction values are obtained via a calibration process and must be given as a function of the indication. Mathematically, $C = -Td$, where Td is the tendency or systematic error of the measurement system. The tendency is the predictable

component of the measurement error. It corresponds to the mean deviation between the system indications and the real value.

The expanded uncertainty accounts for all sources of random error. Mathematically, it is given as

$$U = t(\alpha, \nu)u \tag{B.3}$$

where t is Student's t and u is the standard uncertainty. Student's t is a function of the level of confidence α and the number of degrees of freedom ν.

The standard uncertainty depends on the standard uncertainties of all sources of random error. Considering direct measurements with k independent sources of random error, one can write

$$u_c^2 = u_1^2 + ... + u_k^2 \tag{B.4}$$

where u_i is the standard uncertainty of the i-th source of random effects. When the i-th source is described by a variable with a normal distribution, then u_i corresponds to its standard deviation. Associated to each source of uncertainty there is a number of degrees of freedom ν_i. To calculate the effective number of degrees of freedom of the result, one can use the Welch-Satterthwaite equation:

$$\frac{u_c^4}{\nu_{eff}} = \frac{u_1^4}{\nu_1} + ... + \frac{u_k^4}{\nu_k} \tag{B.5}$$

This allows one to determine $t(\alpha, \nu_{eff})$, which enables the determination of U.

Just as previously mentioned, the uncertainty of a measurement system depends on multiple sources of uncertainty, such as the imprecision related to the correction itself, measurement repeatability, resolution, uncertainties regarding the systematic effects of temperature variation etc.

The correction uncertainty must be provided as a function of the indication, such as the correction itself, and its value depends on the quality of the calibration system among other things. Calibration data provides a correction $C(\overline{I}) \pm U_C$. The term U_C is the expanded uncertainty of the correction. Usually, it is given for $\alpha = 95,45\%$ and a large number of degrees of freedom is used, so that generally $t \approx 2$.

The measurement repeatability is *measurement precision under a set of repeatability conditions of measurement* (BIPM, 2012). According to the same source, repeatability condition of measurement is defined as a *condition of measurement, out of a set of conditions that includes the same measurement procedure, same operators, same measuring system, same operating conditions and same location, and replicate measurements on the same or similar objects over a short period of time.*

Repeatability can be obtained by sequencially measuring multiple times the same invariable measurand, obtaining the resulting sample standard deviation s and multiplying it by the appropriate value of Student's t, for the obtained number of degrees of freedom and desired level of confidence. Mathematically,

$$R_e = t(\alpha, \nu)s \tag{B.6}$$

where α is the level of confidence and ν is the number of degrees of freedom, given by

$$\nu = n - 1 \tag{B.7}$$

where n is the number of measurements. Repeatability can be directly obtained by performing multiple measurements whenever the measuring system is used. Therefore, there is no need to used external data regarding repeatability whenever multiple measurements can be made.

Once repeatability is known, one knows that any indication will fall between $\overline{I} - R_e$ and $\overline{I} + R_e$ for the selected level of confidence. The main interest, however, is to know the central value of the distribution, which must be corrected to provide result of measurement. Therefore, knowing where the mean value lies is more important than known where any random further indication from the system will be. The standard deviation of the average of n observations of a random variable X with standard deviation σ is $\sigma/\sqrt{n}$. This means that, when measuring invariable measurands, the effects of random error can be diminished by performing multiple measurements. Thus, if n measurements of the same invariable measurand are performed, the resulting repeatability can be divided by $\sqrt{n}$, meaning the final indication should be

$$R = \overline{I} \pm \frac{Re}{\sqrt{n}} = \overline{I} \pm t(\alpha, \nu)\frac{s}{\sqrt{n}} \tag{B.8}$$

where $\overline{I}$ is the average of all indications. Note that, in this case, $u = s/\sqrt{n}$.

When using a measuring system with resolution r, the related standard uncertainty is given by $u = r/\left(2\sqrt{3}\right)$. In this case, $\nu \to \infty$.

In the end, one should account for all sources of error. All corrections must be added, the standard uncertainties must be combined, the effective number of degrees of freedom must be obtained and the final result must be determined.

B.1.1 Temperatures

Such as explained in chapter **??**, PT-100 P-M-1/3-1/8-6-1/8-T-3 thermoresistances were used. Since no specific calibration was performed, the total error of this class of equipment was considered. The total error is a function of temperature. Class B thermoresistances have a maximum uncertainty of $\pm 0,30$°C at 0°C. The uncertainty increases linearly until $\pm 0,80$°C at 100°C. The used thermoresistances have a maximum uncertainty of one third of that of class B equipment.

Fluctuations in temperature readings arise from the system's natural repeatability and actual temperature fluctuations. It is important to notice that the stream temperatures are not constant, therefore, the sample standard deviation of the test readings will already account for both factors (repeatability and temperature fluctuations). However, the actual measurand, which is the mean temperature over the entire test, is, in fact, constant. The average of all temperature readings will be a random normal variable with standard

deviation estimated by $s/\sqrt{n}$, where s is the sample standard deviation of the readings themselves. Since no previous calibration was performed, the maximum possible errors must be considered in the analysis. Following the recommendations of Junior and Sousa (2008), the maximum error can be associated to a standard uncertainty of $E_{max}/\sqrt{3}$. This yields

$$u^2(T) = \left(\frac{s}{\sqrt{n}}\right)^2 + \left(\frac{E_{max}}{\sqrt{3}}\right)^2 \tag{B.9}$$

The effective number of degrees of freedom is obtained by equation B.5:

$$\frac{u^4(T)}{\nu_{eff}} = \frac{\left(s/\sqrt{n}\right)^4}{n-1} \tag{B.10}$$

The final result is presented as

$$T = \overline{I}_T \pm t(\alpha, \nu_{eff})u(T) \tag{B.11}$$

where $\overline{I}_T$ is the average of all temperature indications.

B.1.2 Volumetric flow rates

Mass flow rates were measured using *Rosemount-8732* electromagnetic flow meters, such as explained in chapter **??**. Both flow meters were connected to a *National Instruments cDAQ-9178* chassis connected to a computer, which stored the signal readings in text files. Electromagnetic flow meters measure the average flow velocity, which enables one to determine the volumetric flow rate once the tube's diameter is known.

The entire measurement system (flow meter, chassis and computer) was calibrated in the laboratory. Multiple flow rates were set and measured by the electromagnetic flow meters and also using the gravimetric method. Results were compared and the appropriate statistical analysis was performed to determine each flow meter's tendency curve and the respective uncertainties. The resulting curves can be seen in figures 78 and 79. Linear interpolation was used to determine the tendency between measured points.

The standard random uncertainty of volumetric flow rate is a function of the natural repeatability of the system, random fluctuations in the volumetric flow rate caused by turbulence and other possible sources and the uncertainty related to the correction. The first two factors are directly considered when calculating the sample standard deviation of all readings. Since the mean value of volumetric flow rate is the searched result, one considers the sample standard deviation divided by the square root of the number of measurements. This yields

$$u^2(\dot{V}) = \left(\frac{s}{\sqrt{n}}\right)^2 + u^2(C) \tag{B.12}$$

Figure 78 – Cold stream electromagnetic flow meter's tendency curve

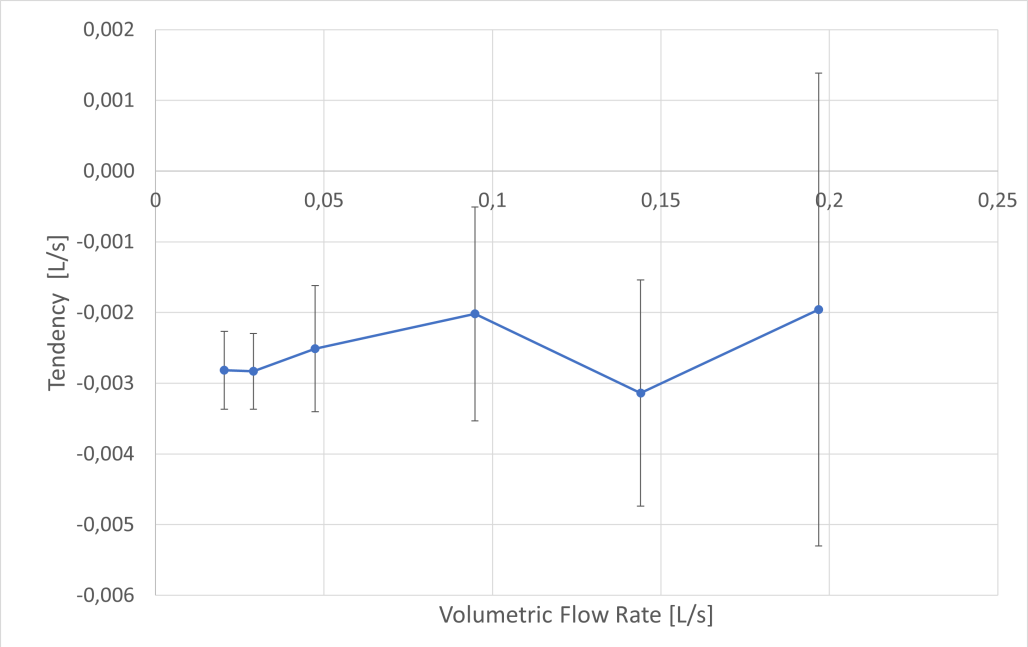

Figure 79 – Hot stream electromagnetic flow meter's tendency curve

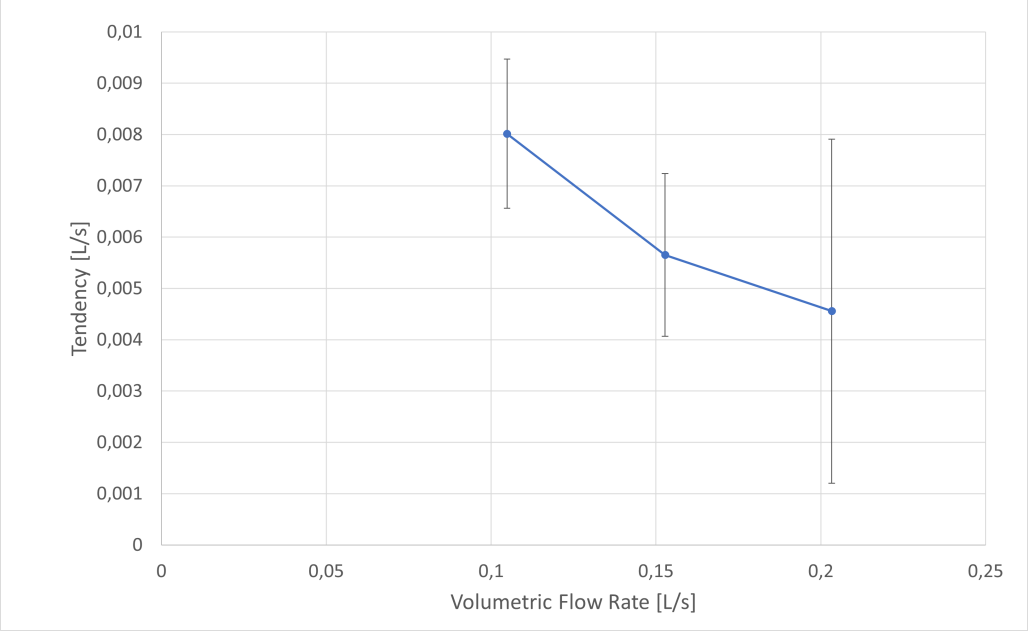

where $u(C)$ is the correction's standard uncertainty. The effective number of degrees of freedom is calclated using equation B.5:

$$\frac{u^4(\dot{V})}{\nu_{eff}} = \frac{\left(\frac{s}{\sqrt{n}}\right)^4}{n-1} + \frac{u^4(C)}{\nu_C} \tag{B.13}$$

where n is the number of measurements. The correction-related number of degrees of freedom ν_C is only known for the measuring points. Although tendency was linearly interpolated between such points to cover the entire measurement domain, whenever the indication fell between two known points, the least of the numbers of degrees of freedom of both points was used in a conservative approach.

One can thus write

$$\dot{V} = \overline{I} - Td \pm t(\alpha, \nu_{eff})u(\dot{V}) \tag{B.14}$$

B.1.3 Pressure drops

The differential pressure transducers used provide an output in the form of an electrical current, which is a function of the pressure difference between its terminals. The unit used in the cold stream was calibrated by a third party laboratory.

Such differential pressure sensors provide an output current between 4mA and 20mA. The minimum current corresponds to the absence of pressure difference, whereas the maximum one corresponds to the maximum pressure difference measurable by the sensor. Variations in pressure difference cause proportional variations in output current, so a linear interpolation is used to cover the entire domain.

During calibration, the sensor is subjected to multiple known pressure differences. At each stage, the output current is compared to the theoretical one that should be obtained by a perfect sensor. The difference between the measured current and the theoretical one is the tendency. A table containing tendency and its uncertainty for a total of 7 calibration points was provided by the laboratory.

Just as before, current readings are affected by the system's natural repeatability and pressure difference fluctuations. The sample standard deviation of the measured data reflects both effects. Since the time-average pressure drop must be obtained, the standard uncertainty related to both phenomena is $s/\sqrt{n}$, where s is the sample standard deviation of all measurements and n is the number of measurements.

The base result must be corrected based on the calibration data. The final standard uncertainty of the output current i is given by

$$u^2(i) = \left(\frac{s}{\sqrt{n}}\right)^2 + u^2_{calib} \tag{B.15}$$

where u_{calib} is the standard uncertainty of the calibration. Again, the effective number of degrees of freedom is given by equation B.5:

$$\frac{u^4(i)}{\nu_{eff}} = \frac{\left(s/\sqrt{n}\right)^4}{n-1} \tag{B.16}$$

The final result for the output current is expressed as

$$i = \overline{I}_i + C \pm t(\alpha, \nu_{eff})u(i) \tag{B.17}$$

where $\overline{I}_i$ is the average of all current readings. Finally, linear interpolation between both limits is performed to find the pressure drop.

B.2 INDIRECT MEASUREMENTS

Indirect measurements result from the application of a mathematical model to direct measurements. An indirect measured quantity y can be expressed as a function of n directly measured quantities $x_1, ..., x_n$. Mathematically, one can write

$$y = f(x_1, ..., x_n) \tag{B.18}$$

The standard uncertainty of y is given by

$$u^2(y) = \left[\frac{\partial y}{\partial x_1}u(x_1)\right]^2 + ... + \left[\frac{\partial y}{\partial x_n}u(x_n)\right]^2 \tag{B.19}$$

whereas the effective number of degrees of freedom of y is given by

$$\frac{\left[\frac{u(y)}{E(y)}\right]^4}{\nu_{eff}} = \frac{\left[\frac{u(x_1)}{E(x_1)}\right]^4}{\nu_1} + ... + \frac{\left[\frac{u(x_n)}{E(x_n)}\right]^4}{\nu_n} \tag{B.20}$$

where $E(x_i)$ is the expected value of x_i. In metrology, this is equivalent to the base result. The ratio $u(x_i)/E(x_i)$ is the relative standard uncertainty of x_i. The last two equations allow one to determine the expanded uncertainty for the desired level of confidence.

B.2.1 Heat transfer rate

The heat transfer rate can be calculated as a function of an enthalpy variation, such as expressed by equation 5.5:

$$q = \dot{m}_c\left(h_{c,out} - h_{c,in}\right) = \dot{m}_h\left(h_{h,in} - h_{h,out}\right)$$

Given that $h = u + pv$, any enthalpy variation can be expressed as

$$\Delta h = h_2 - h_1 = u_2 + \frac{p_2}{\rho_2} - \left(u_1 + \frac{p_1}{\rho_1}\right) = u_2 - u_1 + \frac{p_2 - p_1}{\overline{\rho}}$$

where $\overline{\rho}$ is such that

$$\frac{p_2}{\rho_2} - \frac{p_1}{\rho_1} = \frac{p_2 - p_1}{\overline{\rho}}$$

yielding

$$\overline{\rho} = \frac{p_2 - p_1}{\dfrac{p_2}{\rho_2} - \dfrac{p_1}{\rho_1}} \tag{B.21}$$

Since the density of water is nearly constant for the test conditions, the value of $\overline{\rho}$ can be considered sufficiently accurate to not have its uncertainty considered in the metrological procedure.

Regardless of the stream considered, the heat transfer rate is expressed by

$$q = \dot{m}\left(u_2 - u_1 + \frac{\Delta p}{\overline{\rho}}\right) \tag{B.22}$$

where $\Delta p = p_2 - p_1$. Therefore, the heat transfer rate has the functional form

$$q = q\left(\dot{m}, u_1, u_2, \Delta p\right) \tag{B.23}$$

Applying equation B.19 to the heat transfer rate yields

$$u^2(q) = \left[\frac{\partial q}{\partial \dot{m}}u(\dot{m})\right]^2 + \left[\frac{\partial q}{\partial u_2}u(u_2)\right]^2 + \left[\frac{\partial q}{\partial u_1}u(u_1)\right]^2 + \left[\frac{\partial q}{\partial(\Delta p)}u(\Delta p)\right]^2$$

$$u^2(q) = \left[\left(u_2 - u_1 + \frac{\Delta p}{\overline{\rho}}\right)u(\dot{m})\right]^2 + \left[\dot{m}u(u_2)\right]^2 + \left[\dot{m}u(u_1)\right]^2 + \left[\frac{\dot{m}}{\overline{\rho}}u(\Delta p)\right]^2$$

$$u^2(q) = (\Delta h)^2 u^2(\dot{m}) + \dot{m}^2\left[u^2(u_2) + u^2(u_1) + \frac{1}{\overline{\rho}^2}u^2(\Delta p)\right] \tag{B.24}$$

The effective number of degrees of freedom can then be obtained by writing

$$\frac{\left[\dfrac{u(q)}{E(q)}\right]^4}{\nu_q} = \frac{\left[\dfrac{u(\dot{m})}{E(\dot{m})}\right]^4}{\nu_{\dot{m}}} + \frac{\left[\dfrac{u(u_{i,1})}{E(u_{i,1})}\right]^4}{\nu_{u_{i,1}}} + \frac{\left[\dfrac{u(u_{i,2})}{E(u_{i,2})}\right]^4}{\nu_{u_{i,2}}} + \frac{\left[\dfrac{u(\Delta p)}{E(\Delta p)}\right]^4}{\nu_{\Delta p}} \tag{B.25}$$

In the last two equations, $u(\Delta p)$, $\nu_{\Delta p}$ and $E(\Delta p)$ are already known based on the results of the direct measurements. The mass flow rate comes simply by multiplying the volumetric flow rates by the water density. Since density values are considered to be accurately known, $u(\dot{m}) = \rho u(\dot{V})$ and $E(\dot{m}) = \rho E(\dot{V})$. Lastly, $\nu_{\dot{m}} = \nu_{\dot{V}}$.

The values of internal energy can be obtained from a saturated water thermodynamic table. Here, internal energy is considered to be only a function of temperature, since no expressive pressure variations are present. For the internal energy u_i, based on equation B.19, one has

$$u^2(u_i) = \left[\left(\frac{\partial u_i}{\partial T}\right)_v u(T)\right]^2 = \left[c_v u(T)\right]^2 \tag{B.26}$$

whereas for the effective number of degrees of freedom,

$$\frac{\left[\dfrac{u(u_i)}{E(u_i)}\right]^4}{\nu_{u_i}} = \frac{\left[\dfrac{u(T)}{E(T)}\right]^4}{\nu_T} \tag{B.27}$$

B.2.2 Thermal Conductance

The thermal conductance is given by rewriting equation 5.8 as

$$UA = \frac{q}{\Delta T_{lm}} \tag{B.28}$$

where

$$\Delta T_{lm} = \frac{\Delta T_B - \Delta T_A}{\ln\left(\dfrac{\Delta T_B}{\Delta T_A}\right)} \tag{B.29}$$

is the logarithmic mean temperature difference. Given that the heat exchanger operates in a counterflow arrangement,

$$\Delta T_A = T_{h,i} - T_{c,o} \tag{B.30}$$

$$\Delta T_B = T_{h,o} - T_{c,i} \tag{B.31}$$

Hence, UA is a function of q and ΔT_{lm}:

$$UA = UA\,(q, \Delta T_{lm}) \tag{B.32}$$

Based on equation B.19, one has

$$u^2(UA) = \left[\frac{1}{\Delta T_{lm}} u(q)\right]^2 + \left[-\frac{q}{(\Delta T_{lm})^2} u(q)\right]^2 \tag{B.33}$$

whereas the effective number of degrees of freedom of the thermal conductance can be obtained by writing

$$\frac{\left[\dfrac{u(UA)}{E(UA)}\right]^4}{\nu_{UA}} = \frac{\left[\dfrac{u(q)}{E(q)}\right]^4}{\nu_q} + \frac{\left[\dfrac{u(\Delta T_{lm})}{E(\Delta T_{lm})}\right]^4}{\nu_{\Delta T_{lm}}} \tag{B.34}$$

The values of $u(q)$, $E(q)$ and ν_q are known from the previous section. The standard uncertainty of the logarithmic mean temperature difference is obtained by applying equation B.19 to ΔT_{lm}:

$$u^2(\Delta T_{lm}) = \left[\frac{\partial(\Delta T_{lm})}{\partial(\Delta T_A)} u(\Delta T_A)\right]^2 + \left[\frac{\partial(\Delta T_{lm})}{\partial(\Delta T_B)} u(\Delta T_B)\right]^2 \tag{B.35}$$

This yields

$$u^2(\Delta T_{lm}) = \left[-\frac{\ln\left(\frac{\Delta T_B}{\Delta T_A}\right) + 1 - \frac{\Delta T_B}{\Delta T_A}}{\ln^2\left(\frac{\Delta T_B}{\Delta T_A}\right)} u(\Delta T_A) \right]^2 + \left[\frac{\ln\left(\frac{\Delta T_B}{\Delta T_A}\right) + \frac{\Delta T_A}{\Delta T_B} - 1}{\ln^2\left(\frac{\Delta T_B}{\Delta T_A}\right)} u(\Delta T_B) \right]^2 \tag{B.36}$$

For the effective number of degrees of freedom,

$$\frac{\left[\frac{u(\Delta T_{lm})}{E(\Delta T_{lm})}\right]^4}{\nu_{\Delta T_{lm}}} = \frac{\left[\frac{u(\Delta T_A)}{E(\Delta T_A)}\right]^4}{\nu_{\Delta T_A}} + \frac{\left[\frac{u(\Delta T_B)}{E(\Delta T_B)}\right]^4}{\nu_{\Delta T_B}} \tag{B.37}$$

Finally, the standard uncertainties and effective numbers of degrees of freedom of ΔT_A and ΔT_B must be obtained:

$$u^2(\Delta T_A) = u^2(T_{h,i}) + u^2(T_{c,o}) \tag{B.38}$$

$$u^2(\Delta T_B) = u^2(T_{h,o}) + u^2(T_{c,i}) \tag{B.39}$$

$$\frac{\left[\frac{u(\Delta T_A)}{E(\Delta T_A)}\right]^4}{\nu_{\Delta T_A}} = \frac{\left[\frac{u(T_{h,i})}{E(T_{h,i})}\right]^4}{\nu_{\Delta T_{h,i}}} + \frac{\left[\frac{u(T_{c,o})}{E(T_{c,o})}\right]^4}{\nu_{\Delta T_{c,o}}} \tag{B.40}$$

$$\frac{\left[\frac{u(\Delta T_B)}{E(\Delta T_B)}\right]^4}{\nu_{\Delta T_B}} = \frac{\left[\frac{u(T_{h,o})}{E(T_{h,o})}\right]^4}{\nu_{\Delta T_{h,o}}} + \frac{\left[\frac{u(T_{c,i})}{E(T_{c,i})}\right]^4}{\nu_{\Delta T_{c,i}}} \tag{B.41}$$

APPENDIX C – HEAT TRANSFER RATE AND THERMAL CONDUCTANCE

C.1 HEAT TRANSFER RATE

This section contains the individual plots of heat transfer rate of all test batteries not shown in chapter 7. Each test battery has the same targeted values of hot stream mass flow rate and inlet temperature and is individually represented in each figure. Although experimental results of all test batteries are shown in figure 62, this figure does not present measurement uncertainties. Therefore, the following figures were included in this appendix, so the reader is able to individually analyze each test battery.

Figure 80 – Heat transfer rate. Hot stream inlet temperature at 70°C and mass flow rate at $0,15$kg/s.

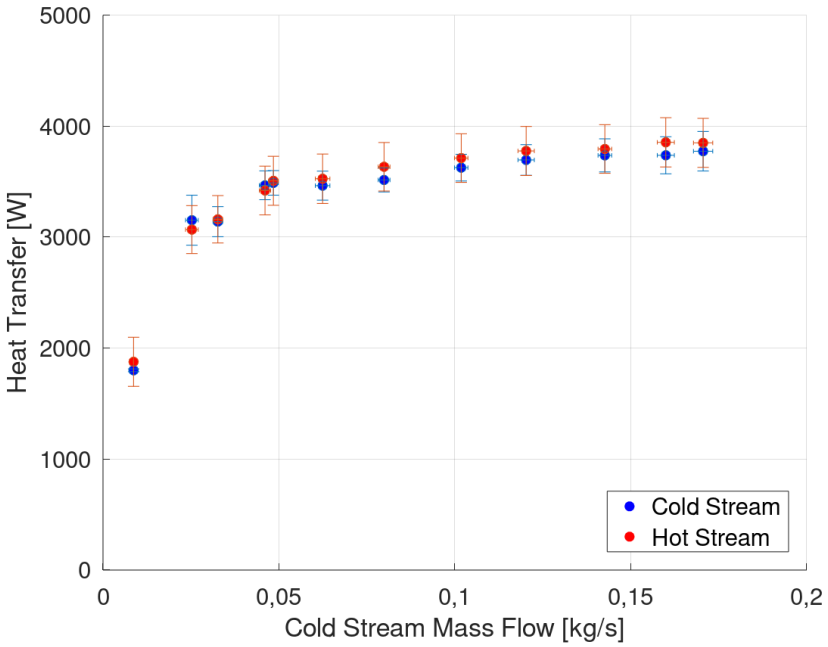

Figure 81 – Heat transfer rate. Hot stream inlet temperature at 70°C and mass flow rate at $0,2$kg/s.

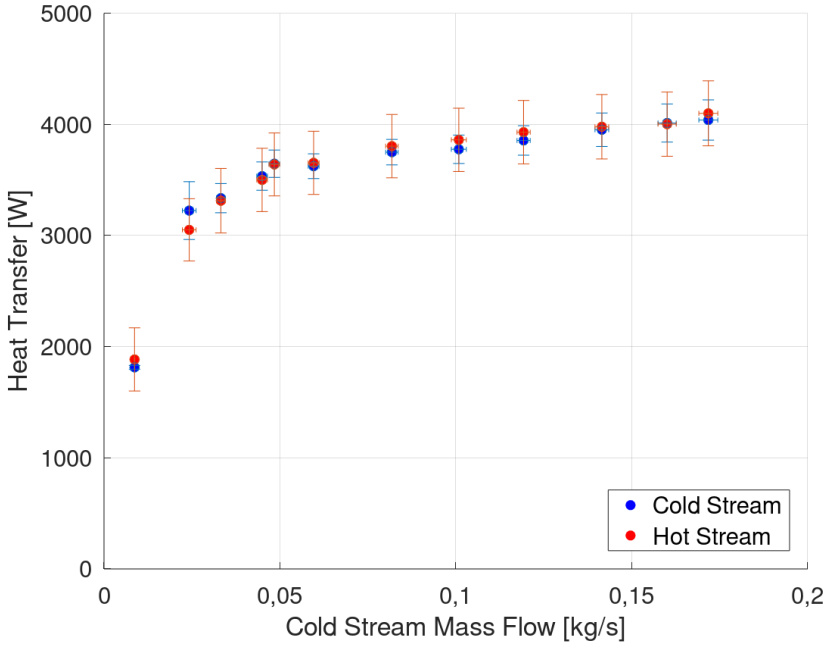

Figure 82 – Heat transfer rate. Hot stream inlet temperature at 80°C and mass flow rate at $0,1$kg/s.

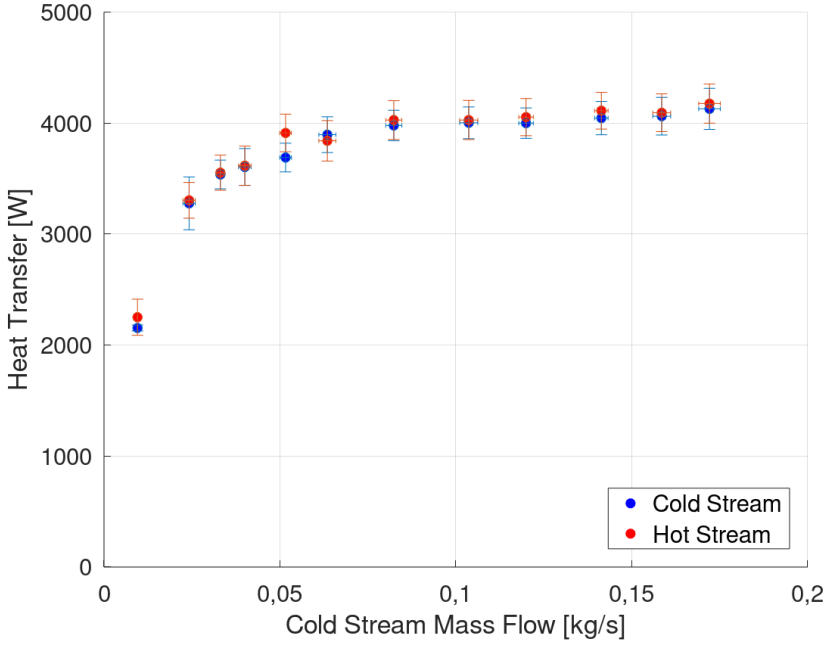

Figure 83 – Heat transfer rate. Hot stream inlet temperature at 80°C and mass flow rate at $0,15$kg/s.

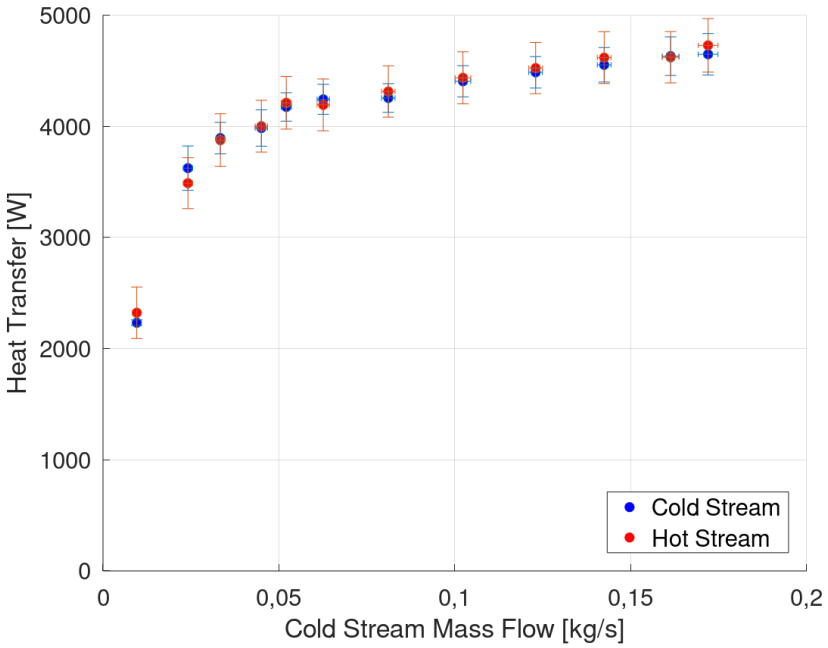

Figure 84 – Heat transfer rate. Hot stream inlet temperature at 80°C and mass flow rate at $0,2$kg/s.

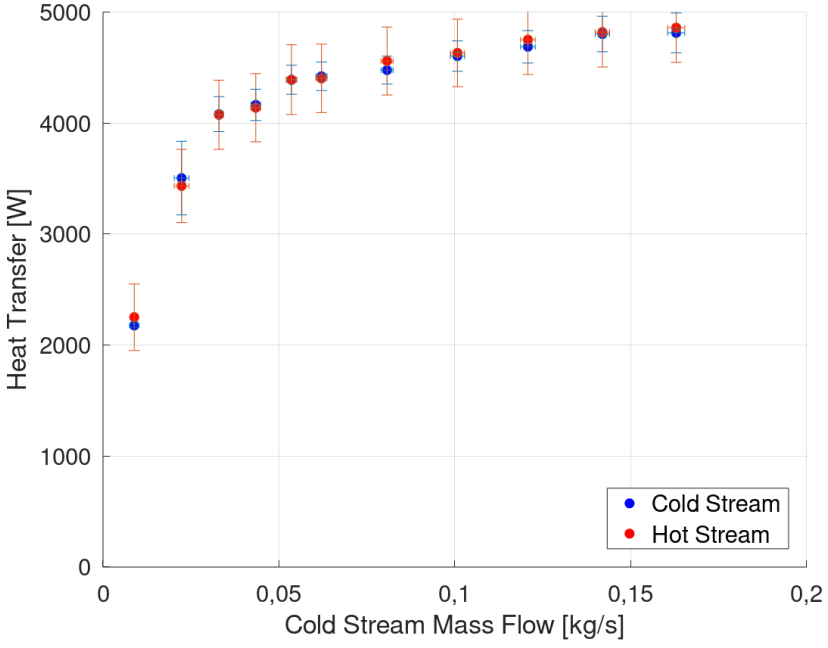

C.2 THERMAL CONDUCTANCE

This section contains the plots of thermal conductance of all test batteries not shown in chapter 7. Similarly, experimental results of thermal conductance of every test can be seen in figure 64, however, this figure does not show measurement uncertainties. Therefore, experimental results of each test battery are brought in this section, to allow different test batteries to be individually analyzed in further depth.

Figure 85 – Thermal conductance. Hot stream inlet temperature at 70°C and mass flow rate at $0,15$kg/s.

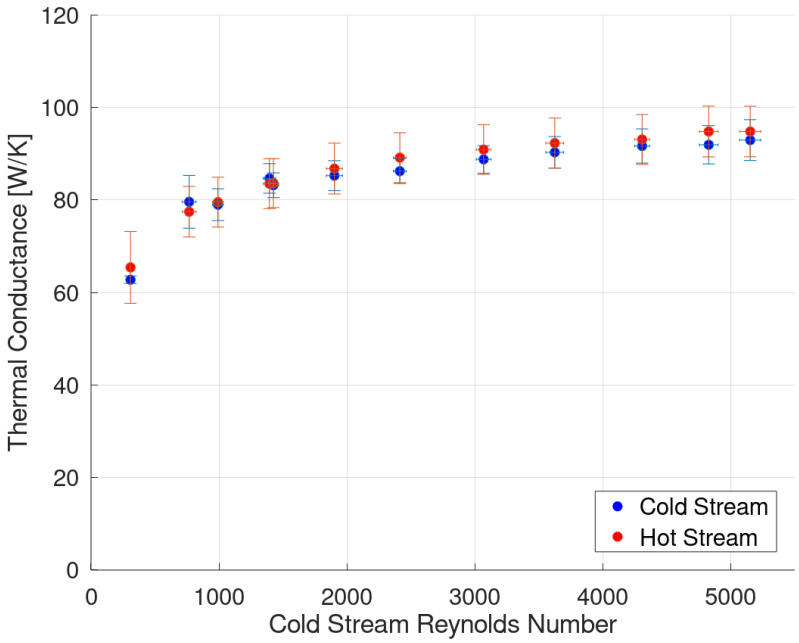

Figure 86 – Thermal conductance. Hot stream inlet temperature at 70°C and mass flow rate at $0,2$kg/s.

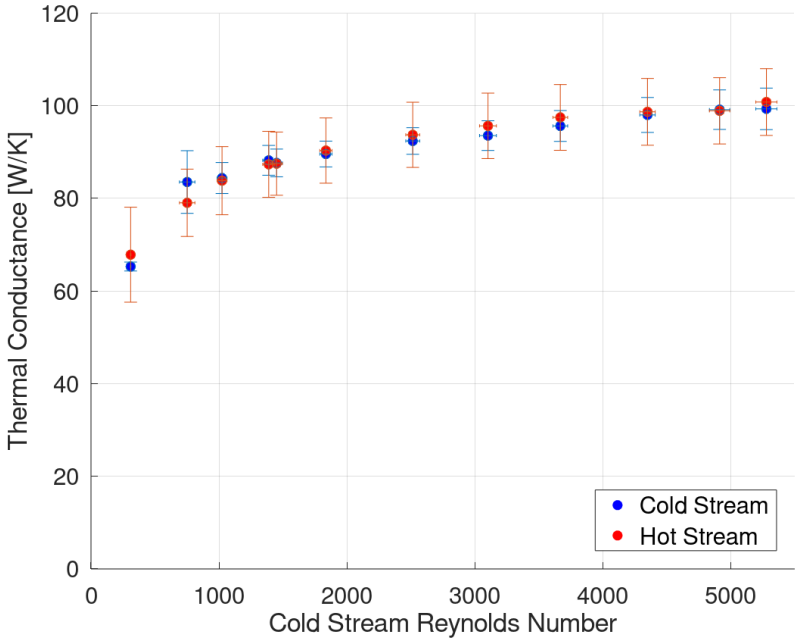

Figure 87 – Thermal conductance. Hot stream inlet temperature at 80°C and mass flow rate at $0,1$kg/s.

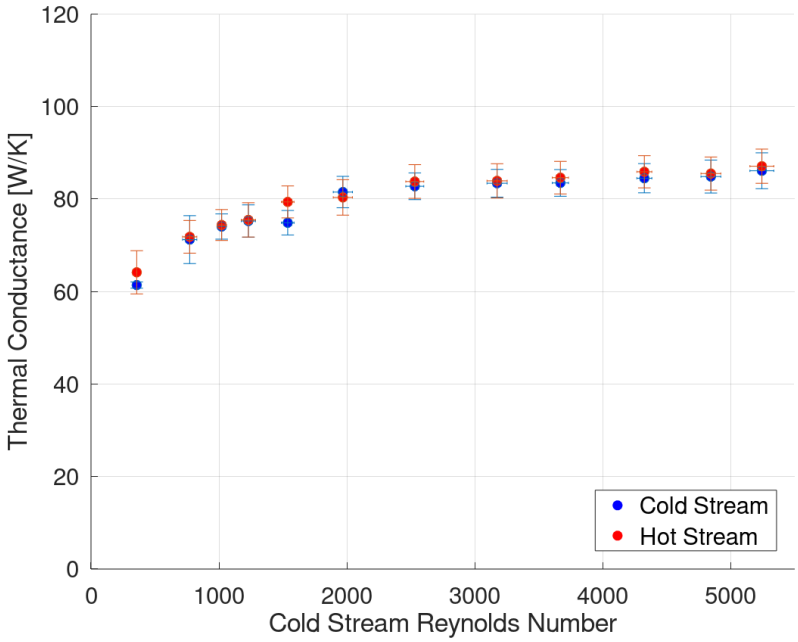

Figure 88 – Thermal conductance. Hot stream inlet temperature at 80°C and mass flow rate at $0,15$kg/s.

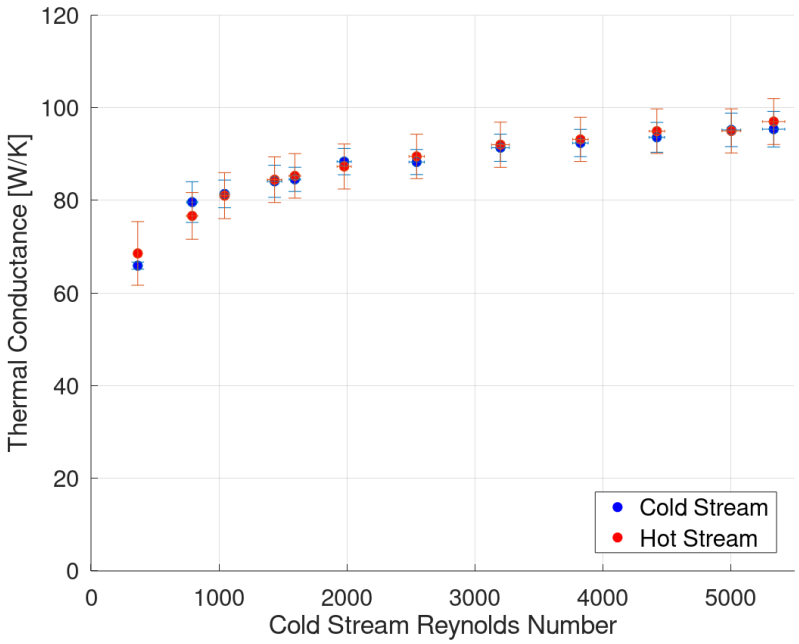

Figure 89 – Thermal conductance. Hot stream inlet temperature at 80°C and mass flow rate at $0,2$kg/s.